STARS

Electronic Theses and Dissertations, 2004-2019

2018

Nonlinear Dynamics in Multimode Optical Fibers

Mohammad Amin Eftekhar
University of Central Florida

University of Central Florida

STARS

Showcase of Text, Archives, Research & Scholarship

NONLINEAR DYNAMICS IN MULTIMODE OPTICAL FIBERS

by

MOHAMMAD AMIN EFTEKHAR

B. Sc. Shiraz University of Technology, 2009
M.Sc. University of Tehran, 2012
M.Sc. University of Central Florida, 2015

A dissertation submitted in partial fulfillment of the requirements

for the degree of Doctor of Philosophy

in the College of Optics and Photonics

at the University of Central Florida

Orlando, Florida

Spring Term

2018

Major Professor: Demetrios Christodoulides

ABSTRACT

Multimode optical fibers have recently reemerged as a viable platform for addressing a number of long-standing issues associated with information bandwidth requirements and power-handling capabilities. The complex nature of heavily multimoded systems can be effectively exploited to observe altogether novel physical effects arising from spatiotemporal and intermodal linear and nonlinear processes. Here, we have studied nonlinear dynamics in multimode optical fibers (MMFs) in both the normal and anomalous dispersion regimes. In the anomalous dispersion regime, the nonlinearity leads to a formation of spatiotemporal 3-D solitons. Unlike in single-mode fibers, these solitons are not unique and their properties can be modified through the additional degrees of freedom offered by these multimoded settings. In addition, soliton related processes such as soliton fission and dispersive wave generation will be also drastically altered in such multimode systems. Our theoretical work unravels some of the complexities of the underlying dynamics and helps us better understand these effects. The nonlinear dynamics in such multimode systems can be accelerated through a judicious fiber design. A cancelation of Raman self-frequency shifts and Blue-shifting multimode solitons were observed in such settings as a result of an acceleration of intermodal oscillations. Spatiotemporal instabilities in parabolic-index multimode fibers will also be discussed. In the normal dispersion regime, this effect can be exploited to generate an ultrabroad and uniform supercontinuum that extends more than 2.5 octaves. To do so, the unstable spectral regions are pushed away from the pump, thus sweeping the entire spectrum. Multimode parabolic pulses were also predicted and observed in passive normally dispersive tapered MMFs. These setting can obviate the harsh bandwidth limitation present in single-mode system imposed by gain medium and be effectively used for realizing high power multimode fiber lasers. Finally, an instant and efficient second-harmonic generation was

observed in the multimode optical fibers. Through a modification of initial conditions, the efficiency of this process could be enhanced to a record high of %6.5.

TO MY MOTHER

for her patience, limitless support and endless love

ACKNOWLEDGMENTS

It is my greatest pleasure to recognize those who have supported me. I am grateful to my Ph.D. advisor, Dr. Demetrios Christodoulides, who made this entire endeavor possible with his inspiring dedication and intuition and making this a great learning opportunity. I especially thank him for guiding and advising me throughout the years.

I would like to thank my committee for their constructive remarks and for sharing their expertise and knowledge in the field of nonlinear optics. I am highly grateful to Dr. Rodrigo Amezcua-Correa for his support and enabling the experimental works by giving full access to his facilities. I am also grateful to Dr. Guifang Li for providing me with his knowledge and guidance.

I am thankful to my wonderful and friendly colleagues at CREOL above all Nonlinear Wave group. I am grateful to CREOL staffs, especially Rachel Franzetta for constantly being available with generous supports and advice.

I was tremendously fortunate to have had many wonderful teachers and professors throughout the years. There are too many to list here, but I would like to especially thank Dr. Jalil Rashed-Mohassel, Dr. Mahmoud Shahabadi and Dr. Mojtaba Dehmollaian who inspired me to follow my passion for science. These are the ones who will always stand out in my mind.

Finally, I would like to thank my wonderful family and friends for always being supportive and encouraging.

TABLE OF CONTENTS

LIST OF FIGURES

LIST OF TABLES

LIST OF ACRONYMS

DGD: Differential Group Delay

DW: Dispersive Wave

FWM: Four-wave Mixing

GIMMF: Graded-index Multimode Fiber

MMF: Multimode Fiber

RSS: Raman Shifted solitons

SH: Second Harmonic

SHG: Second Harmonic Generation

SIMMF: Step-index Multimode Fiber

SMF: Single-mode Fiber

SPM: Self-phase Modulation

SSFS: Soliton Self-Frequency Shift

THG: Third Harmonic Generation

XPM: Cross-phase Modulation

CHAPTER 1: INTRODUCTION

The past three decades have witnessed a number of remarkable advancements in the general field of fiber optics. These breakthroughs have not only enabled a widespread proliferation of the internet, but have also radically transformed industrial manufacturing, laser surgery, optical microscopy, and sensing, to mention a few. Undoubtedly, one of the greatest innovations in this area was the development of photonic crystal fibers (PCFs) that in turn led to unprecedented opportunities in terms of controlling their nonlinear response via dispersion engineering and structural design [1,2]. In this regard, PCFs are nowadays commercially used in implementing spatially coherent ultra-bright supercontinuum sources, spanning the wavelength range from ultra-violet to the mid-infrared [3–7]. Fiber lasers represent yet another field that has experienced striking growth during this same period [8–11]. What made this class of lasers so successful is their notable power scalability, spectral and temporal versatility, high efficiency and their ability to be integrated into robust and modular systems. As such, fiber lasers with MW peak power levels, capable of producing CW radiation or ultrashort pulses are now readily available. As with most technologies that experienced a sudden progress in capabilities, it will not be long before physical constraints appear on the horizon to dampen future progress. Indeed, nonlinear limits and damage thresholds of existing small-core area fibers are now being approached, imposing restrictions on the maximum pulse energies/power one could expect from current fiber lasers and supercontinuum sources [7–9,12].

Equally important to this discussion is the fact that most of the new developments in fiber light sources have thus far relied almost exclusively on single mode (or quasi-single mode) fiber technologies [4–6,8,13–16]. Clearly, a straightforward and obvious approach to overcome some of the aforementioned limitations is to use large area multimode fibers. Multimode optical fibers

(MMFs) are common, and even predate single-mode fibers (SMFs). However, the high bandwidth and structural simplicity of SMFs caused interest in multimode systems to wane by the early 1980s. Today, MMFs are enjoying a renaissance because of their promise for even higher bandwidths based on space-division multiplexing that has emerged as a new paradigm in fiber optics communications [17,18]. The ensued flurry of activities not only led to new classes of MMF components (for amplification, switching, multimode signal processing, etc.) [19–21] but it has also prompted a critical rethinking as to how nonlinear processes unfold in multimode environments - an aspect that has so far remained largely unexplored. This is because historically nonlinear effects (self- and cross-phase modulation, Raman, four-wave mixing, etc.) have been traditionally investigated in SMFs [22], as opposed to more involved MMF systems that can in principle support thousands of modes.

Quite recently, the nonlinear properties of multimode fibers have been reconsidered in a number of studies [23]. In these experiments [24–30], nonlinear wave propagation in graded-index MMFs was found to lead to a series of unexpected results that are otherwise impossible in single-mode settings. These include for example the first observation of the so-called geometric parametric instability [25,27,29], modal condensation, formation of multimode soliton "molecules" [24,26], and uniform supercontinuum generation [27] - rivaling that expected from dispersion engineered PCFs operating close to their zero-dispersion point [6]. What makes this possible is the immense spatiotemporal complexity associated with these nonlinear wave-mixing processes in the presence of a large number of modes [25]. This added spatial degree of freedom can now open up new opportunities at both the scientific and technological level that were previously overlooked and remained unattainable because of technological barriers.

The objective of this dissertation is to study and exploit the physics and complexity of nonlinear dynamics in highly multimode fiber structures. In this regard, these nonlinear dynamics are studied in two regimes: the normal dispersion and the anomalous dispersion regime. First, a general theory is developed to better understand multimode soliton fission and dispersive generation process. This theory accurately explains the underlying reason behind the ultrabroad Cherenkov generation observed in MMFs. Built on this theory, we will study the effect of the initial modal composition on the resulting output spectrum and MM-soliton behavior. It turns out that, unlike in single-mode fibers, the properties of the fundamental multimode solitons such as temporal width, peak power, velocity and etc. cannot be easily determined only from the input pulse energy. But the modal composition of the input beam also plays a crucial role in this respect. It will also be shown that the output spectrum can be tailored by initially exciting the proper modal groups. Then later, the effect of perturbing MM-solitons through an acceleration of intermodal oscillations in a tapered graded-index MMFs is studied. We demonstrate that this spatiotemporal acceleration can have a prominent effect on the ensuing temporal and spectral behavior in both dispersion regimes. This mechanism leads to a peculiar class of relatively blue-shifted multimode solitons and introduces a new process for establishing blue-drifting dispersive wave combs through speeding up the collision dynamics among the constituent modes of multimode solitons. Under normal dispersive conditions, in the presence of an acceleration of intermodal oscillations, we observe a generation of accelerating frequency bands that dynamically sweep the entire spectrum. This, in turn, can be utilized to produce a notably flat and uniform supercontinuum, extending over 2.5 octaves.

Under the normally dispersive condition, nonlinear Schrödinger equation supports a self-similar parabolic pulse solution in the presence of a gain term [31–34]. Observation of these similaritons came as a solution to compensate for high optical nonlinear effects, resulting from the small core

and high field intensity of single mode fibers. However, limited gain bandwidth and small chirp available from cavity parameters set a severe limitation on the maximum achievable pulse energy and duration. We will that through a judicial design of a multimode fiber taper, one can overcome these limitations and realize highly chirped high bandwidth similaritons. In the last section, we experimentally demonstrate that high SHG conversion efficiencies of up to ~6.5% are accessible in heavily multimode parabolic-index germanium-doped optical fibers. This conversion occurred without first preparing the fiber via any of the known schemes. More importantly, the SHG was found to reach a maximum in an almost instantaneous manner.

Multicore optical fibers are also another avenue to address the rising need for higher information bandwidth. We present a general methodology to compute the supermodes and their corresponding propagation eigenvalues in a multicore system of arbitrary size and number of elements. To use multicore systems for high-bandwidth communication, one needs to overcome the modal walk-off between the supermodes. To this end, we suggest a new design in which all the eigenvalues lie on a ladder, equidistant from each other. By doing this, one can couple modes together through a simple grating structure and minimize the effect of differential group delays.

CHAPTER 2: UNIVERSAL THEORY OF CHERENKOV RADIATION BY FUSED MULTIMODE SOLITONS

The most significant feature of wave propagation in the anomalous dispersion regime is soliton formation. In this regime, the input packets of high energy, equivalent to higher-order solitons, experience a soliton fission and disintegrate into their constituent solitons. This process is accompanied by a transfer of energy from solitons to dispersive waves (DWs). These low amplitude dispersive waves play an important role in the spectral content generation in the shorter wavelength side of the spectrum (near blue and UV). Although these processes are extensively studied in the context of single-mode fibers, they are very poorly understood in the multimode settings. So far there has been no theoretical work that can explain the underlying dynamics of multimode solitons fission and their respective broadband DW generation. In this chapter, we present a general theory that explains this rather involved process and helps us predict and control the output spectral features of a multimode system. Before getting into the analysis we need to first know what multimode solitons are and how they are different from their single-mode counterparts.

2.1 Multimode Optical Solitons

A multimode soliton is a composite structure in which several modes travel together. To form a multimode soliton, the input field should compensate for intermodal dispersion as well as chromatic dispersion. Our analysis will be similar to what presented by Crosignani et al [35]. In this analysis, we only consider the effect of the electronic processes and ignore non-instantaneous effects such as Raman effect. In this case, the nonlinear polarization P^{NL} takes the form below

$$P_{NL}(t) = \left(\frac{\sigma}{2}\right) \boldsymbol{E}(t).\boldsymbol{E}(t)\boldsymbol{E}(t) \qquad (1)$$

This nonlinear electric polarizability modifies the index by $\epsilon_2 |\hat{E}_x|^2$. We suppose that the electric field $\boldsymbol{E}$ has a single polarization like $\hat{E}_x$ which is orthogonal to the propagation direction. In this analysis, the fiber is considered to be weakly guiding so as it allows for neglecting longitudinal component with respect to the transverse ones. The field component $\hat{E}_x$ that modifies the refractive index of the environment is actually a superposition of many spatial modes centered at different frequencies

$$\hat{E}_x(\boldsymbol{r}, z, t) = \sum_\nu E_\nu(\boldsymbol{r}) \exp(i\beta_\nu(\omega_\nu)z - i\omega_\nu t)\, \hat{\Phi}_\nu(z, t) \qquad (2)$$

Here $\boldsymbol{r} = (x, y)$ represents the transverse coordinates, the terms $E_\nu(\boldsymbol{r})$'s are the spatial mode configurations. Various modes are considered to be centered around different central wavelengths ω_ν. The term $\beta_\nu(\omega_\nu)$ is the propagation constant of the νth mode. $\hat{\Phi}_\nu(z, t)$'s are the slowly varying mode amplitudes for different modes. The total dielectric constant varies with the total electric field as below:

$$\epsilon(\boldsymbol{r}, z, \omega) = \epsilon_1(\boldsymbol{r}, \omega) + \epsilon_2 |\hat{E}_x(\boldsymbol{r}, z, t)|^2 \qquad (3)$$

where $\epsilon_1(\boldsymbol{r}, \omega)$ is the fiber linear dielectric constant. The second term is responsible for a deviation from the linear index distribution that leads to a modal deformation and hence intermodal coupling. According to the modal amplitudes should satisfy the following nonlinear Schrödinger equation. In the following equation, four-wave mixing terms are ignored [5].

$$i\frac{\partial \hat{\Phi}_\nu}{\partial z} + \frac{i}{V_\nu}\frac{\partial \hat{\Phi}_\nu}{\partial t} + \frac{1}{2A_\nu}\frac{\partial^2 \hat{\Phi}_\nu}{\partial t^2} + \left[\sum_{\mu \neq \nu} 2R_{\mu\nu}|\hat{\Phi}_\mu|^2 + R_{\nu\nu}|\hat{\Phi}_\nu|^2\right]\hat{\Phi}_\nu \qquad (4)$$

$$\nu = 1, 2, \dots$$

$$R_{\mu\nu} = \left[\frac{\omega_0\left(\frac{\epsilon_2}{\epsilon_0}\right)}{2n_1 c}\right]\frac{\iint_{-\infty}^{+\infty} E_\mu^2(\boldsymbol{r})E_\nu^2(\boldsymbol{r})dxdy}{\iint_{-\infty}^{+\infty} E_\nu^2(\boldsymbol{r})dxdy}.$$

$R_{\mu\nu}$ calculates the modal overlap between different modes and calculates simply the nonlinear cross-section when $\mu = \nu$. In this relation n_1 in the average value of the fiber linear refractive index. The parameter $V_\nu^{-1} = \left(\frac{d\beta_\nu}{d\omega}\right)_{\omega=\omega_\nu}$ shows the group velocity of mode ν at the central frequency ω_ν and $A_\nu^{-1} = \left(\frac{d^2\beta_\nu}{d\omega^2}\right)_{\omega=\omega_\nu}$ is the dispersion of each mode at the central frequency ω_ν. The term A_ν^{-1} is different for each mode which stems from the fact that each mode has a different dispersion profile.

The essential condition for a formation of a multimode soliton is that all the modes involved need to travel together.

$$V_\nu^{-1} = V^{-1} = \left(\frac{d\beta_1}{d\omega}\right)_{\omega=\omega_1} = \left(\frac{d\beta_2}{d\omega}\right)_{\omega=\omega_2} = \left(\frac{d\beta_3}{d\omega}\right)_{\omega=\omega_3} = \cdots \qquad (5)$$

It can be shown that the bright-soliton solution of the kind below can satisfy the multimode nonlinear Schrödinger equation.

$$\widehat{\Phi}_\nu(z,t) = \widehat{\Phi}_{0\nu} \exp\left(\frac{iz}{2A_\nu\tau^2}\right) \mathrm{sech}\left[\frac{\left(t-\frac{z}{V}\right)}{\tau}\right], \nu = 1,2,\dots \qquad (6)$$

This shows there is a bright soliton with a $sech(t)$ time-dependency for each mode. The nonlinear phase that each individual mode accumulates is different but all will have the same duration and the same group velocity. The above-mentioned solitons exist provided that the modal components satisfy the relation below

$$-\frac{1}{A_\nu\tau^2} = 2\sum_\mu R_{\mu\nu}\left|\widehat{\phi}_{0\mu}\right|^2 + R_{\nu\nu}\left|\widehat{\phi}_{0\nu}\right|^2, \nu = 1,2,\dots \qquad (7)$$

Form the relation above, one can say that given the input pulse energy, there is no unique distribution for a multimode soliton and hence there can be many solitons all satisfying the above equation and having different modal distributions.

The lower limit for the field intensity required for mode trapping is given as

$$\frac{(V_\mu - V)^2}{V^2} \ll - \left(\frac{V^2}{A_\nu}\right)\left[\frac{\omega_0\left(\frac{\epsilon_2}{\epsilon_0}\right)}{n_1 c}\right] \times \sum_\mu \alpha_{\mu\nu}|\hat{\Phi}_\mu|^2, \quad \nu = 1,2,\dots \qquad (8)$$

That shows the intensity of a multimode soliton in step-index fibers is higher than that for graded-index fibers due to a larger modal walk-off.

2.2 Dispersive Wave Generation in Multimode Systems

Equation (6) tells us that each mode possesses a nonlinear phase in the form of $\exp\left(\frac{iz}{A_\nu \tau^2}\right)$. Reconsidering the gauge transformations, the dispersion relation associated with each of the constituent modes of a multimode soliton is given as below

$$\beta_{pq}(\omega) = \beta_{pq}\left(\omega_{s_{pq}}\right) + \frac{1}{V}\left(\omega - \omega_{s_{pq}}\right) + \frac{1}{A_{pq}\tau^2} \qquad (9)$$

In this relation, we relied on the fact that a soliton does not disperse during propagation and hence does not have higher order dispersion terms. The indices p and q refer to the spatial mode (p,q). The clear dependence of the last term on the input power levels is represented in the relation below

$$\beta_{pq}(\omega) = \beta_{pq}\left(\omega_{s_{pq}}\right) + \frac{1}{V}\left(\omega - \omega_{s_{pq}}\right) + \left[R_{pq,pq}|\hat{\phi}_{0,pq}|^2 - 2\sum_{p',q'} R_{p'q',pq}|\hat{\phi}_{0p'q'}|^2\right] \quad (10)$$

In cases that we are dealing with a single-mode system, the cross-phase terms are absent and the first term turns simply into $\gamma|E|^2$ that accounts only for the self-phase modulation effect. Here, we use the simpler variation $\frac{1}{A_\nu \tau^2}$ in our formulation. Knowing the temporal pulse-width of the soliton and the dispersion relation of each of the mode at their central frequencies, one can calculate the nonlinear phases. Practically, since the dispersion of the modes is very similar to each other, one legitimate approximation is considering all the dispersion terms to be equal for all the modes.

Cherenkov radiation is defined as linear waves of the form $A = e^{i(kz-\omega t)}$ that are generated through a phase-matching condition with solitons for a short period of time during the soliton fission process. The dispersive wave components lie mainly in the visible wavelengths and satisfy the nonlinear Schrödinger equation.

$$i\partial_z A - \left(\frac{1}{2!}\beta_2\partial_t^2 + \frac{i}{3!}\beta_3\partial_t^3 + \cdots\right)A = -\gamma|A|^2 A - T\gamma A\partial_t|A|^2 \qquad (11)$$

As it was mentioned before, resonant Cherenkov radiation primarily depends on the phase-matching conditions and is therefore narrowband. However, recent numerical and experimental results prove otherwise [36,37]. The generated dispersive waves (DWs) in these works extend to hundreds of nanometers. Although some of the aspects of this process are previously explained [36], however, one cannot still explain the ultrabroad DW generation in heavily multimoded step-index fibers when excited in the anomalous dispersion regime. Our studies reveal, for the first time, a universal system to understand the process for any multimode system.

The radiation frequency ω_R is found through a phase-matching between the soliton and the low amplitude linear waves;

$$\beta_s(\omega_R) = \beta(\omega_R) \qquad (12)$$

Where β_S is the soliton wavenumber and $\beta(\omega)$ is the fiber's linear dispersion relation. Efficient dispersive wave generation occurs over a short propagation distance before the emergence of the distinct fundamental solitons. For the special case of parabolic-index multimode fibers, the dispersion relation is given as below:

$$\beta_{mn} = k_0 n(\omega)\left[1 - \frac{2(m+n+1)}{k_0 n(\omega)}\sqrt{\frac{2\Delta}{a^2}}\right]^{1/2} \qquad (13)$$

As it was previously pointed out, the essential condition for the formation of multimode solitons is mode fusion.

$$v_{g_{m,n}}^{-1} = \frac{d\beta_{mn}}{d\omega} = V^{-1}.$$

From Eq. (13) the modal group velocity in graded-index MMFs can be calculated as below:

$$v_{g_{m,n}}^{-1} = \frac{\frac{1}{c}(n(\omega)+\omega\, dn/d\omega)}{\sqrt{1-\frac{2(m+n+1)\sqrt{\frac{2\Delta}{a^2}}}{\frac{\omega}{c}n(\omega)}}}\left[1-\frac{(m+n+1)\sqrt{\frac{2\Delta}{a^2}}}{\frac{\omega}{c}n(\omega)}\right] \tag{14}$$

where (m,n) denotes the spatial mode profile indices. For different modes (m,n) the central frequency $\omega_{m,n}$ should be tuned so as all the modes move together. Knowing the escape velocity of a soliton, all the frequencies can be found. To account for the modal dispersion relations in graded-index multimode fibers, since the second term under the square root is much smaller than 1, one can use the following approximate relation

$$\beta_{mn} = k_0 n(\omega) - (m+n+1)\sqrt{\frac{2\Delta}{a^2}} \tag{15}$$

The MM-soliton dispersion relation can now be written as

$$\beta_{S_{pq}}(\omega) = \frac{\omega_{S_{pq}}}{c}n\left(\omega_{S_{pq}}\right) - (p+q+1)\sqrt{\frac{2\Delta}{a^2}} + \frac{1}{V}\left(\omega - \omega_{S_{pq}}\right) + \frac{1}{A_{pq}\tau^2} \tag{16}$$

The phase-matching condition is met for dispersive waves at frequency ω_R. If DW content is generated in the modal component (m,n), we represent the phase-matched frequency by $\omega_{R_{mn}}$

$$\frac{\omega_{S_{pq}}}{c}n\left(\omega_{S_{pq}}\right) - (p+q+1)\sqrt{\frac{2\Delta}{a^2}} + \frac{1}{V}\left(\omega_{R_{mn}} - \omega_{S_{pq}}\right) + \frac{1}{A_{pq}\tau^2} =$$

$$\frac{\omega_{R_{mn}}}{c}n(\omega_{R_{mn}}) - (m+n+1)\sqrt{\frac{2\Delta}{a^2}} \tag{17}$$

$$\frac{\omega_{R_{mn}}}{c} n(\omega_{R_{mn}}) - \frac{1}{V}\omega_{R_{mn}} = (m + n - p - q)\sqrt{\frac{2\Delta}{a^2}} + \frac{\omega_{S_{pq}}}{c} n\left(\omega_{S_{pq}}\right) - \frac{1}{V}\omega_{S_{pq}} + \frac{1}{A_{pq}\tau^2}$$

by applying further simplifications, we arrive at the following equation

$$\omega_{R_{mn}}\left(\frac{n(\omega_{R_{mn}})}{c} - \frac{1}{V}\right) = (m + n - p - q)\sqrt{\frac{2\Delta}{a^2}} + \frac{\omega_{S_{pq}}}{c} n\left(\omega_{S_{pq}}\right) - \frac{1}{V}\omega_{S_{pq}} + \frac{1}{A_{pq}\tau^2} \quad (18)$$

For typical values $\Delta = 3 \times 10^{-3}$ and $a = 25\ \mu m$, $\sqrt{\frac{2\Delta}{a^2}} \approx 5.65 \times 10^3$. At the soliton fission point,

the pulsed beam significantly squeezes in time and space. Its compression in space is equivalent

to a population of many higher-order spatial modes. The fundamental component of the first

soliton is denoted by $p + q = 1$. It can in principle couple to different spatial modes in DWs and

occupy the spatial mode (m, n). Assuming that all modal components contributing to the formation

of a multimode soliton are lying close to each other and from the Eq. (15) one can expect a

grouping of DW lines and formation of a discrete DW radiation pattern.

Table 2-1 The approximate order (location) of DW combs based on the modal make-ups

n, m	0	1	2	3	4	5	6
0		1	2	3	4	5	6
1		1	2	3	4	5	6	.
2		2	3	4	5	6	.	.
3		3	4	5	6	.	.	.
4		4	5	6	.	.	.	.
5		5	6	.	.	.	.	.
6		6	.	.	.	.	.	.

Table 2-1 indicates that the energy present in a particular soliton mode (p_1, q_1) can be coupled to the all the DW modes with the same $m + n$ indices sit in the same location. This leads to a grouping of spectral DWs lines and formation of DW-combs.

To corroborate our theory, we performed a series of numerical studies with the help of a gUPPE simulator. In these simulations, a graded-index MMF of 31.25 μm core radius was excited with an on-axis pulsed beam having 400-fs pulse-width and centered at 1550 nm. The spectrum pertaining to this simulation is shown in Figure 2-1.
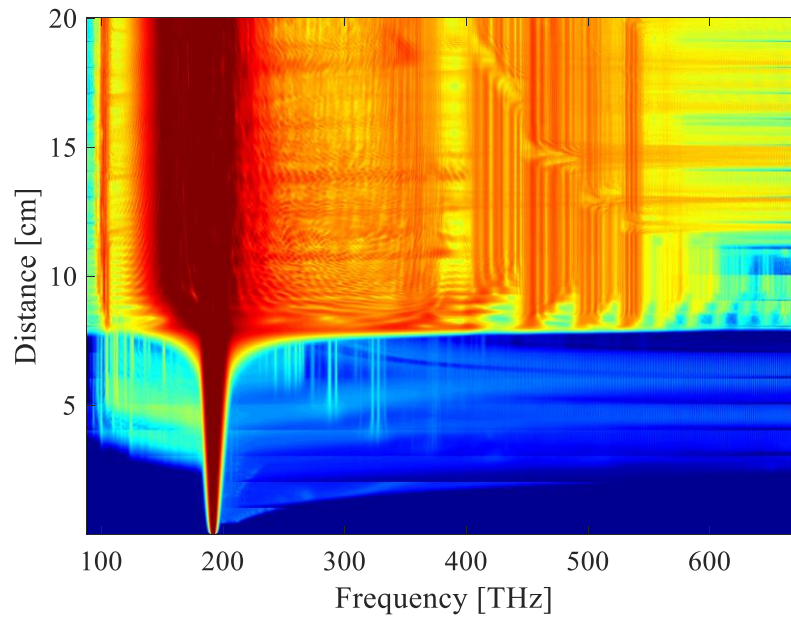
Figure 2-1 The spectral evolution of a 400-fs pulse centered at 1550 nm when propagates for 20 cm in a graded-index MMF, obtained from a gUPPE simulation.

The temporal evolution of the same simulation is shown in Figure 2-2 and Figure 2-3.
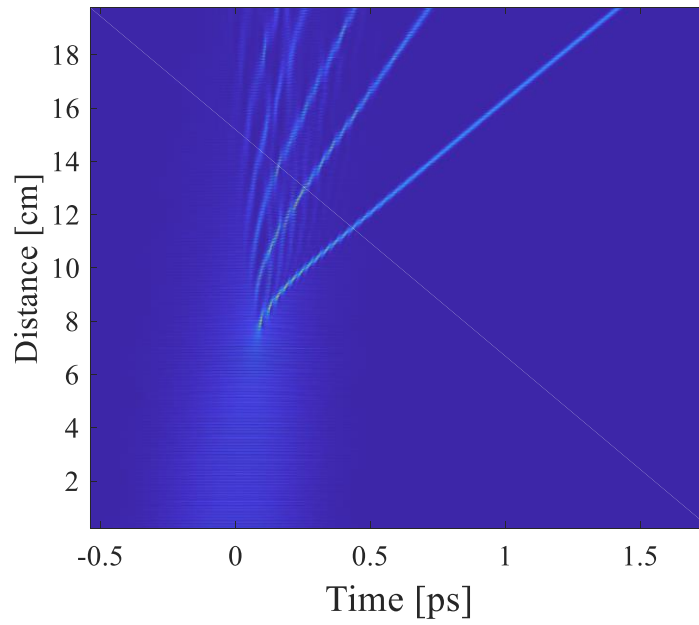
Figure 2-2 The temporal pulse evolution corresponding to Figure 2-1
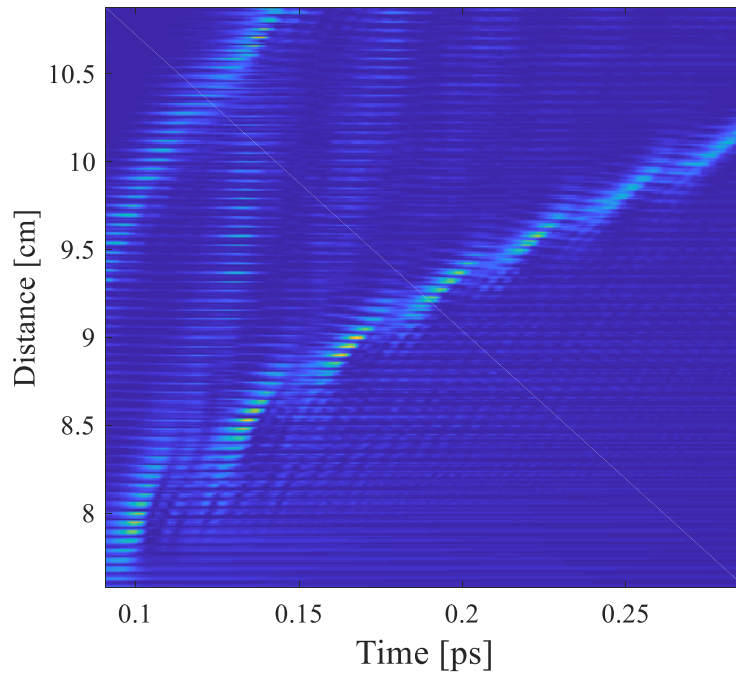
Figure 2-3 A closer look at multiple pulse compression occasions of the first soliton shown in Figure 2-1, right after the major soliton fission.

The first emitted soliton which also has the highest intensity is responsible for the significant red-shifting observed in the spectrum in Figure 2-4.
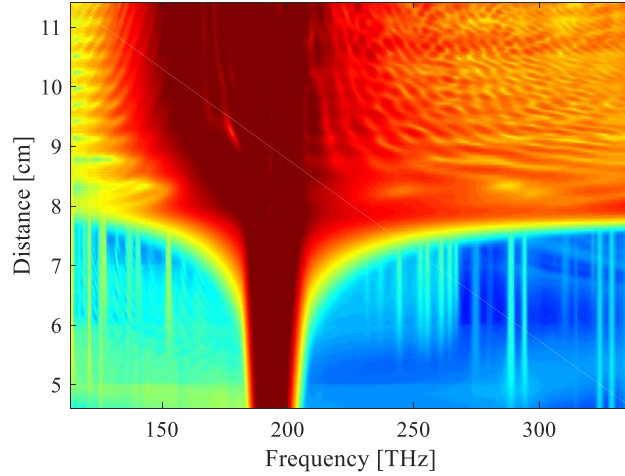
Figure 2-4 A closer look at the spectral features of the first red-shifted soliton.

The group velocity of the strongest soliton is calculated from simulations to be $2.0465 \times 10^8 \ m/s$ proportional to a soliton lying around 161.2 THz (1.8598 µm). The central frequency for each mode contributing to the multimode soliton is calculated from this velocity. Our theory predicts the DW lines to be at values given in Table 2-2. The values match very well with our numerical results obtained from gUPPE simulation (Figure 2-5)

Table 2-2 The predicted DW line locations calculated from the velocity of the first emitted soliton

N	f_{DW} (THz)
0	445.1
1	475.3
2	498.7
3	518.4
4	535.7
5	551.1
6	565.1
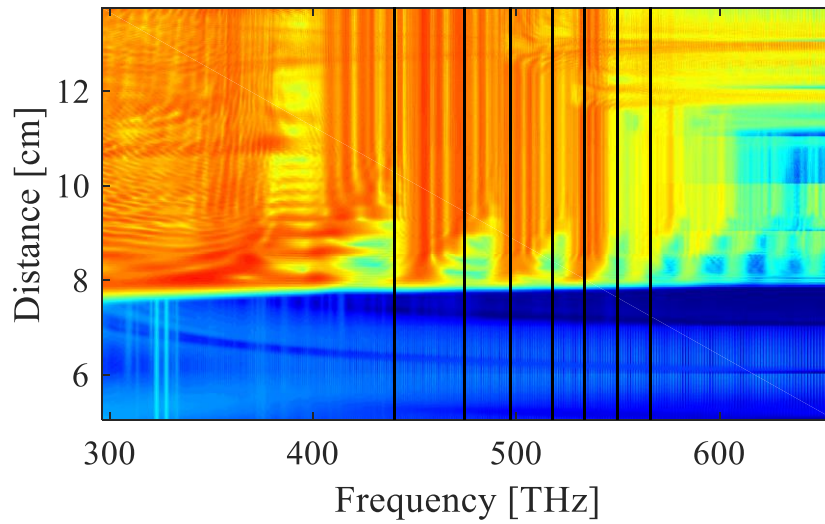
Figure 2-5 The perfect matching of the DW lines and the theoretical predictions (black lines)

Now, we check the DWs generated by the soliton before it experiences a significant redshifting. Shortly after the soliton fission, the strongest soliton which lies around 1.597 µm (187.7THz) and

has a velocity of $2.049 \times 10^8 \, m/s$ give rise to a series of DWs. Based on our theory, the phase-matching condition is met for the frequencies given in Table 2-3.

Table 2-3 The predicted DW line location computed from the velocity of the soliton

N	$f_{DW} \, (THz)$
0	368.9
1	419.3
2	450.8
3	475.3
4	495.9
5	513.7
6	529.6
7	544.1
8	557.7
9	570.1
10	581.8

Since in this example, only the LP_{0m} modes are excited, only DW lines with a multiplication of two ($N = 0,2,4,...$) are expected to show up. The perfect matching between these peaks and our prediction is evident in Figure 2-6
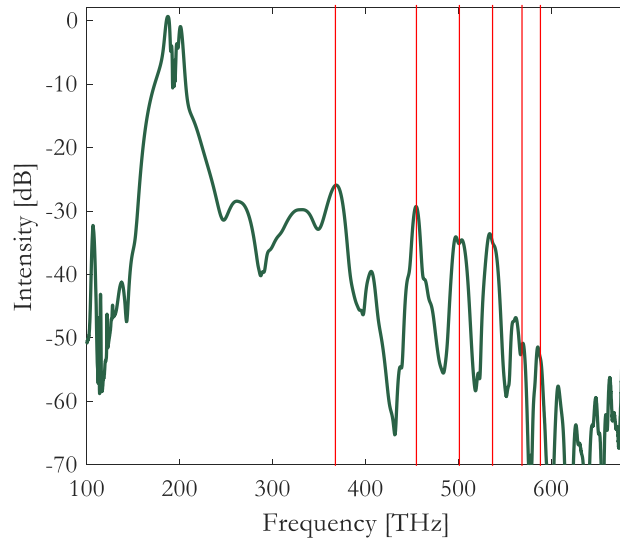
Figure 2-6 Comparing the predicted locations of the DW lines with the actual spectrum obtained right after the first major soliton fission.

Relying on this theory, one can also explain the spectral peak lying on the higher wavelength edge. As it can be seen in Figure 2-7, the phase-matching condition can be met at higher wavelengths edge (~2-3 μm). This explains the curious line in the NIR that always shows up after a multimode soliton fission. Therefore, in such multimode systems, the DW resonance frequency does not necessarily lie in the visible wavelengths. But it can be also found in the higher-wavelength edge, according to the phase-matching conditions.
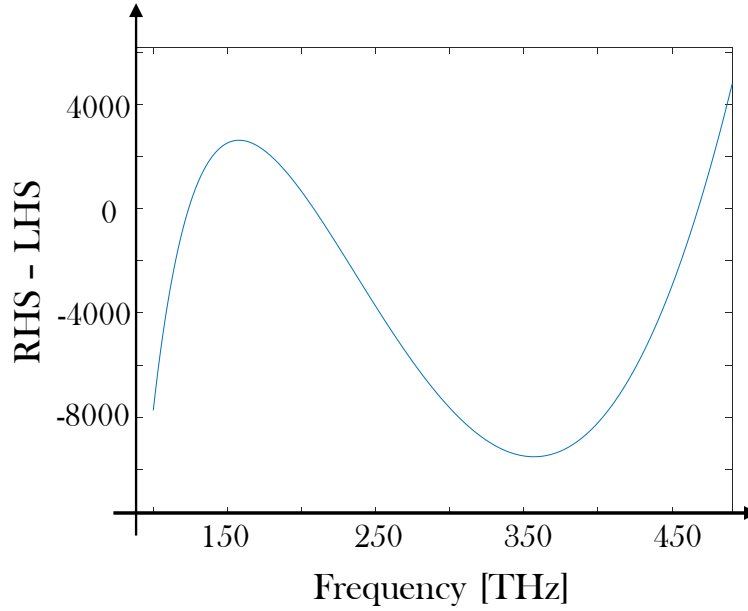
Figure 2-7 The phase-matching condition explains the DW line generated in the 2-3 µm frequency region.

To predict the location of the DW-combs using this technique, one should know the central wavelengths of solitons (or equivalently their escape velocity). This is very difficult without performing a simulation or having the spectrum evolution. However, a very good approximation can be made based on the fact that right after the soliton fission, all the solitons lie at 1550 nm. This is later when under the action of intrapulse Raman scattering, they experience a red-shifting (deceleration). However, the first and strongest DW-comb is produced right after the soliton fission and before Raman-induced frequency shift come into play. The experiment was performed on a multimode fiber with a core radius of 35 µm and $\Delta n = 0.03$. The locations of DWs, assuming that the generated MM-solitons lies approximately at the pump wavelength, the phase-matching condition predicts DW wavelengths. Figure 2-8 demonstrates the perfect phase-matching present between our theoretical predictions and the experimental results.
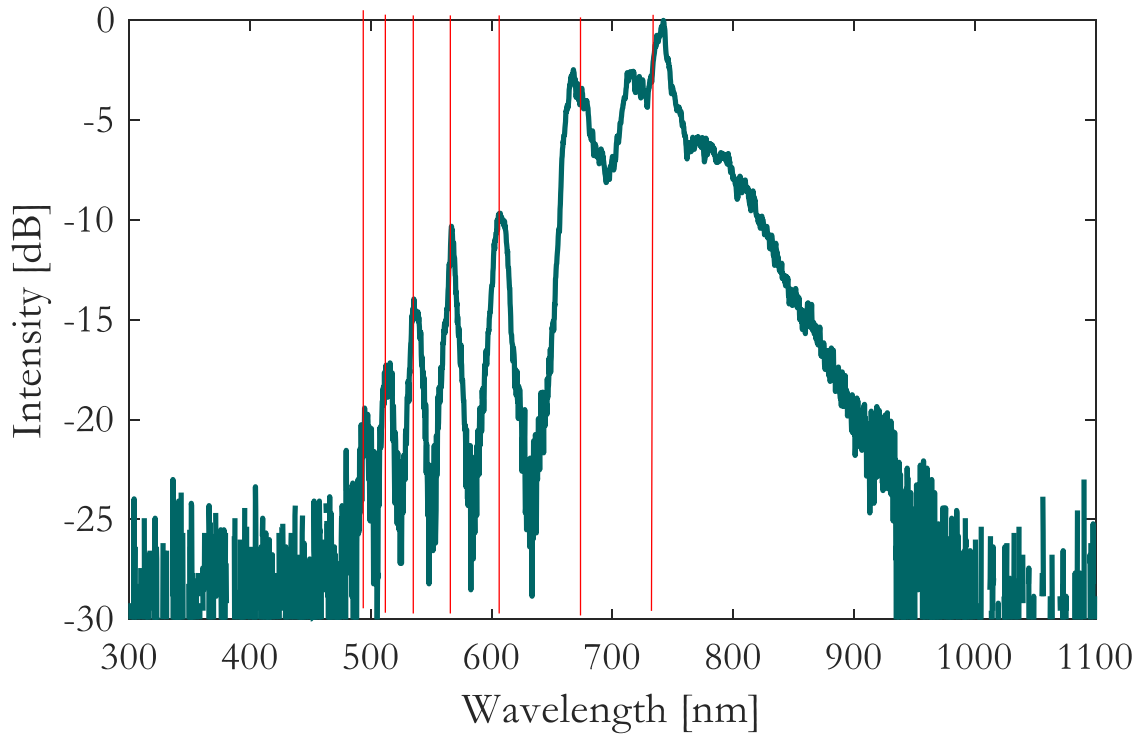
Figure 2-8 A comparison between predicted DW lines and the spectrum for experimentally measured DWs recorded in the output of a 10 m long parabolic-index MMF with a core radius of 35 μm.

As it can be seen in Figure 2-8 there is an excellent agreement between our predicted locations of

the DW-comb lines and the experimental results. Again, due to a symmetric excitement of the

fiber, only even orders are excited and the rest are not present in this figure.

Table 2-4 The predicted DW line locations, for the experimental results shown in Figure 2-8.

$k - (m + n)$	DW location
0	1689.0
1	734.6
2	675.3
3	636.9
4	608.2
5	585.3
6	566.3
7	550.4
8	536.5
9	524.2
10	513.0
11	503.5
12	494.3

It is worth mentioning that since the soliton energy is predominantly in the fundamental mode, for the sidebands lying in the larger frequencies, the population will be in favor of higher-order modes, which is in agreement with [36], however, all the DWs will be multimoded because of numerous pathways between many modes of the soliton and DW. This is also in agreement with the results presented in [37], where by deliberately populating higher-order modes, the energy content in the DW-combs and their modal distributions could be greatly modified.

Despite the fact that the efficiency of coupling drops for frequencies farther from zero-dispersion wavelength, the presence of many more modes for farther DW lines causes the existing energy no to drop radically and hence the spectrum can in principle extend to very short wavelengths (<500 nm).

Given this theory, in dealing with fibers that do not have an equidistant distribution of eigenvalues, one expects a drift of grouped sidebands away from each other and formation of a continuous hump of energy. The theoretical and experimental results for a step-index fiber are in agreement with this theory. As it can be seen in Figure 2-9, the soliton fission has resulted into an ultra-broad dispersive wave that extends from 1000 nm to below 500 nm. The simulation results, obtained from a gUPPE simulation, also confirm this broadband phase-matching condition leading to the development of such energy lump in the visible window.
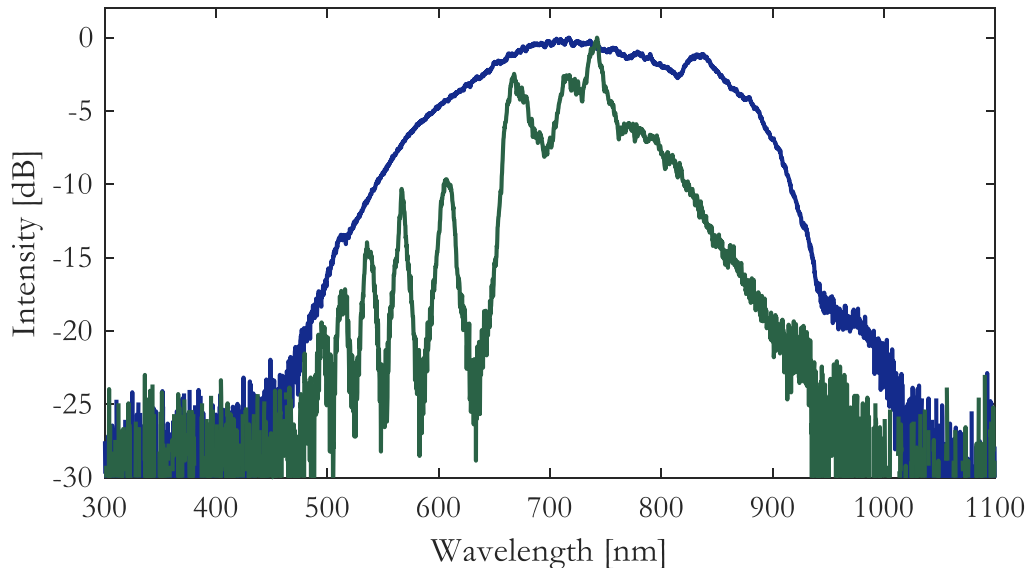
Figure 2-9 A comparison between the DWs generated from a step-index MMF and a parabolic-index MMF. The extent of DWs generated in both cases is approximately the same. However, the DWs generated from a step-index MMF do not have the comb-like features, observed in GIMMFs.
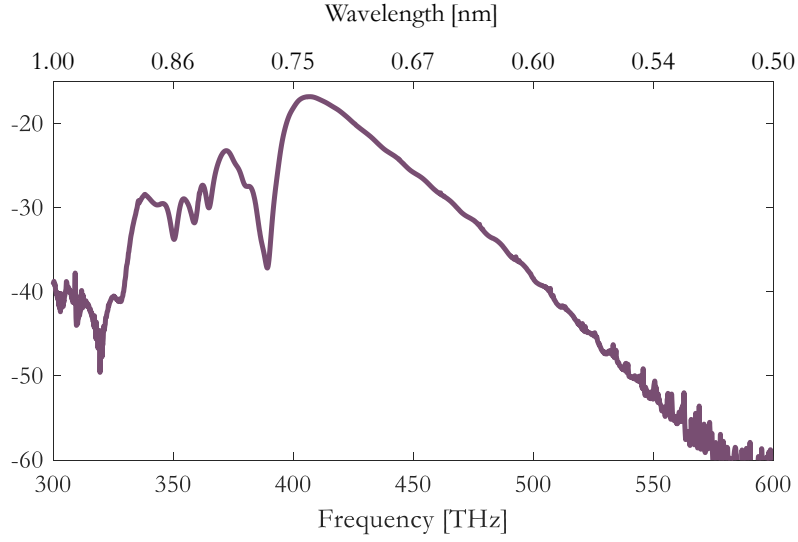
Figure 2-10 Numerical simulations computed from a gUPPE simulator also show a generation of a wideband DWs as a result of soliton fission.

Equation (17) shows that there is a nonlinear phase term in the phase-matching condition between DWs and the solitons. This nonlinear phase term predicts a shift in the DWs with a significant change in the input power levels. Figure 2-11 and Figure 2-12 represent the behavior of generated DWs, measured at the end of a graded-index multimode fiber and step-index multimode fiber, respectively, for different power levels.
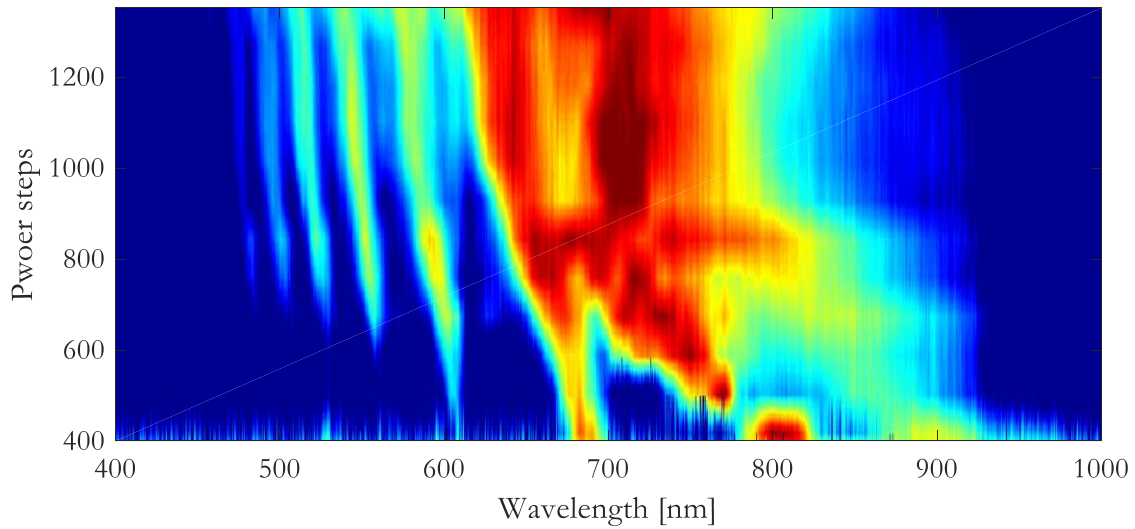
Figure 2-11 Experimentally measured blue-drifting of DWs as a result of an increase in the input power levels. The blue drifting of DW comes as a result of the nonlinear phase term.
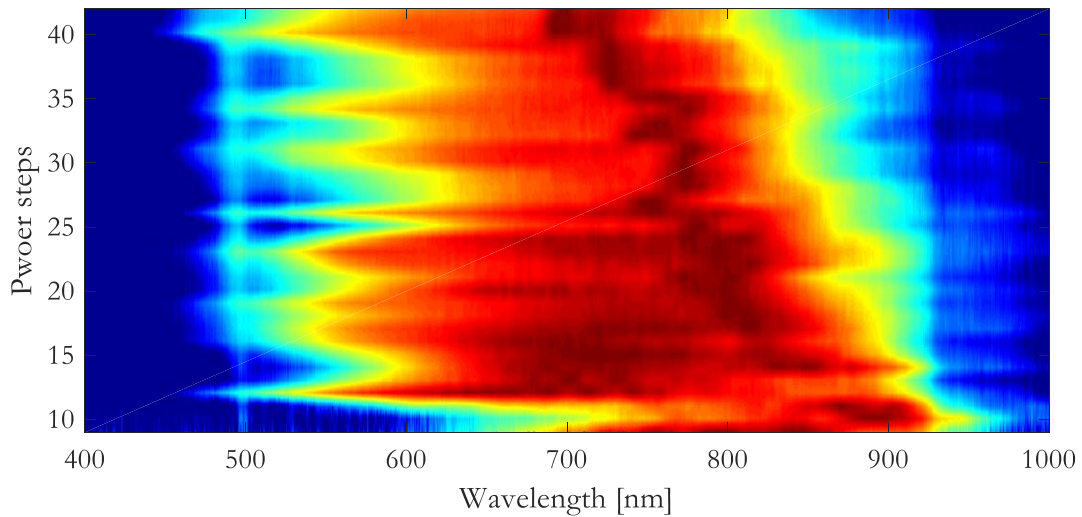
Figure 2-12 Experimentally measured blue-drifting of DWs when the input power grows – as a result of the nonlinear phase term.

As it can be clearly seen in these figures, by increasing the input power, DWs drift toward shorter wavelengths which is in agreement with our theoretical predictions. However, since lower order modes have a larger nonlinear coefficient, their spectral shift is expected to be more significant.

23

The analysis given above was only for the first emitted soliton, while in principle for energies large enough there can be multiple solitons. The first soliton is the strongest and slowest soliton. Since the other generated solitons have a larger group velocity the DW lines are expected to lie farther. Figure 2-13 represents numerical results when the pulse breaks into a number of solitons.
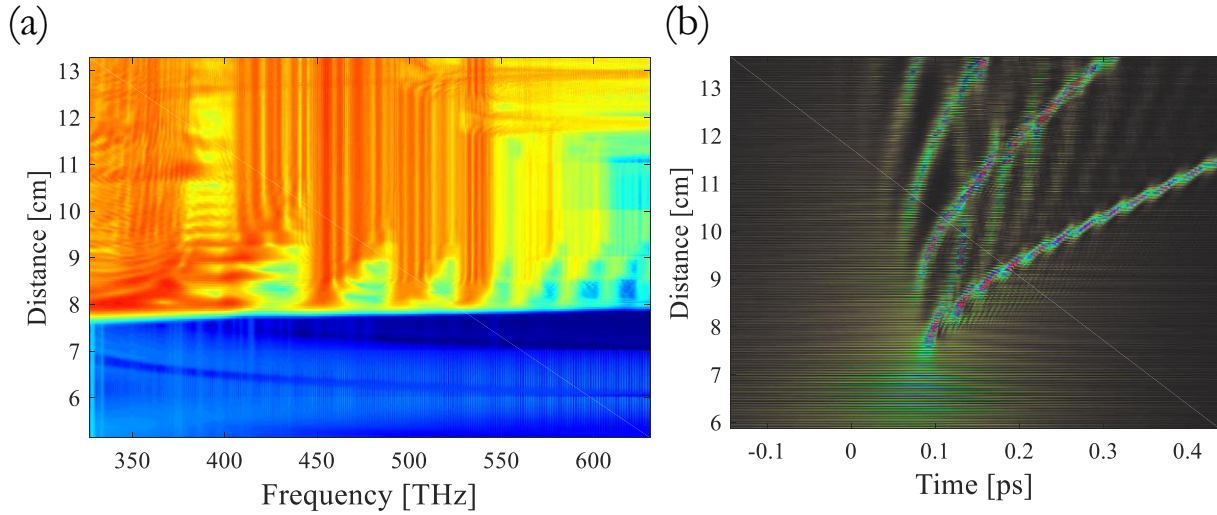
Figure 2-13 Numerically computed soliton evolution in space-time and its corresponding generated DWs. Different solitons are coupled to a shifted version of DW-comb.

According to our numerical simulations, the solitons are generated on a course of a few centimeters and each has a radically different group velocity. The corresponding DWs are also generated discretely and over a few centimeters, each one slightly shifted toward blue, which is a result of faster emitted solitons.

Given this analysis, to generate a very broad and homogenous DW spectrum, one should use a waveguide with a randomly distributed series of eigenvalues (such as Hénon-Heiles potential Figure 2-14). To this end, we considered an optical fiber with a chaotically distributed index. The generated DW from such an index is represented in Figure 2-15.
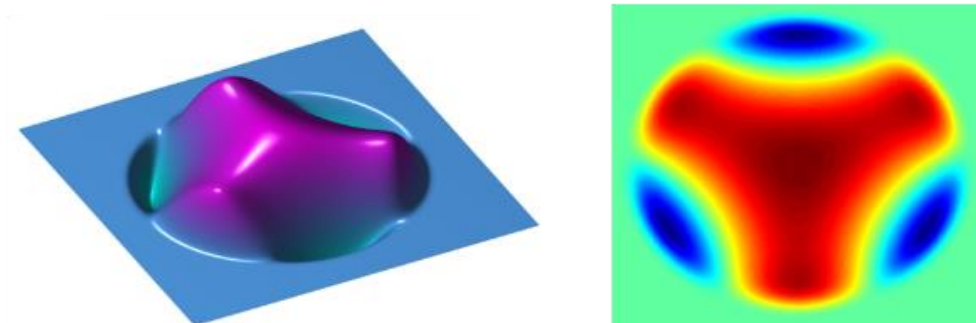
Figure 2-14 The refractive index distribution of a Hénon-Heiles chaotic potential
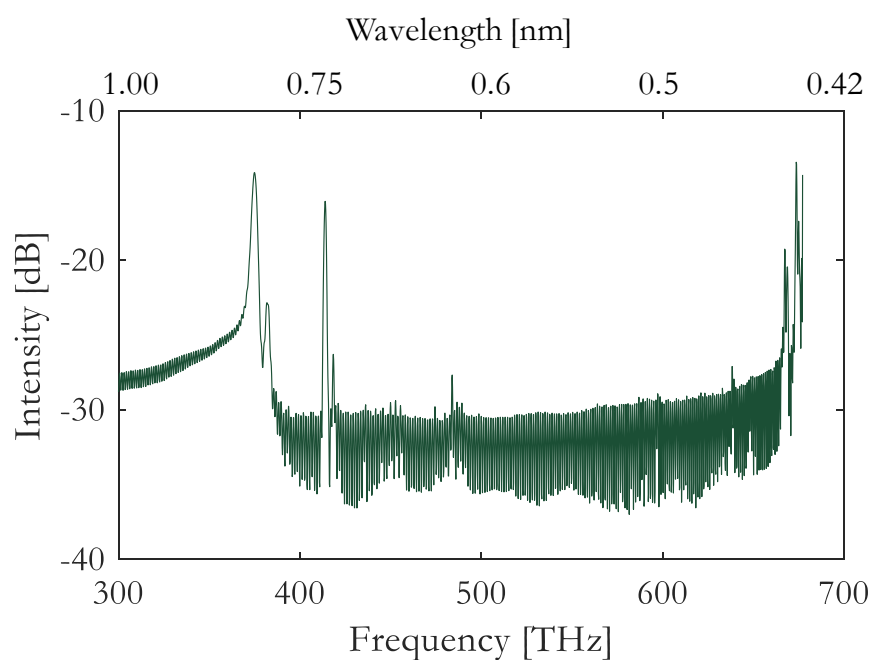
Figure 2-15 The DW form a fiber with a chaotic refractive index − obtained from a gUPPE simulator.

The output spectrum measured in the output of a chaotic fiber shows that this strategy can be

exploited for an efficient generation of spectral content on the visible side of the spectrum.

.

CHAPTER 3: TAILORING NONLINEAR PROCESSES THROUGH CONTROLING INITIAL CONDITIONS IN GRADED-INDEX MULTIMODE FIBERS

The results presented in this section have been published and can be found at : M. A. Eftekhar, L. G. Wright, M. S. Mills, M. Kolesik, R. Amezcua Correa, F. W. Wise, and D. N. Christodoulides, "Versatile supercontinuum generation in parabolic multimode optical fibers," Opt. Express **25**, 9078-9087 (2017) [37]

3.1 Introduction

Quite recently, the nonlinear "virtues" of nonlinear MMFs have been reconsidered in both the normal and anomalous dispersion regimes [23]. In this vein, the observation of multimode optical solitons in parabolic MMFs has been reported [24,38] – thus confirming earlier predictions [39,40]. Supercontinuum generation has also been successfully demonstrated in graded-index MMFs by launching ultra-short pulses in the anomalous dispersion region (1550 nm) [28,41]. In these experiments, discrete spectral components were observed in the visible domain – features that were subsequently explained through the interplay between spatiotemporal soliton oscillations and dispersive waves that are only possible in parabolic fibers [28]. In addition, efficient supercontinuum generation from the visible to near-infrared (when pumped in the normal dispersion regime, 1064 nm) was reported in low DGD parabolic MMFs [42] by making use of a newly observed mechanism – better known as geometric parametric instability [29,43]. Such MMF supercontinuum sources could potentially display spectral densities that are orders of magnitudes higher than those currently obtained in single-mode fiber systems [42]. Beam clean-up was also observed for the first time during SC generation [42,44]– an effect that is yet not fully understood. These latter studies all indicate that MMFs can provide a rich setting where nonlinear

effects can be potentially molded by exploiting the sheer complexity offered by a multitude of wave-mixing paths. Of importance will be to assess to what extent one can shape the output of such experiments through new degrees of freedom.

Here, we show that the input beam modal composition can provide two additional degrees of freedom in tailoring the output spectral content resulting from nonlinear interactions in graded-index multimode fibers. These two parameters directly stem from the indices (l, m) of the supported mode group LP_{lm}. Our study suggests that soliton fission and emission effects as well as dispersive wave generation, known to play an important role during SC, critically depend on the way the modes of this fiber are initially excited. Unlike single-mode fibers, initial beam conditions tend to affect multimode soliton velocities and their energy content. Numerical simulations based on a gUPPE approach [45,46] are in good agreement with previously reported experimental observations, carried out at 1550 nm [41].

3.2 Theory and Method

To demonstrate the effect initial spatial conditions, have on the generated SC spectra in heavily multimoded fibers, we first perform a series of numerical studies. The silica fiber under investigation is assumed to have a core diameter of 2a = 62.5 µm and a parabolic index profile (so as to minimize modal walk-off) with a maximum numerical aperture $NA = 0.275$. This MMF is excited at 1550 nm where the dispersion is anomalous and at which wavelength this structure is expected to support ~ 300 modes. Given that the number of propagating modes scales as $1/\lambda^2$, one would expect thousands of modes especially in the visible range. Clearly, simulating in full this complex environment on a mode-by-mode basis becomes quickly impractical, if not impossible. Each mode requires a pre-computed dispersion curve, and each nonlinear interaction is described by a pre-calculated tensor requiring billions or trillions of non-zero multi-dimensional integrals.

Even if these could be computed, coupled-mode models cannot accurately describe the full wavelength-dependence of modes and nonlinear interactions, especially near cut-off as occurs for many modes involved in our broadband spectra. In addition, a mode-by-mode methodology will fail to capture the ensued dynamics in such a broad parabolic index profile, even at moderate power levels where weak self-focusing effects are expected to present themselves. Hence, while such models can provide insight, for highly-multimode propagation especially, a full theoretical understanding absolutely requires rigorous full-field simulations based on the gUPPE [45,46]. This unidirectional pulse propagator (UPPE) allows one to model supercontinuum generation in highly multimode MMFs in a global manner, accounting for all possible nonlinear effects. In this respect, the evolution of the vectorial electric field is comprehensively described by

$$\partial_z \vec{E}(k_\perp, \omega, z) = i k_z \vec{E}(k_\perp, \omega, z) + \frac{i\omega^2}{2\epsilon_0 c^2 k_z} \vec{P}(k_\perp, \omega, z) - \frac{\omega}{2\epsilon_0 c^2 k_z} \vec{J}(k_\perp, \omega, z) \qquad (19)$$

where $k_z(k_\perp, \omega) = \sqrt{\omega^2 \varepsilon(\omega)/c^2 - k_x^2 - k_y^2}$ and $\varepsilon(\omega)$ is the frequency dependent permittivity of the medium with c representing the speed of light. The waveguide is represented as a static contribution to polarization $\vec{P}$ and is implemented as an additional module for the simulator. Equation (1) implicitly considers diffraction/waveguiding processes as well as dispersion and mode walk-off effects. Moreover, all the nonlinear interactions are included in the polarization and current terms, represented by $\vec{P}(k_\perp, \omega, z)$ and $\vec{J}(k_\perp, \omega, z)$ in (1), respectively. For the task at hand, the UPPE core is primed to account for all nonlinear phenomena such as self-phase and cross-phase modulation, four-wave mixing, third harmonic generation, shock-effects, Raman, etc. The nonlinear Kerr coefficient is $n_2 = 2.9 \times 10^{-20} m^2/W$ and its Raman fraction is taken here to be f = 0.18 in the standard two-parameter response model [47]. The wavelength dependence of the refractive index is provided through an appropriate Sellmeier series. In our studies, the current term (accounting for possible plasma and filamentation effects) in Eq. (1) played a negligible role.

3.3 Numerical and Experimental Results

In all our simulations, we assume that the input pulse energy is $E_{in} \approx 150 \ nJ$. The temporal pulse width is $\tau \approx 500 \ fs$ (FWHM) and the minimum waist spot-size (where the intensity drops by e^{-2}) of the input circular Gaussian beam is $w = 15 \ \mu m$. Evidently, different modal groups LP_{lm} will be excited depending on the position of the input Gaussian beam. In this case, the modal content can be directly obtained by projecting the input field profile on the orthogonal Gauss-Laguerre base functions. For example, if the beam launched is centered, only modes from the LP_{0m} group will be excited, i.e. having zero orbital angular momentum. To some extent, this modal population is akin to that associated with a vacuum squeezed or coherent state. For the parabolic fiber under consideration, the modal composition corresponding to an on-axis Gaussian beam excitation is shown in Figure 3-1(a). Meanwhile, if this same Gaussian beam is shifted by $10 \ \mu m$ with respect to the fiber center, the modal composition is significantly altered, as depicted in Figure 3-1(b). In this latter scenario, most of the energy no longer resides in the fundamental mode. Instead, the mode content does not monotonically decrease with m and in addition, modes with angular momenta are now involved (with LP_{1m} contributing the most).
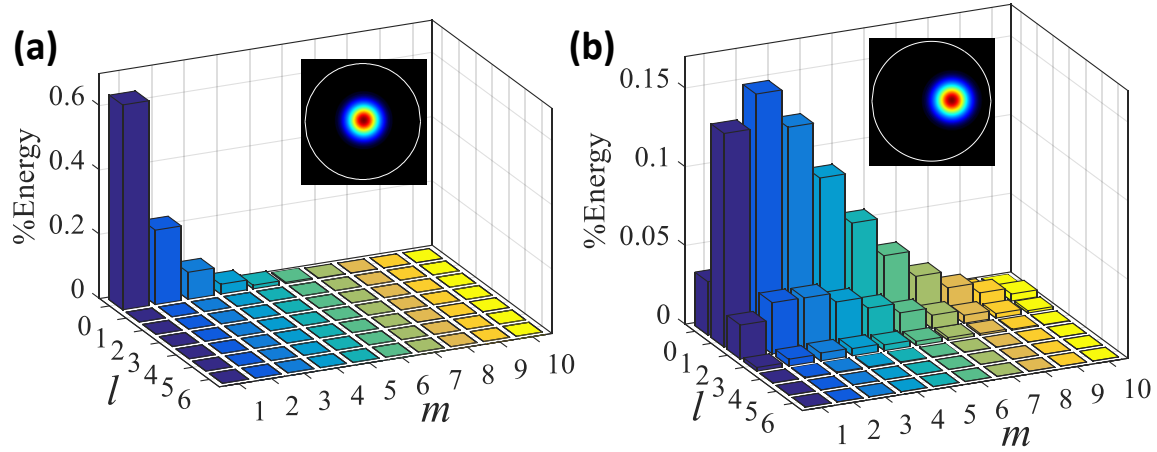
Figure 3-1 (a) Energy distribution among the LP_{lm} modes of a parabolic fiber when excited on-axis. In this case, only the LP_{0m} modes are populated with the fundamental mode taking most of the energy. (b) Modal population when the system is excited off-axis. For this input, considerable energy resides in the LP_{1m} set.

Under the aforementioned initial conditions, the evolution of the SC spectrum, as obtained from gUPPE simulations is shown in Figure 3-2. The supercontinuum features in Figure 3-2(a) result from an on-axis excitation, (corresponding to Figure 3-1(a)) while those in Figure 3-2(b) from an off-axis input (Figure 3-1(b)). Overall, these two figures show there is a significant difference in the way SC develops in this MMF, depending on the modal groups initially excited. If the fiber is excited on-axis with a spot-size different than that of the fundamental mode, the beam experiences periodic contractions and expansions. Meanwhile, if the Gaussian wavefront is launched off-axis, in addition to the aforementioned effects, the beam tends to oscillate around the fiber center [48].

As Figure 3-2 indicates, in both cases, the spectrum rapidly broadens with propagation distance. Three stages of spectral evolution are clear in this figure. During the first stage, the spectrum gradually expands and the temporal and spatial profiles of the pulsed beam continuously contract. In addition, the periodic compression/expansion of light that results from modal interference, an innate property of parabolic-index optical fibers, leads to a geometric parametric instability (GPI) which manifests itself as narrow line sidebands symmetrically located around the pump frequency

ω_p [29,42,43]. The angular frequency of the generated mth sideband can be obtained from $\omega_{SB_m} \simeq$

$\omega_p \pm \sqrt{m}\, \omega_G$, where $\omega_G^2 = 2\delta/|k_0''|$. Here $\delta = a^{-1}\sqrt{2\Delta}$ represents the spacing between the

propagation constant eigenvalues, $|k_0''|$ is the fiber dispersion at the pump wavelength, and $\Delta =$

$(n_{core} - n_{clad})/n_{core}$. In our experiments, $\Delta = 0.0165$, and $|k_0''| = 2.8 \times 10^{-26} m^{-1}s^2$. For

these parameters, the first three visible sidebands are expected to appear at 296, 338, and 371 THz

while the first NIR sideband at 91.2 THz. These sidebands are easily discernable in Figure 3-2(b).

Interestingly, however, this is not the case in Figure 3-2(a). This can be understood by keeping in

mind that the GPI process is a direct byproduct of modal interference. In the first case, when the

system is excited on-axis with a spot size close to that of a fundamental mode (most of the energy

resides in LP_{01}), the ensued GPI is weak and hence little energy is transferred to the sidebands. On

the other hand, when the MMF is excited off-axis, the compression/expansion cycles are more

severe and the GPI gain is, therefore, higher, as indicated in Figure 3-2(b).
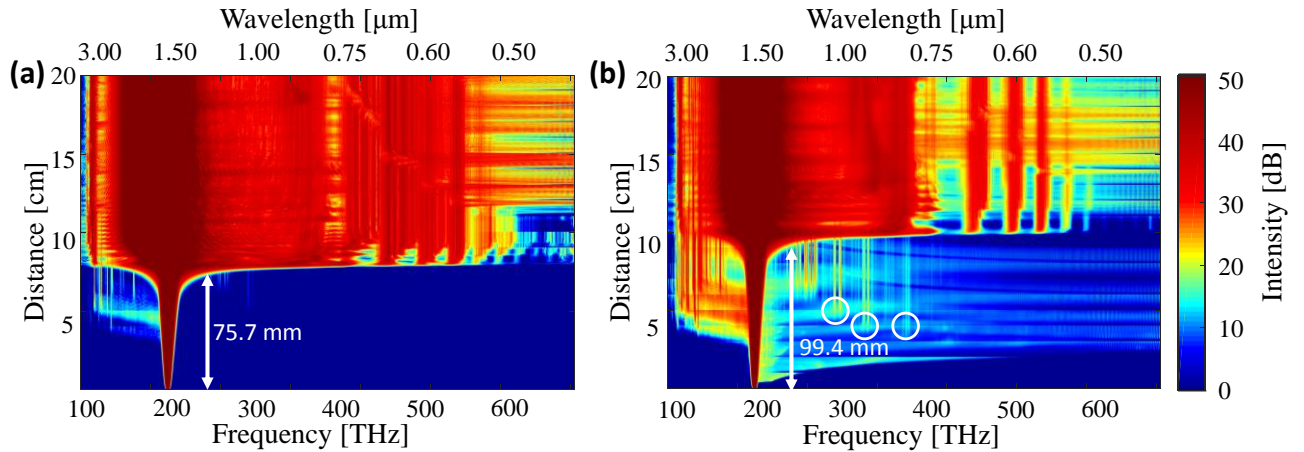
Figure 3-2 Evolution of the supercontinuum spectrum in a 20 cm long parabolic MMF when the pulse energy is 150 nJ for (a) an on-axis excitation (b) off-axis input (offset by 10 µm). In all cases, three stages are apparent: (i) initial spectral broadening, (ii) soliton fission, and (iii) soliton and dispersive wave propagation. The respective distances where soliton fission occurs are also shown. In (b) the circles denote the onset of the first three GPI sidebands. The pump wavelength is 1550 nm.

During the second stage, the input pulse, having enough energy to support multiple solitons, breaks into a series of distinct fundamental multimode soliton components. Each soliton, generated in this soliton fission stage (in the anomalous dispersion regime) has different properties or modal composition. Each produces linear dispersive waves in the normal dispersive region with correspondingly different characteristics. The distance at which this process occurs, not only depends on the input energy and dispersion, but also on the initial spatial conditions. In fact, since each spatial mode satisfies a different dispersion relation, the way the input energy is distributed among modes determines the effective dispersion and thus directly affects the fission distance. As it can be seen in Figure 3-2(a), for on-axis excitation, the pulse undergoes fission after 76 mm of propagation, while for the off-axis case it takes place at 99 mm (Figure 3-2(b)).

During the third stage, the co-propagation of solitons and dispersive waves in the MMF is responsible for supercontinuum generation, through the interplay of all the aforementioned processes. The spectra developed after 20 cm of propagation, corresponding to the on-axis and off-axis initial conditions of Figure 3-1, are depicted in Figure 3-3. Both Figure 3-2 and Figure 3-3 reveal significant differences in the resulting spectral features, suggesting that initial conditions indeed matter in supercontinuum generation. Launching the pulse on-axis leads to more intense multimode solitons, capable of experiencing stronger Raman self-frequency shifts in the infrared region. The gradual redshifting of solitons is accompanied by a gradual drift of their dispersive waves toward shorter wavelengths. This redshifting effect along with the ensuing FWM mechanism results into a rather flat spectrum. On the other hand, exciting the fiber off-axis produces distinct dispersive wave components in the visible (Figure 3-3, red curve) that do not drift toward higher frequencies since the generated solitons are less susceptible to redshifting.
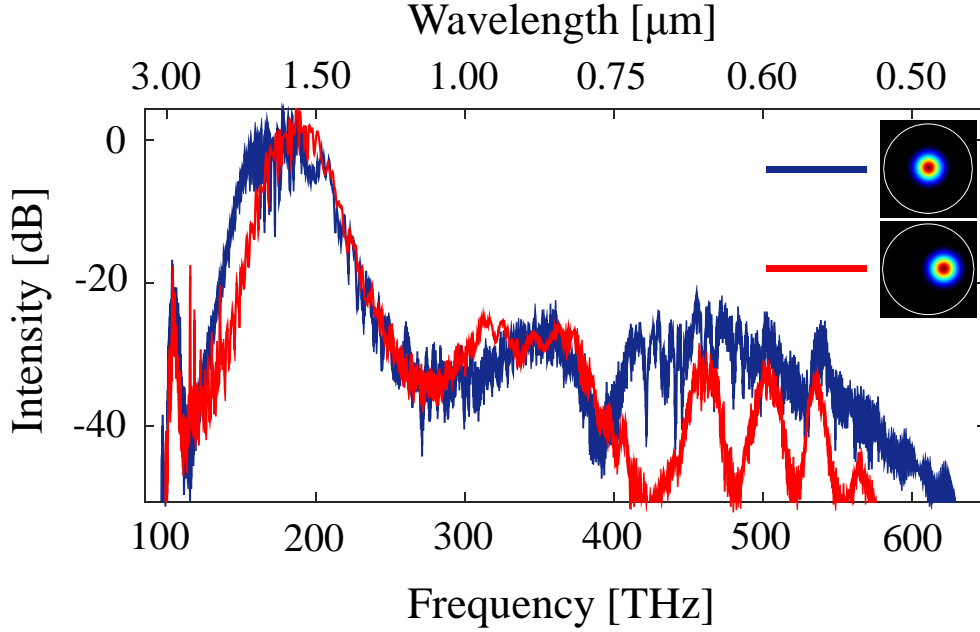
Figure 3-3 Comparison of the supercontinuum spectra features produced in an anomalously dispersive parabolic MMF for on-axis (blue) versus off-axis (red) excitation conditions. The propagation distance is 20 cm and the pulse width is 500 fs. All other parameters are the same as Figure 3-2.

This sensitivity of the emergent spectral features to the initial modal composition or spatial launching conditions can only be understood by taking a closer look at the temporal and spatial behavior of the elements involved in this process (Figure 3-4 (a)-(f)). Figure 3-4 (b) and (d) show the temporal evolution of the input pulse (500 fs, 150 nJ) in our parabolic MMF during the first 20 cm of propagation distance, under on-axis and off-axis excitation conditions, respectively. As can be inferred from the slopes of the traces, which are representatives of wavepacket velocities with respect to the moving frame, the fission generated solitons from an on-axis input propagate much slower than those resulting from an off-axis excitation. For these two scenarios, the spatial intensity distribution associated with the slowest and more pronounced solitons is depicted by the insets in Figure 3-4 (e) and Figure 3-4 (f). For clarity, these same figures also provide *x*-cross-sections of these intensity profiles (red curves). Moreover, the modal composition of these primary

solitons has been numerically estimated by projecting their spatial fields on the constituent LP_{lm} modes of the MMF at that particular wavelength (energy distributions in Figure 3-4 (e) and Figure 3-4 (f)). These results demonstrate that the solitons generated from on-axis excitation reside mostly in the fundamental mode while higher order modes like LP_{02}, LP_{11}, etc. jointly share only 10 percent of its energy. However, for off-axis excitation conditions, the resulting solitons are heavily multimoded, with more than 40 percent of their energy distributed among higher-order spatial modes. Since the fundamental mode in the former case, dominates in terms of energy, the Raman self-frequency shift is expected to be more pronounced. As indicated in previous studies [49], this is because the LP_{01} mode typically enjoys a higher Raman gain – a direct by-product of the overlap integrals. This explains why the generated solitons under off-axis conditions experience less Raman deceleration and hence move faster. In addition, the modes involved, as initially dictated by launching conditions, dynamically exchange energy during propagation as a result of wave-mixing and Raman processes. Figure 3-4 (a) and (c) show the temporal features at the output of the fiber. In both cases, the solitons have a pulse-width of 18-20 fs. However, the energy each soliton carries depends again on initial conditions. In fact, for an on-axis input, the first generated soliton contains almost 40% of the total energy.
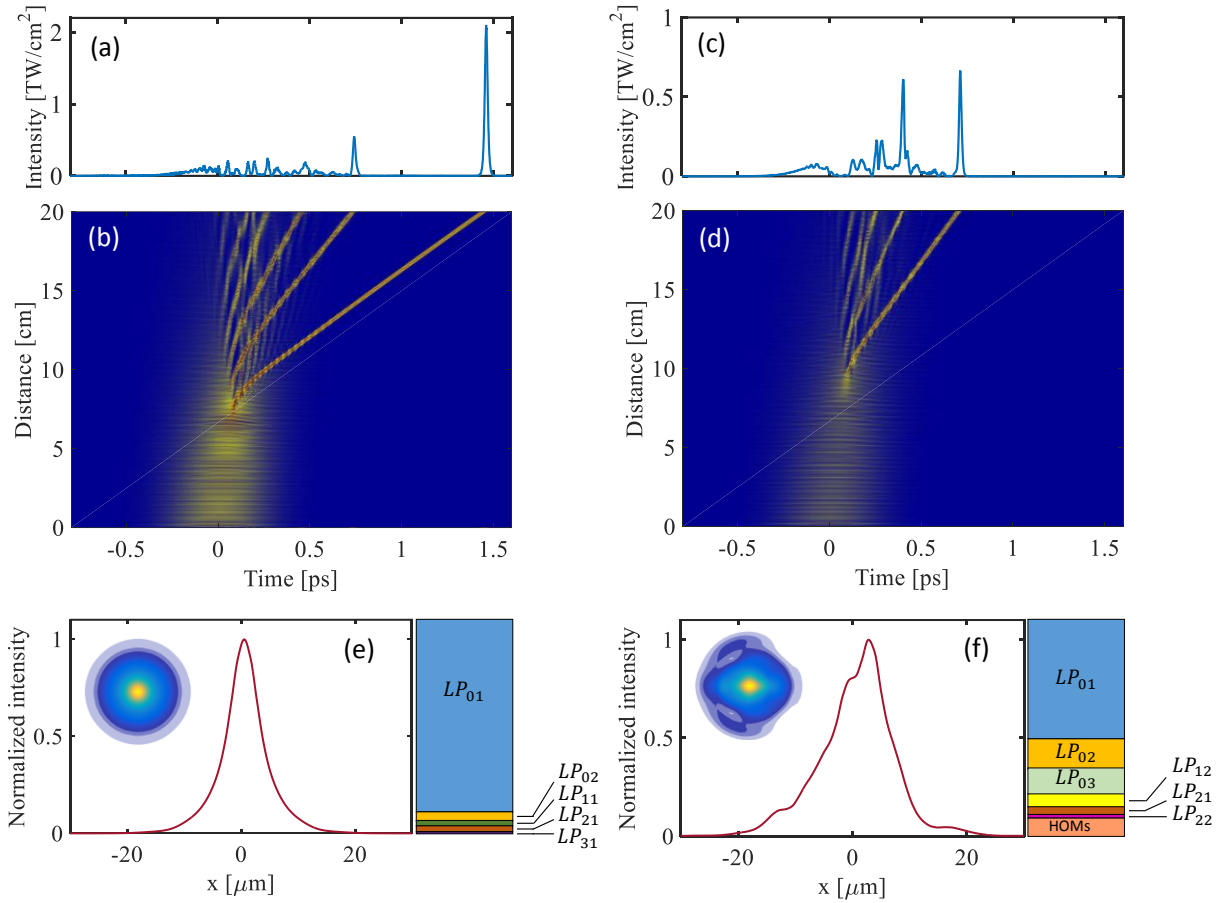
Figure 3-4 Resulting temporal features after 20 cm in a parabolic MMF when excited on axis. (b) Temporal evolution of the initial 500 fs pulse (150 nJ) corresponding to (a). The emergence of slow solitons is apparent. (c) and (d) Same as in (a) and (b), respectively, for off-axis excitation. (e) The spatial intensity profile and its x-cross section corresponding to the slowest dominant soliton at the end of the fiber, when illuminated with an on-axis Gaussian beam. (f) Same as in (e) for off-axis launching conditions, where the soliton-beam experiences transverse oscillations during propagation.

The simulations show good agreement with experiments [41]. In our experiments, an amplified fiber laser operating at 1550 nm and emitting pulses with a ~ 500 fs pulse-width, was coupled into ~ 1 m long fibers with the same parameters used in our numerical studies. By translating the fiber with respect to the optical lens, the initial conditions were varied. The Gaussian mode field diameter at the input was about 30 μm. Figure 3-5 (a) and (b) show, respectively, the NIR and visible portions of the output spectra resulting from an on-axis excitation. Figure 3-5 (c) and (d),

on the other hand, depict the spectra for the off-axis case (~10-15 µm displacement). The near-field beam profile, integrated over all wavelengths, corresponding to each of these measurements is shown on the right of each figure. In agreement with our numerical results, we observe that most of the energy resides in the fundamental mode, thus causing significant redshifting towards NIR from the generated solitons (Figure 3-5 (a)). Meanwhile, by moving the input beam away from the center, the frequency generation in the NIR region is considerably subdued (Figure 3-5 (c)). As also predicted by our simulations, the visible component of the spectrum, depicted in Figure 3-5 (b) for on-axis, exhibits appreciable frequency generation over a broad range while the output spectrum resulting from an off-axis excitation displays instead a series of distinct peaks (Figure 3-5 (d)).
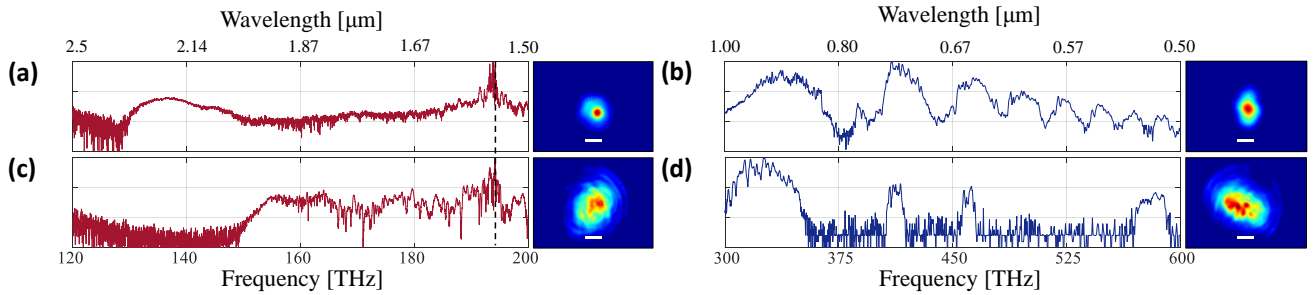
Figure 3-5 Experimentally measured (a) NIR and (b) visible supercontinuum spectrum for on-axis excitation together with generated transverse output intensity profiles after 1 m of propagation. (c) and (d), Same as in (a) and (b) for an off-axis excitation. In all cases, each division represents a 10 dB variation. The scale bars in the insets represent 20 µm.

Our results clearly indicate that changing the initial spatial conditions can have a significant effect on the spatial and temporal evolution of the multimoded field which accordingly alters the frequency generation process. Thus far, we have mostly studied the effect of LP_{0m} (with the fundamental mode dominating) and LP_{1m} modes on the output spectrum. Yet, a plethora of other initial conditions can in principle be synthesized, with each one leaving a different imprint on the output. As an example, we here theoretically investigate two other possibilities. In the first case,

the fiber is illuminated with a ring pattern having a radius of 25 μm and a FWHM of 4.5 μm. Under these conditions, 80% of the total energy is distributed among the LP_{06}, LP_{07}, and LP_{08} group of modes, with the LP_{07} possessing most of the energy. The share of the first five LP_{0m} modes, including the fundamental, remains below 5%. The peak intensity and energy of the pulses used are the same as in Figs. 3-2 – 3-5. Figure 3-6 (a) and (b) show the NIR and visible portions of the output spectrum after 20 cm of propagation. As it can be inferred from Figure 3-6 (a), the self-frequency shift of the generated multimoded solitons is rather small. This can be attributed to the fact that higher LP_{0m} modes tend to experience lower Raman gains. Interestingly, however, this same modal composition leads to a considerable enhancement of supercontinuum in the visible portion of the spectrum (400-600 THz), as shown in Figure 3-6 (b). This enhancement is closely related to a more efficient generation of dispersive waves via Raman solitons. Meanwhile, the component between 300-400 THz – arising from dispersive waves emitted at the pump wavelength (PDWs) – is suppressed.
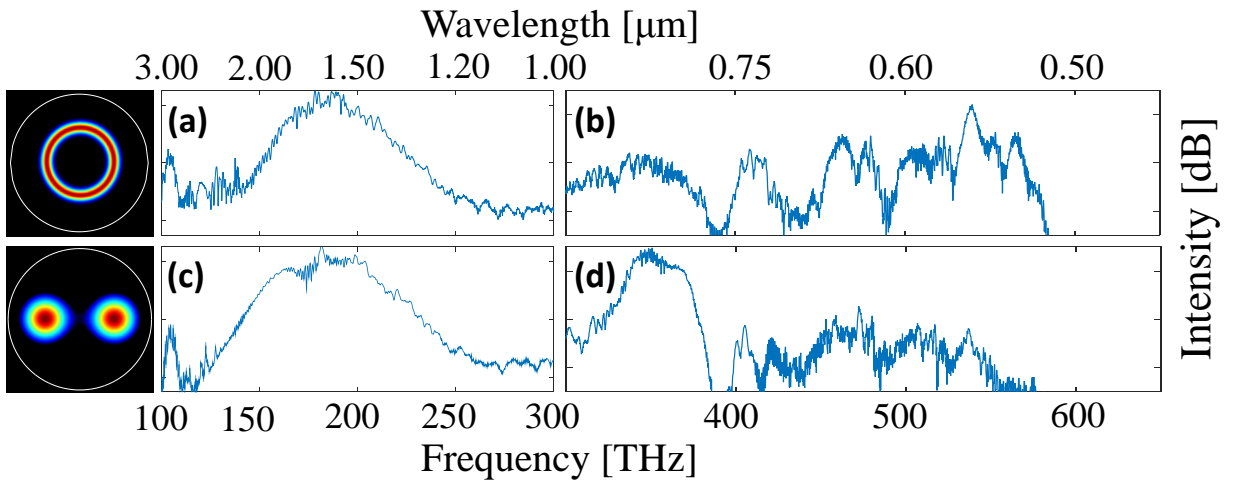
Figure 3-6 Generated (a) NIR and (b) visible portion of the spectrum when the fiber is excited by a ring beam. Same as in (c) and (d) when using a two-spot excitation. Each division in (a) and (c) represents a 20 dB differential while in (b) and (d) a 10 dB variation.

As a second example, we consider the case of symmetrically exciting the fiber with two spots in phase, akin to a quantum cat-state $|\psi\rangle + |-\psi\rangle$. This state results in the elimination of all $LP_{2k-1,m}$ modes where k is a positive integer. In our simulations, the fiber is excited with two Gaussian beams, separated by 20 μm. Each of these two displaced Gaussian beams is identical in size with those used in Figs. 3-2 − 3-4 and carries half of the total energy (75 nJ). In this arrangement, the energy is distributed among the LP_{0m} and LP_{2m} group of modes, with the fundamental mode having the largest share. Figure 3-6 (c) shows the resulting NIR supercontinuum spectrum. As expected, the Raman process is now more pronounced given that a larger portion of the energy is injected in the fundamental mode. On the other hand, the visible section of the spectrum, shown in Figure 3-6 (d), indicates that this symmetric excitation leads to a notable enhancement in the 300-400 THz band (arising from PDWs) while the higher frequencies are subdued.

Figure 3-7 shows experimental results corresponding to four different initial spatial conditions. In all cases, the generated supercontinuum spectrum is highly sensitive to the modal groups initially excited. The integrated output beam profiles in the visible and NIR are also depicted. While in Figure 3-7 (b) the spectral features are comb-like, in (d) they are more broad and flat, similar to observations in our simulations (Figure 3-6 (b) and (d)). Similar conclusions also hold for the experimental observations of Figure 3-7 (a) and (c).
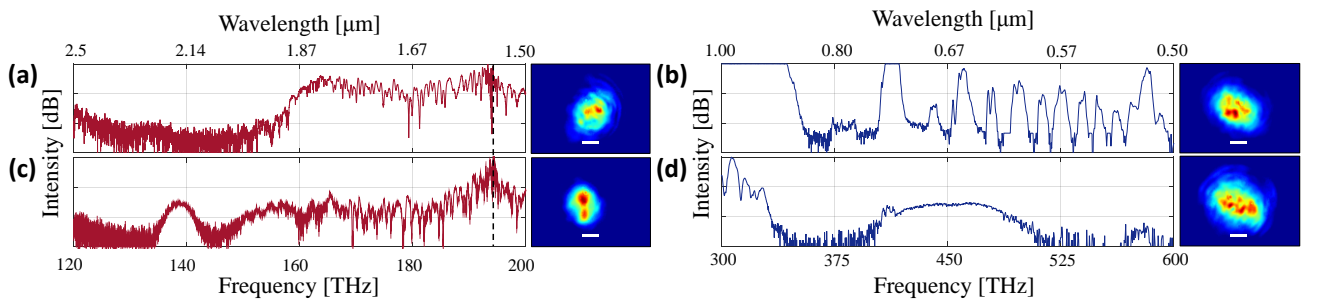
Figure 3-7 Experimentally measured NIR and visible supercontinuum spectra for four different initial spatial conditions together with generated transverse output intensity profiles after 1m of

propagation. In all cases, the pulse energy is 150 nJ. In all cases, each division represents a 10 dB variation. The scale bars in the insets represent 20 µm.

3.4 Conclusion

In conclusion, we have shown that parabolic multimode fibers can provide a versatile platform for tailoring supercontinuum generation. Experiments and simulations carried out in the anomalous dispersive region indicate that the modal composition (energy distribution and phase relationship among eigenmodes) of the input beam plays an important role in altering the output spectrum. This is accomplished through the interplay of soliton fission processes, Raman, dispersive wave generation and four-wave mixing. Our results could pave the way for new classes of optical sources with pre-engineered spectra and unprecedented high spectral densities.

CHAPTER 4: NONLINEAR DYNAMICS IN THE PRESENCE OF ACCELERATED NONLINEAR PROCESSES

4.1 Abstract

Multimode optical fibers have recently reemerged as a viable platform for addressing a number of long-standing issues associated with information bandwidth requirements and power-handling capabilities. As shown in recent studies, the complex nature of such heavily multimoded systems can be effectively exploited to observe altogether novel physical effects arising from spatiotemporal and intermodal linear and nonlinear processes. As such, multimode optical solitons, spatial beam self-cleaning, geometric parametric instabilities, and spatiotemporal mode-locking have been lately reported in multimode waveguide settings. In this work, we study for the first time, accelerated nonlinear intermodal interactions in core-diameter decreasing multimode fibers. We demonstrate that this spatiotemporal acceleration can have a prominent effect on the ensued temporal and spectral behavior in both dispersion regimes. Under normal dispersive conditions, we observe a generation of accelerating frequency bands that dynamically sweep the entire spectrum. This, in turn, can be utilized to produce a notably flat and uniform supercontinuum, extending over 2.5 octaves. On the other hand, in the anomalous dispersion regime, this same mechanism leads to a peculiar class of relatively blue-shifted multimode solitons and introduces a new process for establishing blue-drifting dispersive wave combs through speeding up the collision dynamics among the constituent modes of multimode solitons.

4.2 Introduction

Multimode fiber systems offer a promising avenue for overcoming some of the physical limitations associated with single mode structures. The ever-increasing demand for higher data-carrying capacities has incited a flurry of activities [18,50–52] that not only led to new classes of active and

passive multimode fiber components [20,21] but it has also prompted a critical rethinking as to how linear/nonlinear processes can be exploited in multimode environments [20,21,53–65,25,66,29,42] – an aspect that has so far remained largely unexplored. In this respect, the added spatial degrees of freedom provide further opportunities at both the scientific and technological level that were previously overlooked and remained unattainable because of technological barriers. From a more fundamental perspective, such hyperdimensional multimode systems provide an ideal testbed for investigating complex linear and nonlinear modal interactions [25,29,59–66] – akin to those taking place in many-body molecular dynamics [67]. In recent experiments, nonlinear wave propagation in graded-index multimode fibers (MMFs) was found to lead to a series of unexpected results that are otherwise impossible in single-mode waveguides [25,28,29,42,65,66,68]. These include, for example, the first observation of the so-called geometric parametric instability [29,42], modal condensation [42,68,69], formation of multimode soliton "molecules" [25,65], efficient and instant second-harmonic generation [70], and visible supercontinuum generation [42,71] that rivals that obtained from dispersion engineered photonic crystal fibers [6,72]. What makes this possible is the immense spatiotemporal complexity associated with these nonlinear wave-mixing mechanisms in the presence of a large number of modes [25].

Geometric parametric instabilities naturally arise in parabolic MMFs because of periodic beam compression/expansion, resulting from the equidistant distribution of the propagation eigenvalues in such 2-D harmonic potentials [43]. This, in turn, causes a longitudinal modulation of the optical intensity and hence forces all the modes to nonlinearly interact or collide periodically with each other, thus giving rise to new spectral sidebands, as lately observed in a number of studies, especially in conjunction with supercontinuum generation in the visible region [42,71]. Another intriguing process that is unique to nonlinear multimode systems is that of spatial beam self-

cleaning. This self-organized effect is induced by the Kerr nonlinear energy exchange between the many modes involved and always occurs irrespective of initial conditions [42,68,69]. Unlike, Raman beam clean-up, this modal energy transfer tends to thermodynamically populate lower-order modes in an effort to maximize the system's entropy [73]. The aforementioned aspects could be of importance in realizing high power optical sources based on MMF technologies. Indeed, the prospect of simultaneously locking multiple spatial and longitudinal modes in multimode fiber lasers was successfully demonstrated in a recent work [74].

Here, we explore for the first time accelerated spatiotemporal nonlinear dynamics in long-tapered parabolic-index multimode fibers. As opposed to single-mode fiber tapers, where the axially varying dispersion plays a key role during nonlinear evolution [14], the dispersion in our tapered multimode system remains invariant and the resulting nonlinear interactions are now predominated and drastically altered by the induced accelerated intermodal dynamics – irrespective of the dispersion regime. The ensued nonlinear modal collisions in this "many-body" system (Figure 4-1(a)) leads to a host of unexpected results. Under normal dispersive conditions, we observe the formation of upshifted and downshifted gain spectral bands that progressively drift away from the pump wavelength as the intermodal oscillations speed up. In turn, this mechanism leads to the generation of a markedly flat and uniform spectrum that extends over several octaves with large spectral power densities. Meanwhile, in the anomalous dispersion regime, this acceleration process results in a pronounced change of soliton behavior: the emerging multimode solitons (MM-solitons) go through a series of self-adjusting phases that destabilize their spatial distribution along propagation. At the same time, some of these solitons experience an unexpected temporal slowdown in their Raman-induced deceleration, because of a cross-phase modulation interaction between the MM-solitons and slow, broadband dispersive waves – a process never observed

before. Finally, we observe a dispersive wave (DW) comb in the spectrum that continuously blue-drifts, not because of soliton trapping, but as a result of accelerated MM-soliton intermodal collisions in the tapered MMF system.

 4.3 <u>Accelerated Spatiotemporal Dynamics in Anomalously Dispersive MMF Tapers</u>
Solitons are ubiquitous entities that appear in many and diverse physical settings, ranging from fluids, plasmas, nonlinear optics, and solid-state physics, to mention a few [75–78]. In single-mode optical fibers (SMF), temporal solitons represent nonlinear 'modes' or stationary states of the underlying (1+1) D nonlinear Schrödinger equation – a process enabled by balancing self-phase modulation (SPM) and dispersive effects [22,76,79]. While in three-dimensional bulk environments, optical solitons happen to be inherently unstable, their stability can be reestablished in multimoded waveguides. Unlike solitons in SMFs that have been intensely investigated over the years, their counterparts in MMFs still remain largely unexplored. Quite recently, multimode solitons have been successfully observed [65] for the first time in anomalously dispersive parabolic fibers, thus corroborating earlier theoretical results [39]. What makes multimode solitons so complex and rich in dynamics is not only their modal composition but also their intricate intermodal space-time interactions. As opposed to solitons in single mode fiber systems that can be uniquely determined by their energy content, for multimode solitons the situation is considerably more convoluted. This is because the MM-soliton 'molecules' can, in principle, take several different forms depending on their modal make-up [25,80]. These composite soliton structures are formed when the constituent modes nonlinearly coalesce after appropriately shifting their frequencies in order to overcome intermodal group-velocity walk-offs. Hence, the soliton fission process, as well as the ensued MM-solitons and corresponding DWs, can be modified by judiciously engineering the modal structure of the input beam [80]. In parabolic-index MMFs, the

self-imaging behavior associated with multimode solitons leads to a periodic nonlinear interaction of the modal elements. This, in turn, gives rise to a broadband sequence of DWs, which in principle can extend into the UV [28]. Here, we investigate for the first time how accelerated interactions can affect the soliton fission mechanism and the subsequently generated multimode solitons along with their Cherenkov radiation.

To understand these effects, we must first consider the speeding up of the beam expansion/compression cycles in a tapered MMF. In our experiments, the core radius, $a(z)$, of the parabolic MMF was approximately exponentially tapered along the propagation direction, i.e. $a(z) = a_0 \, exp(-\gamma z/2)$, where a_0 is the initial core radius and γ is the tapering rate. Therefore, the core-index potential of this system can be described by $n^2 = n_0^2 \, (1 - 2\Delta(r/a_0)^2 e^{\gamma z})$ where Δ represents the relative index change between core and cladding. In seeking Gaussian beam solutions in this parabolic-index arrangement, we use the following ansatz for the spatial part of the optical electric field envelope: $E(r,z) = A(z)exp\left(-\frac{r^2}{2w^2(z)}\right) e^{i[\theta(z)+r^2F(z)]}$. The accelerated evolution of the beam spot-size during propagation in the tapered MMF is given in the below section.

The refractive index profile of a non-uniform optical fiber can be represented as below:

$$n = n_0 \left(1 - \Delta \left(\frac{r}{a_0}\right)^2 f(z)\right) \qquad (20)$$

By replacing the above index profile in the Helmholtz equation ($\nabla^2 E + k_0^2 n^2 E = 0$), we acquire the field evolution equation in a fiber profile with z-dependent core radius. Next, we employ the slowly varying envelope approximation (SVEA) $E(x,y,z) = \Phi(x,y,z)e^{ik_0 n_0 z}$. By decomposing the operator ∇^2 to longitudinal and transverse components ($\nabla^2 = \partial_{zz} + \nabla_\perp^2$) we will have:

$$\nabla^2 E + k_0^2 n^2 E = (\partial_{zz} + \nabla_\perp^2)E + k_0^2 n^2 E$$

$$\Phi_{zz} + 2ik_0 n_0 \Phi_z - k_0^2 n_0^2 \Phi + \nabla_\perp^2 \Phi + k_0^2 n^2 \Phi = 0 \qquad (21)$$

By replacing the index profile $n(z)$ we get:

$$\Phi_{zz} + 2ik_0 n_0 \Phi_z - k_0^2 n_0^2 \Phi + \nabla_\perp^2 \Phi + k_0^2 n_0^2 \Phi - 2\Delta \left(\frac{r}{a_0}\right)^2 f(z) k_0^2 n_0^2 \Phi = 0$$

$$i\Phi_z + \frac{1}{2k_0 n_0} \nabla_\perp^2 \Phi - \Delta \left(\frac{r}{a_0}\right)^2 f(z) k_0 n_0 \Phi = 0 \qquad (22)$$

One way to solve this differential equation is through a separation of variables:

$$\Phi = F(x,z)G(y,z)$$

Which gives

$$\frac{iF_z}{F} + \frac{iG_z}{G} + \frac{1/F}{2k_0 n_0} \nabla_\perp^2 F + \frac{1/G}{2k_0 n_0} \nabla_\perp^2 G - \Delta \left[\left(\frac{x}{a_0}\right)^2 + \left(\frac{y}{a_0}\right)^2\right] f(z) k_0 n_0 = 0 \quad (23)$$

Separating the terms independent of x and y gives:

$$iF_z + \frac{1}{2k_0 n_0} F_{xx} - \Delta \left(\frac{x}{a_0}\right)^2 f(z) k_0 n_0 F = 0$$

$$iG_z + \frac{1}{2k_0 n_0} G_{yy} - \Delta \left(\frac{y}{a_0}\right)^2 f(z) k_0 n_0 G = 0 \qquad (24)$$

Since both the equations are essentially identical, one needs to solve only one of them. The evolution equation under consideration is as below:

$$iu_z + \frac{1}{2k_0 n_0} u_{xx} - \Delta \left(\frac{x}{a_0}\right)^2 f(z) k_0 n_0 u = 0 \qquad (25)$$

The above equation is normalized through applying the following normalization parameters.

$$\xi = \frac{z}{a_0}\sqrt{2\Delta}, \ s = \frac{x}{x_0}, \ x_0^2 = \frac{a_0}{\sqrt{2\Delta}}\frac{1}{k_0 n_0} \qquad (26)$$

Where x_0 is the spot-size of the fundamental mode. By applying the normalization parameters one gets:

$$i\frac{\partial u}{\partial \xi} + \frac{1}{2}\frac{\partial^2 u}{\partial s^2} - \frac{s^2}{2}f(\xi)u = 0 \tag{27}$$

We assume a Gaussian-type solution for the evolution equation as below

$$u(s,\xi) = A(\xi)\ e^{-\frac{s^2}{2w^2(\xi)}}\ e^{i[\theta(\xi)+s^2 F(\xi)]} \tag{28}$$

where $w(\xi)$ is the beam waist

$$u_\xi = \left[A' + A\left(i\theta' + is^2 F' + \frac{s^2}{w^3}w'\right)\right]e^{-\frac{s^2}{2w^2(\xi)}}\ e^{i[\theta(\xi)+s^2 F(\xi)]} \tag{29}$$

$$u_{ss} = A\left(\frac{s^2}{w^4} - \frac{i4s^2 F}{w^2} - 4s^2 F^2 + 2iF - \frac{1}{w^2}\right)e^{-\frac{s^2}{2w^2(\xi)}}\ e^{i[\theta(\xi)+s^2 F(\xi)]} \tag{30}$$

$$iA' - A\theta' - As^2 F' + i\frac{s^2}{w^3}Aw' + \frac{As^2}{2w^4} - \frac{i2s^2 FA}{w^2} - 2s^2 F^2 A + iFA - \frac{A}{2w^2} - \frac{s^2}{2}f(\xi)A = 0 \tag{31}$$

By separating real and imaginary parts as well as terms with different powers of s:

$$2F' = \frac{1}{w^4} - 4F^2 - f(\xi) \tag{32}$$

$$\theta' + \frac{1}{2w^2} = 0 \tag{33}$$

$$\frac{w'}{w^3} - \frac{2F}{w^2} = 0 \tag{34}$$

$$A' + FA = 0 \tag{35}$$

From the relation (34):

$$w' - 2Fw = 0,$$

$$F = w'/2w$$

Replacing F in the equation (35) gives:

$$A' + w'/2wA = 0$$

$$2A'Aw + w'A^2 = 0$$

$$(A^2 w)' = 0$$

$$A^2 w = Const. \qquad (36)$$

Equation (36) is a manifestation of conservation of energy. By replacing F and F' in Eq. (32) one arrives to the following equations:

$$4F^2 = \frac{w'^2}{w^2}$$

$$2F' = \frac{w''}{w} - \frac{w'^2}{w^2}$$

$$2F' = \frac{1}{w^4} - 4F^2 - f(\xi)$$

$$\frac{w''}{w} - \frac{w'^2}{w^2} = \frac{1}{w^4} - \frac{w'^2}{w^2} - f(\xi)$$

$$w'' + f(\xi)w = \frac{1}{w^3}$$

$$\frac{d^2 w(\xi)}{d\xi^2} + f(\xi)w(\xi) = \frac{1}{w(\xi)^3} \qquad (37)$$

Equation (378) is called Ermakov (Yermakov) equation

To solve the Ermakov equation, one needs to first solve the homogenous second order linear equation.

$$y''_{xx} + f(x)y = 0$$

Assuming a solution $Q(x)$ to this homogenous equation

$$Q''_{xx} + f(x)Q(x) = 0$$

Then by applying the transformation below it simplifies the equation.

$$\zeta = \int \frac{dx}{Q^2(x)}, \quad z = \frac{y}{Q(x)}$$

Which gives

47

$$z''_{\zeta\zeta} = az^{-3}$$

The exact solution to the equation above is given from

$$C_1 y^2 = aQ^2 + Q^2 \left(C_2 + C_1 \int \frac{dx}{Q^2(x)} \right)^2 \qquad (38)$$

To solve the above equation we need to first define the function $f(\xi)$. From Eq. (1), we know that:

$$n^2 = n_0^2 \left(1 - 2\Delta \left(\frac{r}{a_0} \right)^2 f(z) \right)$$

$$a(z) = a_0 e^{-\alpha z}$$

$$f(z) = e^{2\alpha z} \qquad (39)$$

As an example, if the fiber is gradually changing in radius from $30 \ \mu m$ to $10 \ \mu m$ over a course of $25 \ m$:

$$\alpha(0) = a_0 = 30 \ \mu m$$

$$a(25) = a_0 e^{-25\alpha} = 10 \ \mu m$$

$$e^{-25\alpha} = \frac{1}{3}$$

$$\alpha = \frac{\ln(3)}{25} = 0.0439445$$

$$\xi = \frac{z}{a_0} \sqrt{2\Delta} \qquad (40)$$

$$z = \frac{\xi a_0}{\sqrt{2\Delta}}$$

$$f(\xi) = e^{2\alpha \frac{a_0}{\sqrt{2\Delta}} \xi}$$

To see the evolution of the beam waist during propagation, the following equation must be first solved:

$$\frac{d^2 w(\xi)}{d\xi^2} + e^{2\alpha \frac{a_0}{\sqrt{2\Delta}} \xi} w(\xi) = \frac{1}{w(\xi)^3} \qquad (41)$$

For simplicity, we apply the change of variable $\beta = \alpha \frac{a_0}{\sqrt{2\Delta}}$.

The homogeneous equation is as below:

$$\frac{d^2 Q(\xi)}{d\xi^2} + e^{2\beta\xi} Q(\xi) = 0 \qquad (42)$$

We know that for the following equation

$$y''_{xx} + ae^{\lambda x} y = 0, \quad \lambda \neq 0 \qquad (43)$$

The solution is as

$$y = C_1 J_0(z) + C_2 Y_0(z), \quad z = \frac{2}{\lambda}\sqrt{a}e^{\lambda x/2} \qquad (44)$$

Thus, the solution to this equation will be

$$Q(\xi) = A J_0\left(\frac{e^{\beta\xi}}{\beta}\right) + B Y_0\left(\frac{e^{\beta\xi}}{\beta}\right) \qquad (45)$$

Having $Q(\xi)$ we know that the complete solution will be

$$C_1 w^2 = Q^2 + Q^2 \left(C_2 + C_1 \int \frac{d\xi}{Q^2(\xi)}\right)^2$$

Taking the integral of the inverse square of $Q(\xi)$ is very difficult nay impossible. The question is if there is any other way to simplify this integral. We should first check the typical values for β. For our current fiber

$$\beta = 0.0439445 \times 30 \times \frac{10^{-6}}{\sqrt{2 \times 0.010174}} = 9.242 \times 10^{-6}$$

$$\frac{1}{\beta} = 1.08 \times 10^5$$

Given that Bessel arguments are scaled with $1/\beta$, we can use asymptotic forms.

$$J_v(z) \sim \left(\frac{2}{\pi z}\right)^{1/2} \left[\cos\left(z - \frac{1}{2}\pi v - \frac{1}{4}\pi\right) \sum_{m=0}^{\infty} \frac{(-1)^m (v, 2m)}{(2m)^{2m}} - \sin\left(z - \frac{1}{2}\pi v - \frac{1}{4}\pi\right) \sum_{m=0}^{\infty} \frac{(-1)^m (v, 2m+1)}{(2z)^{2m+1}}\right] \quad (46)$$

$$Y_v(z) \sim \left(\frac{2}{\pi z}\right)^{1/2} \left[\sin\left(z - \frac{1}{2}\pi v - \frac{1}{4}\pi\right) \sum_{m=0}^{\infty} \frac{(-1)^m (v, 2m)}{(2m)^{2m}} + \cos\left(z - \frac{1}{2}\pi v - \frac{1}{4}\pi\right) \sum_{m=0}^{\infty} \frac{(-1)^m (v, 2m+1)}{(2z)^{2m+1}}\right] \quad (47)$$

where

$$(v, m) = \frac{\Gamma\left(v + m + \frac{1}{2}\right)}{m! \Gamma\left(v - m + \frac{1}{2}\right)} \quad (48)$$

Since we are dealing with J_0 and Y_0 so $v = 0$. In this case

$\sum_{m=0}^{\infty} \frac{(-1)^m (v, 2m)}{(2m)^{2m}}$ for $m = 0$ becomes 1 and for $m > 1$ is 0

$\sum_{m=0}^{\infty} \frac{(-1)^m (v, 2m+1)}{(2z)^{2m+1}}$ is 0 for all m as long as $v = 0$

So we use the following approximations

$$J_v(z) \sim \left(\frac{2}{\pi z}\right)^{1/2} \cos\left(z - \frac{1}{4}\pi\right) \quad (49)$$

$$Y_v(z) \sim \left(\frac{2}{\pi z}\right)^{1/2} \sin\left(z - \frac{1}{4}\pi\right) \quad (50)$$

And asymptotically we arrive to the following equation:

$$Q(\zeta) = \left(\frac{2}{\pi \zeta}\right)^{1/2} \left[A \cos\left(\zeta - \frac{1}{4}\pi\right) + B \sin\left(\zeta - \frac{1}{4}\pi\right)\right] \quad (51)$$

We can further simplify the above equations

$$Q(\zeta) = \left(\frac{2}{\pi \zeta}\right)^{1/2} \left[A \cos\left(\zeta - \frac{1}{4}\pi\right) + B \sin\left(\zeta - \frac{1}{4}\pi\right)\right]$$

$$Q(\zeta) = \left(\frac{2}{\pi \zeta}\right)^{1/2} \sqrt{A^2 + B^2} \left[\frac{A}{\sqrt{A^2 + B^2}} \cos\left(\zeta - \frac{1}{4}\pi\right) + \frac{B}{\sqrt{A^2 + B^2}} \sin\left(\zeta - \frac{1}{4}\pi\right)\right]$$

given

$$\cos(\alpha - \beta) = \cos(\alpha)\cos(\beta) + \sin(\alpha)\sin(\beta)$$

$$\cos(\beta) = \frac{A}{\sqrt{A^2 + B^2}}, \qquad \sin(\beta) = \frac{B}{\sqrt{A^2 + B^2}}, \qquad \tan(\beta) = \frac{B}{A}, \qquad \beta = \mathrm{atan}\left(\frac{B}{A}\right)$$

Which gives

$$Q(\zeta) = \frac{C_Q}{\sqrt{\zeta}}[\cos(\zeta - \phi)]$$

where $C_Q = \sqrt{\frac{2}{\pi}}\sqrt{A^2 + B^2}$, $\phi = \frac{\pi}{4} + \mathrm{atan}\left(\frac{B}{A}\right)$ and $\zeta = \frac{e^{\beta\xi}}{\beta}$

The following integral should be calculated

$$\int \frac{d\xi}{Q^2(\xi)}$$

since $d\xi = \frac{d\zeta}{\beta\zeta}$. So the integral we need to solve is

$$\int \frac{d\zeta}{Q^2(\zeta)} = \int \frac{\zeta\frac{d\zeta}{\beta\zeta}}{C_Q^2 \cos^2(\zeta - \phi)} =$$

$$\frac{1}{C_Q^2\beta}\int \frac{d\zeta}{\cos^2(\zeta - \phi)} = \frac{1}{C_Q^2\beta}\tan(\zeta - \phi) + const \qquad (52)$$

By replacing ζ with ξ we get

$$\int \frac{d\xi}{Q^2(\xi)} = \frac{1}{C_Q^2\beta}\tan\left(\frac{e^{\beta\xi}}{\beta} - \phi\right) + const \qquad (53)$$

We are now left with computing the coefficients from the initial conditions. We consider a special

case of $C_2 = 0$

$$C_1 w^2 = Q^2\left(1 + C_1^2 \left[\int_0^\xi \frac{d\xi}{Q^2(\xi)}\right]^2\right) \qquad (54)$$

$at\ z = 0\ (\xi = 0),\ w(0) = w_0$

$$C_1 w^2 = Q^2$$

$$Q(\xi) = AJ_0\left(\frac{e^{\beta\xi}}{\beta}\right) + BY_0\left(\frac{e^{\beta\xi}}{\beta}\right)$$

$$C_1 = \frac{\left[AJ_0\left(\frac{1}{\beta}\right)+BY_0\left(\frac{1}{\beta}\right)\right]^2}{w_0^2} \tag{55}$$

Our second assumption is that the incoming wave is incident on the fiber at its minimum waist $w' = 0$.

$$2C_1w\,w' = 2Q\,Q'\left(1 + C_1^2\left[\int_0^\xi \frac{d\xi}{Q^2(\xi)}\right]^2\right) + 2Q^2C_1^2\left[\int_0^\xi \frac{d\xi}{Q^2(\xi)}\right]\frac{1}{Q^2}$$

At $\xi = 0$ the $\int_0^\xi \frac{d\xi}{Q^2(\xi)} = 0$ so:

$$2C_1w\,w' = 2Q\,Q'$$

So

$$Q' = 0$$

$$\frac{dQ(\xi)}{d\xi} = e^{\beta\xi}\left[AJ_0'\left(\frac{e^{\beta\xi}}{\beta}\right) + BY_0'\left(\frac{e^{\beta\xi}}{\beta}\right)\right] \tag{56}$$

Evaluating the above expression at $\xi = 0$ gives

$$\frac{dQ(\xi)}{d\xi}\Big|_{\xi=0} = AJ_0'\left(\frac{1}{\beta}\right) + BY_0'\left(\frac{1}{\beta}\right) = 0 \tag{57}$$

We can always normalize the coefficients and consider $C_1 = 1$ then

$$Q(0) = w_0 \tag{58}$$

Which gives

$$AJ_0\left(\frac{1}{\beta}\right) + BY_0\left(\frac{1}{\beta}\right) = w_0 \tag{59}$$

$$AJ_0'\left(\frac{1}{\beta}\right) + BY_0'\left(\frac{1}{\beta}\right) = 0 \tag{60}$$

Given the above equations A and B are easily calculated as below:

$$A = \frac{w_0 Y_0'\left(\frac{1}{\beta}\right)}{J_0\left(\frac{1}{\beta}\right)Y_0'\left(\frac{1}{\beta}\right) - J_0'\left(\frac{1}{\beta}\right)Y_0\left(\frac{1}{\beta}\right)}$$ (61)

$$B = \frac{-w_0 J_0'\left(\frac{1}{\beta}\right)}{J_0\left(\frac{1}{\beta}\right)Y_0'\left(\frac{1}{\beta}\right) - J_0'\left(\frac{1}{\beta}\right)Y_0\left(\frac{1}{\beta}\right)}$$ (62)

According to Wronskian relation

$$J_\alpha(x)Y_\alpha'(x) - J'_\alpha(x)Y_\alpha(x) = \frac{2}{\pi x}$$ (63)

then in our case we simply have:

$$J_0\left(\frac{1}{\beta}\right) Y_0'\left(\frac{1}{\beta}\right) - J_0'\left(\frac{1}{\beta}\right) Y_0\left(\frac{1}{\beta}\right) = \frac{2\beta}{\pi}$$ (64)

finally, the coefficients are found as below

$$A = \frac{\pi w_0}{2\beta} Y_0'\left(\frac{1}{\beta}\right) = -\frac{\pi w_0}{2\beta} Y_1\left(\frac{1}{\beta}\right)$$ (65)

$$B = -\frac{\pi w_0}{2\beta} J_0'\left(\frac{1}{\beta}\right) = +\frac{\pi w_0}{2\beta} J_1\left(\frac{1}{\beta}\right)$$ (66)

As we saw By solving this Ermakov problem, one finds:

$$w^2 = w_0^2 \left[A J_0\left(\frac{e^{\beta\xi}}{\beta}\right) + B Y_0\left(\frac{e^{\beta\xi}}{\beta}\right) \right]^2 \left(1 + \frac{1}{C^4\beta^2}\left(\tan\left(\frac{e^{\beta\xi}}{\beta} - \phi\right) - \tan\left(\frac{1}{\beta} - \phi\right) \right)^2 \right)$$

In the above expression, w_0 is the input beam waist, $\xi = z\frac{\sqrt{2\Delta}}{a_0}$ represents a normalized propagation

distance, and the quantities β, C and ϕ are given by $\beta = \gamma a_0/2\sqrt{2\Delta}$, $C = \sqrt{\frac{2(A^2+B^2)}{\pi}}$, $\phi = \pi/4 +$

$\tan^{-1}(B/A)$, where the coefficients A and B in these relations are obtained from the input initial

conditions. In the case, the input beam is incident upon the fiber at its minimum waist, the

parameters A and B can be obtained from $= -\frac{\pi w_0}{2\beta x_0} Y_1\left(\frac{1}{\beta}\right)$, $B = \frac{\pi w_0}{2\beta x_0} J_1\left(\frac{1}{\beta}\right)$, where $x_0^2 = \frac{a_0}{\sqrt{2\Delta}\, k_0 n_0}$,

with x_0 being the spot-size of the fundamental mode. In addition, $J_1(x)$ and $Y_1(x)$ represent first-

order Bessel functions of the first and second kind, respectively. Figure 4-1 (b) depicts the spot-

size evolution $w(\xi)$ as a function of propagation distance. In this example, the input spot-size w_0 was chosen to be 1.5 times larger than that of the fundamental mode x_0. For illustration purposes, we considered a relatively short tapered parabolic-index MMF, where its core radius decreases from 40 to 10 μm within 4 cm.
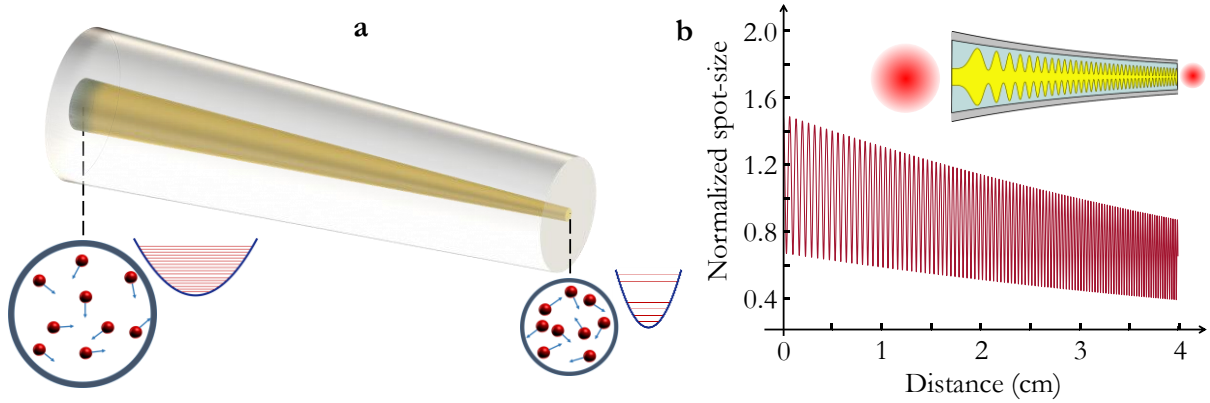
Figure 4-1 Acceleration of intermodal collisions in a tapered multimode fiber. (a) Schematic of a core-decreasing parabolic multimode fiber. As the fiber core is reduced in size, the spacing between the propagation eigenvalues increases, leading to an acceleration in intermodal collisions and energy exchange. (b) Evolution of the spot-size as a function of the propagation distance in a 4-cm tapered fiber when its core decreases from 40 to 10 μm. In this example, the input spot-size was chosen to be 1.5 times larger than that of the fundamental mode. As shown in (b), the oscillations in the optical beam diameter experience an acceleration along the propagation direction.

This figure clearly shows that as the fiber narrows down, the beam waist decreases while the intermodal beam oscillation rate experiences an acceleration along the propagation direction. In the presence of nonlinearity, this power density compression implies that the interaction forces among modes are also progressively accelerating and enhanced. As we will see, this acceleration of intermodal oscillations can alter the soliton fission process and drastically change the behavior of the generated DWs and Raman-shifted solitons as well as the soliton modal content.

To experimentally study this tapered MMF system under anomalously dispersive conditions, we use 100 fs pulses (up to 170 nJ in energy) at 1550 nm from a mode-locked Ti:Sapphire laser. In

these experiments, the input beam waist is 15 μm, thus exciting tens of modes. The parabolic fiber

under consideration is comprised of two sections: a 10 m uniform section having a core radius of

40 μm followed by a 4-m tapered segment where the core radius exponentially decreases from 40

to 10 μm.
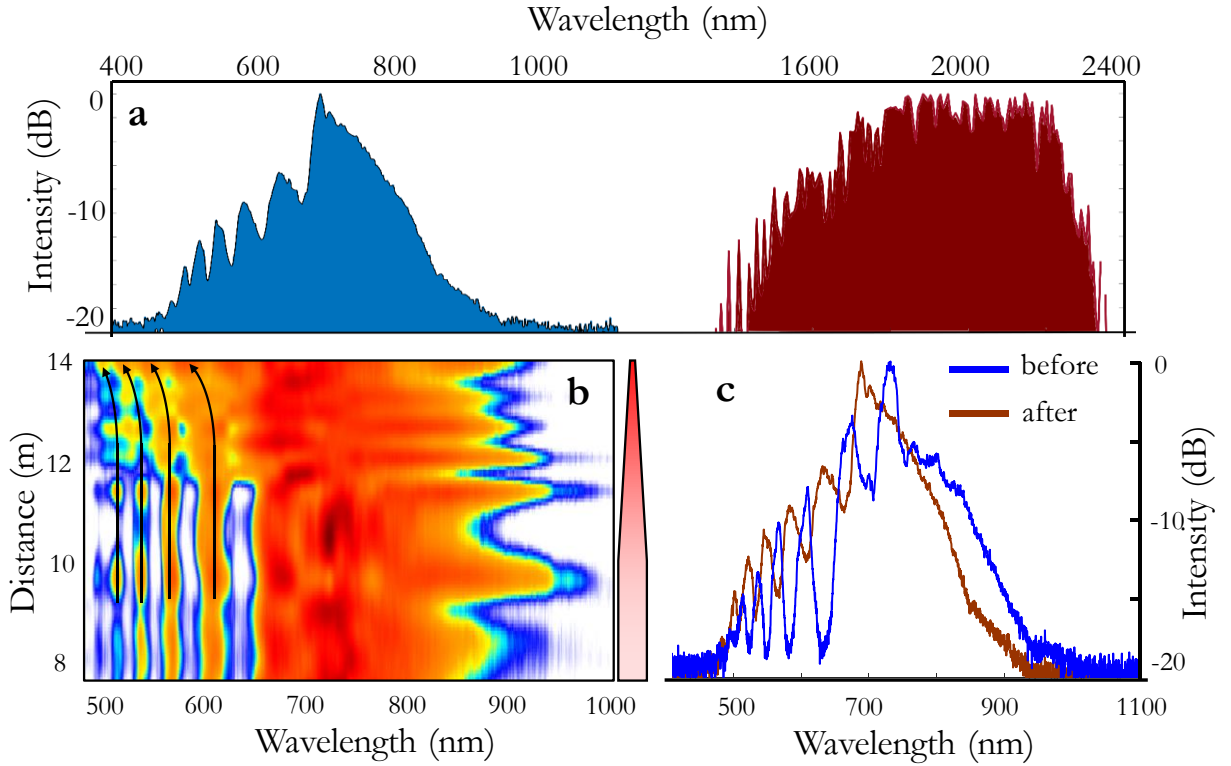
Figure 4-2 Experimentally observed spectral evolution in a tapered multimode fiber (a) The spectrum recorded at the output of the tapered multimode fiber when a 100 fs, 1550 nm pulse is used at the input with a peak power of 750 kW. The NIR frequency components are formed because of multimode solitons while the visible part arises from dispersive waves. (b) Spectral evolution in the visible section as measured using a cutback method. The tapered segment of the MMF is 4 m long (its core radius is reduced from 40 to 10 μm) and is preceded by a 10 m uniform fiber. As the pulses enter the tapered section, DWs experience a continuous blue-drifting of more than 45 nm, indicating a speedup in the intermodal oscillations. (c), The spectrum in (b) is depicted for comparison, before and after the tapered section where blue-shifting of the DW-comb is evident.

By employing cutback methods, this particular arrangement allows one to monitor and compare

the generated nonlinear interactions and spectra in these two different environments. The entire

spectrum (750 kW) obtained after the taper is shown in Figure 4-2 (a). The experimentally

observed visible side of the spectrum (produced by DWs) is plotted in Figure 4-2 (b). This figure

shows, that, in the uniform section, the spectrum finally evolves into a broadband DW comb-like

structure, characterized by a series of distinct lines, formed at the soliton fission point.
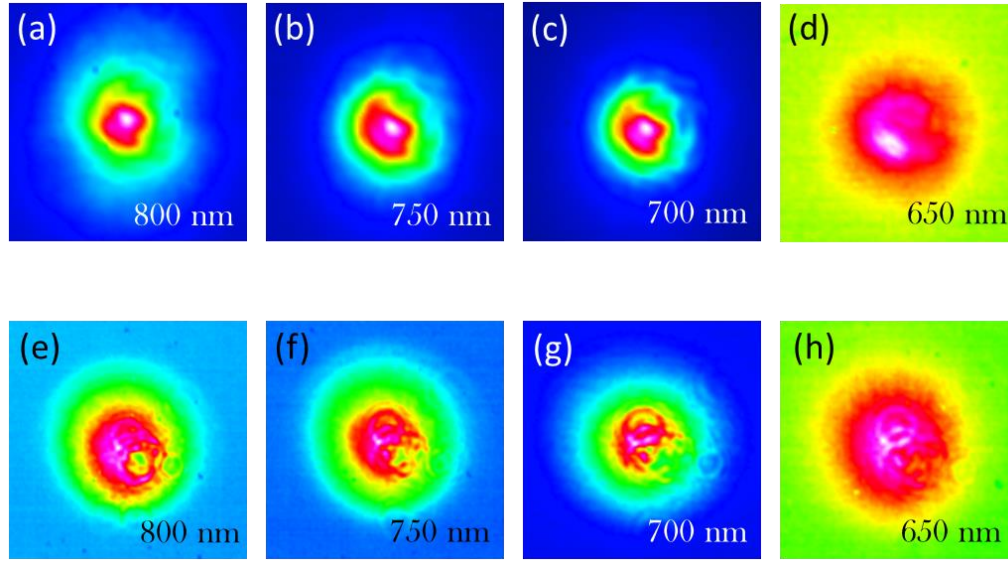
Figure 4-3 The beam profiles corresponding to DWs before and after the tapered section. (a-d), the beam profiles at four wavelengths 800, 750, 700 and 650 nm before the tapered section and after 10 m of propagation through the uniform fiber. The beam profiles are clean with most of the energy in the fundamental mode. (e-h), the beam profiles after the tapering section at the same four wavelengths. The dispersive waves that are generated as a result of an acceleration of solitons are still clean, mostly residing in the fundamental mode

Emission of such broadband DWs in graded-index MMFs have been observed and reported in a

number of studies before [25,28,80]. Unlike in single mode fibers where the soliton fission process

is accompanied by the generation of a phase-matched narrowband DW line [22,81], in graded-

index MMFs, the resulting DWs are broadband and comb-like, a behavior attributed to the periodic

compression/expansion of propagating MM-solitons in graded-index MMFs. As clearly shown in

Figure 4-2 (b), the spectrum remains almost invariant as long as the MMF is axially uniform. On

the other hand, in the last 4-m tapered stage, as the solitons experience a speedup in their

intermodal oscillations, a significant accelerated drift of the DW-combs (black arrows) towards shorter wavelengths is observed. Figure 4-2 (c) compares the output spectra, before and after the tapering section where a blue-drifting of more than 45 nm is observed.
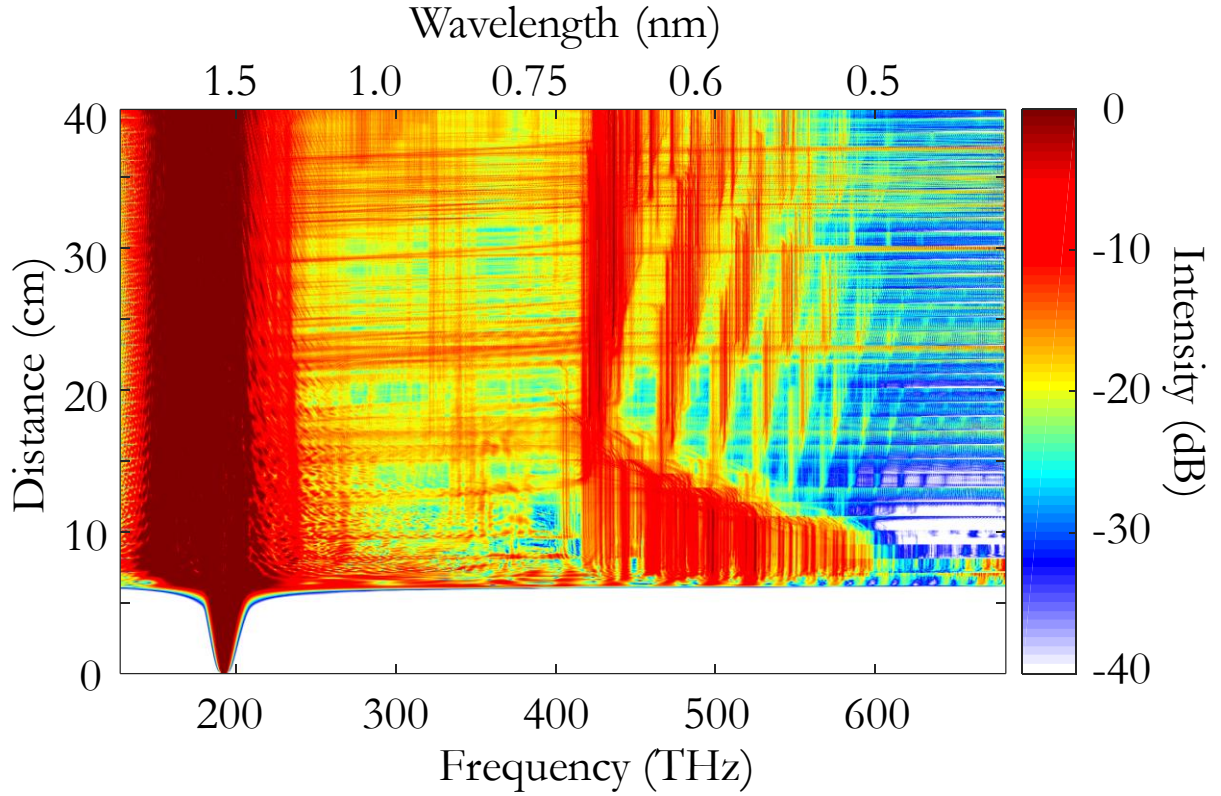
Figure 4-4 Spectral evolution in a tapered multimode fiber as obtained from a gUPPE simulation. A 400-fs, 1550 nm pulse with a peak power of ~ 500 kW is injected in a 40 cm long tapered multimode fiber, whose core radius decreases from 40 to 10 µm. After only a few centimeters of propagation, the input pulse undergoes a soliton fission and a sequence of DWs emerges in the visible. Upon further propagation, the generated MM-solitons experience fission-like processes (red horizontal lines) that almost immediately expand the spectrum and generate new blue-drifted DW lines.

The spatial intensity profiles corresponding to the aforementioned combs, before and after the taper section, for four different wavelengths are depicted Figure 4-3 (e-h). The beam profiles before the tapering section are clean and Gaussian-like. This can be a result of the spatial beam

self-cleaning happening in MMFs. The beam distribution of the DWs stays clean and mostly confined in the fundamental mode even after it goes through an acceleration of oscillations.

To better understand this DW behavior, we conduct a series of numerical studies and simulations that implicitly take into account modal walk-offs, SPM, cross-phase modulation, four-wave mixing (FWM), Raman and shock effects, etc. Because of the computational complexity of this problem, we model these processes in much shorter taper spans by utilizing gUPPE methods [45,82]. The spectrum, as obtained from these simulations, is depicted in Figure 4-4. This figure demonstrates that as the soliton breaks up into its multimode soliton constituents, a series of Cherenkov lines (from 500 to 710 nm) is formed as a result of a broadband FWM phase-matching between these multimode solitons and DWs. As the core radius decreases along the fiber, the solitons tend to adjust to local fiber conditions, thus producing minor fission-like processes that lead to new DW spectral lines. The newly produced DWs are blue-drifted because of faster intermodal oscillations of multimode solitons. A cascade of these effects along the fiber taper leads to a continuous blue-shifting of the emerging DW-combs. It is worth noting that blue-drifting of DWs has been previously reported in the context of single-mode fibers. This observation has been explained through a trapping of DWs behind the decelerating solitons where the DWs have to shift their central wavelength in order to adjust for their now slower propagation velocities [83]. However, this is not the case in our study since the generated DWs are now lying well within the visible portion of the spectrum (500-650 nm) where the group velocities are much slower than that of MM-solitons and hence they cannot be trapped.

We next investigate the impact of these accelerating oscillations on multimode optical solitons. The theoretically anticipated temporal evolution of the input pulse, corresponding to Figure 4-4, is depicted in Figure 4-5. In this case, after the soliton fission point, the pulse disintegrates into a

number of multiple solitons. Interestingly, as the core radius decreases, the generated solitons behave very differently with respect to each other. After a brief period of deceleration, the first emitted soliton starts to eventually accelerate – an indication of soliton blue-shifting. The second soliton travels at a constant velocity and the subsequent solitons experience deceleration.
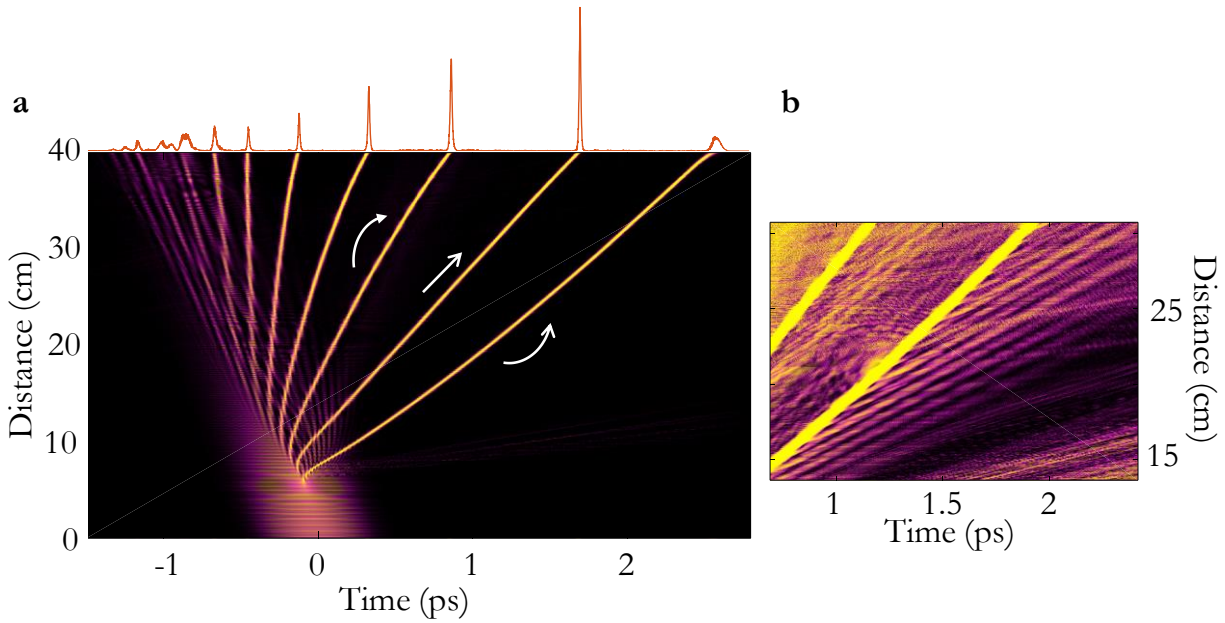
Figure 4-5 Temporal evolution of a 400-fs at 1550 nm pulse in a tapered multimode fiber as obtained from a gUPPE simulation. (a) Generation and propagation of MM-solitons are displayed in a co-moving temporal window. The parameters used are identical to those in Figure 4-4. The MM-solitons exhibit radically different behaviors as they propagate through the tapered section. The trajectory of the slowest soliton has a positive curvature, signifying a speedup during propagation. The second soliton has a zero temporal curvature (and thus no acceleration) while all the subsequent solitons are decelerating. (b) A closer look at the trajectory of the first emitted soliton reveals an emission of DWs as these solitons are continuously perturbed in the tapering section. Because of these DWs, the first soliton experiences a slight bend toward earlier times and hence travels faster.

This behavior is unexpected since the Raman induced self-frequency shift (SSFS) tends to slow down solitons by redshifting their central wavelengths [84]. As previously mentioned, MM-solitons are periodically perturbed in an accelerated fashion (via expansions/compressions) and hence continuously shed Cherenkov DWs as they go through the tapered fiber section. Since these

DWs have slower group velocities, they lag behind the generated MM-solitons – thus forcing them to interact with all the other solitons previously generated. In recent theoretical studies, it has been conjectured that this XPM interplay between DWs and solitons can lead to a cancelation of SSFS and hence blue-shifting of the ensued solitons [85,86]. Figure 4-5 (b) reveals as the first soliton sheds its DWs, it experiences a slight drift toward shorter delay times.
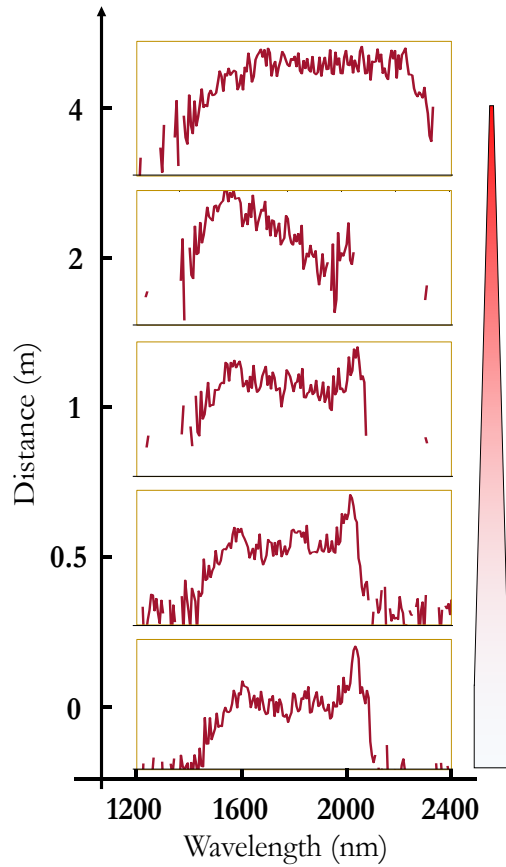
Figure 4-6 Experimentally observed spectra associated with MM-solitons along the tapered MMF. The NIR spectrum measured along the taper (right) when excited at 1550 nm. The parameters used are the same as those in Figure 4-2. In the lowest panel, recorded right before the start of the tapered section, the MM-soliton spectrum resides in the long wavelength edge – around 2000 nm. However, after 0.5 m of propagation, the energy is transferred towards shorter wavelengths. After 2 m of propagation, most of the energy is found to be below 1600 nm. Finally, at the end of the taper, the soliton energy is uniformly distributed over a wide spectral window extending from 1500 to 2300 nm. The height of each panel is scaled at 20 dB.

This indicates a temporal acceleration of this soliton which is also accompanied by a blue-shifting in the spectral domain. Another interesting aspect associated with this process is a monotonic growth in the average energy residing in the second soliton during propagation. This is in agreement with recent predictions, suggesting that under appropriate conditions a soliton can also absorb energy from DWs and hence grow in intensity [85]. Experimental observations corroborate this behavior. In this respect, Figure 4-6 shows the evolution of the experimentally observed spectrum in the NIR, for five different distances along the MMF taper. While before the tapering section, a significant amount of the total soliton energy happens to reside in the longer wavelength edge (2000 nm) as a result of intrapulse Raman scattering, after 2 m in the taper, the spectrum shifts towards shorter wavelengths. This represents the first experimental observation of intrapulse Raman scattering cancelation and soliton blue-shifting through a DW interaction – as theoretically predicted in Refs. [85,86]. Figure 4-6 shows that, finally, after 3 m of propagation, the spectral energy is uniformly distributed across the NIR window.
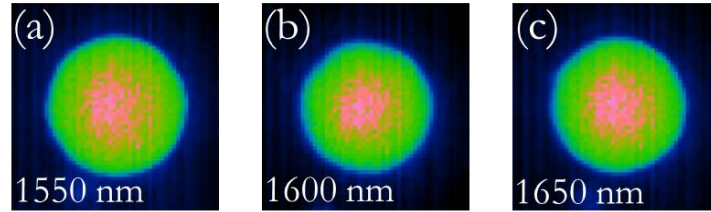
Figure 4-7 The beam profile of the Raman-shifted solitons at three sample wavelengths. All the beam profiles are captured right before the tapered section. In all cases, the beam distributions are Gaussian-like, clean and stable.

As previously reported in several studies, one expects considerable beam self-cleaning in MMFs because of FWM. The spatial beam profile associated with the DW wavelengths, before and after the taper, is relatively speckle-free and Gaussian-like, with most of its energy residing in the fundamental mode (see Figure 4-7). However, this is not the case for multimode solitons

occupying the spectral regions between 1.55 – 2 µm. The spatial beam profiles corresponding to the various MM-solitons was measured at different positions along the MMF taper. While, the soliton beam profiles happen to be quasi-Gaussian in the uniform fiber section, as the solitons enter the tapered section, their modal distribution becomes destabilized and the energy flows towards higher-order modes. Figure 4-8 depicts this effect at different positions within the taper.
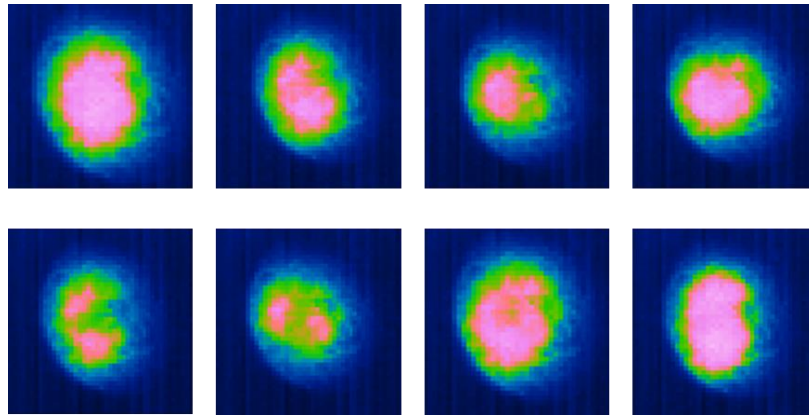
Figure 4-8 The beam profiles of the Raman-shifted solitons measured after the tapering section. These beam profiles are measured at a sample distance of 2 m after the onset of the tapered section. The beam profiles are recorded at 1600 nm for 8 different instants. The beam is very unstable and the energy continuously jumps among different modes. A ring pattern and the beam profile mode of LP_{11} are evident in this figure.
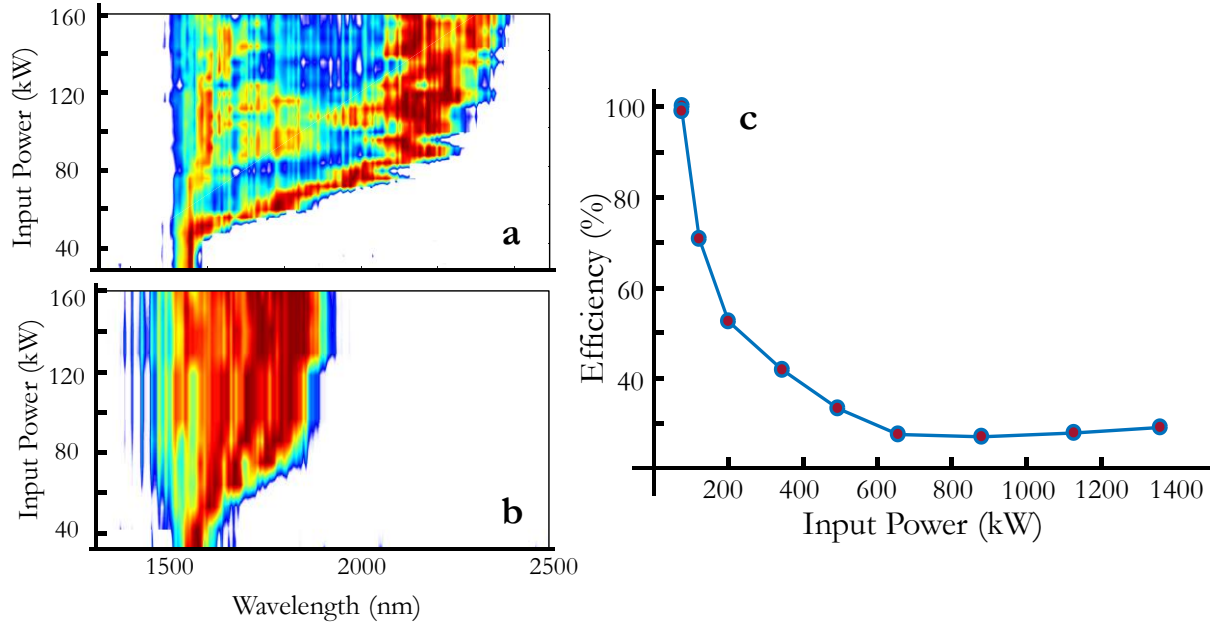
Figure 4-9 An experimental comparison of soliton red-shifting in a tapered and a uniform MMF. (a) The output spectrum after a 3-m tapered MMF with a core radius decreasing from 30 to 10 µm. As the input power level increases, the soliton experiences a significant redshifting that extends up to 2300 nm. (b) The recorded output spectrum from a 3-m uniform graded-index MMF having a core radius of 25 µm. In this regime, the solitons experience a subdued red-shifting up to 1900 nm. (c) The transmission efficiency curve as obtained by comparing the fiber output power before and after the tapered segment. As the input power level increases, the efficiency drops. In all cases, 100-fs pulses at 1550 nm are used.

The power loss associated with this tapered MMF is measured as a function of the input power and is depicted in Figure 4-9 (c). To estimate the power transmission, the total energy is measured before and after the tapering section. Figure 4-9 (c) indicates that at relatively low input powers (<70 kW) the transmission through the taper is almost 100%. This high transmission is here attributed to the beam self-cleaning effect that promotes propagation in the lower-order modes. However, as the input power is increased to 640 kW, the efficiency significantly drops to ~30%, eventually stabilizing around this value. To understand this behavior, we compared the NIR spectral response of a uniform 3-m long MMF (25 µm core radius) with that of a tapered fiber (3 m in length, and a core radius decreasing from 30 to 10 µm) as a function of input peak power. These results, depicted in Figure 4-9 (a) and (b), interestingly show, that in the tapered case, there

is an enhancement in the soliton self-frequency shift, as the input power levels increase. This, in turn, pushes the generated soliton wavelengths into the long-wavelength edge (above 2 µm) where the fiber linear loss happens to be significantly larger. Therefore, the overall loss in the system is expected to increase at higher power levels.

4.4 Spatiotemporal Dynamics in Normally Dispersive MMF Tapers.

For this set of experiments, we used in-house fabricated germanium-doped graded-index silica MMFs having different lengths and tapering ratios. In all cases, the fiber index profile remains self-similarly parabolic along the entire length, having a maximum numerical aperture of NA= 0.21. The fibers were excited with a microchip laser pump at 1064 nm where silica is normally dispersive. This laser delivers 400 ps pulses with a maximum energy of 95 µJ (maximum peak power of 240 kW) at a 500 Hz repetition rate. Laser radiation is coupled into the fibers through a 50 mm focal length lens. The input beam is centered at the fiber front facet, exciting hundreds of modes. Figure 4-10 (a) shows the resulting supercontinuum spectrum as obtained at the output of a 15-m long MMF taper when its core radius decreases exponentially from 40 to 10 µm.
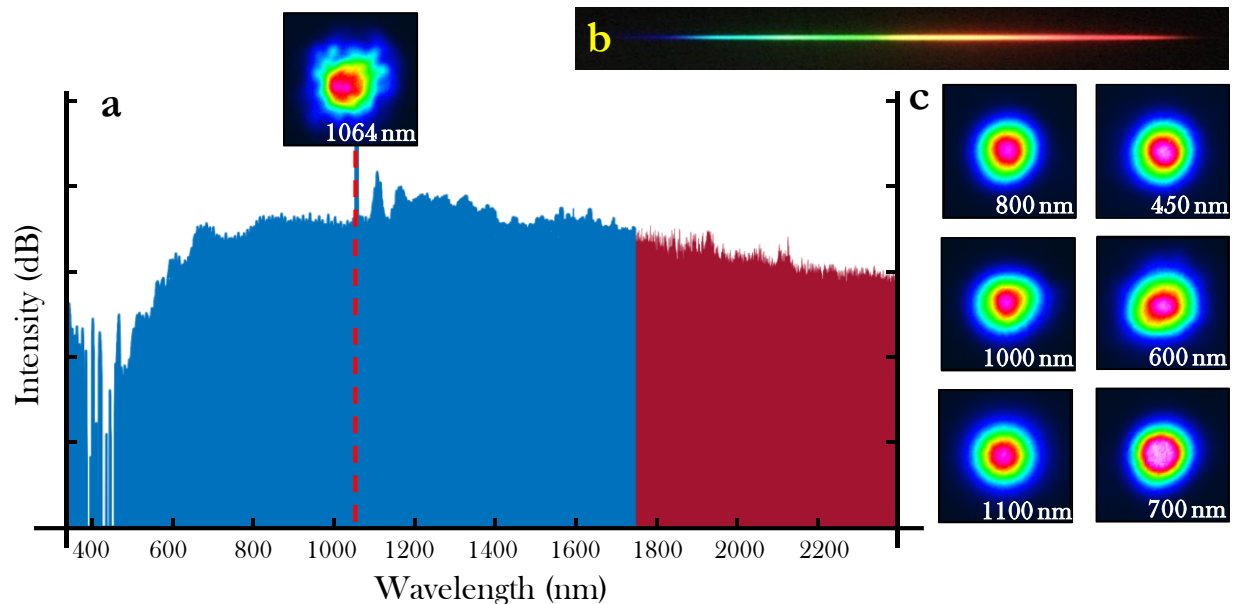
Figure 4-10 Experimentally obtained supercontinuum spectra from a tapered parabolic-index MMF. (a) The output supercontinuum spectrum after a 15-m long graded-index MMF when its core radius is reduced from 40 to 10 µm. The fiber is excited at 1064 nm (red dashed line) in the normal dispersion regime with an input pulse of 400 ps and a peak power of 180 kW. The spectrum happens to be relatively flat, extending from 450 to 2400 nm (more than 2.5 octaves). The pump beam profile is shown as an inset in (a). (b) A photograph image of the visible component of the dispersed output spectrum. (c) The beam profiles recorded at different wavelengths of the output supercontinuum. All the beam profiles appear clean and speckle-free, with a significant amount of power residing in the fundamental mode. Every scale division in (a) corresponds to 10 dB.

At the pump wavelength, the taper initially supports ~ 600 modes while at the end of the fiber this number is reduced to ~ 40. Our experimental results indicate an exceptionally flat and uniform supercontinuum (SC) spectrum, spanning more than 2.5 octaves (from 450 nm to 2400 nm), with a relative variation of less than 10 dB across the entire bandwidth. Such a flat, far-extended spectrum has never been observed before in any other single-mode or multimode fiber setting. The beam profiles corresponding to different SC wavelengths are also shown in Figure 4-10. In all cases, the experimentally observed beam patterns are quasi-Gaussian and speckle-free. These results suggest that most of the energy at these wavelengths is funneled towards lower order modes.
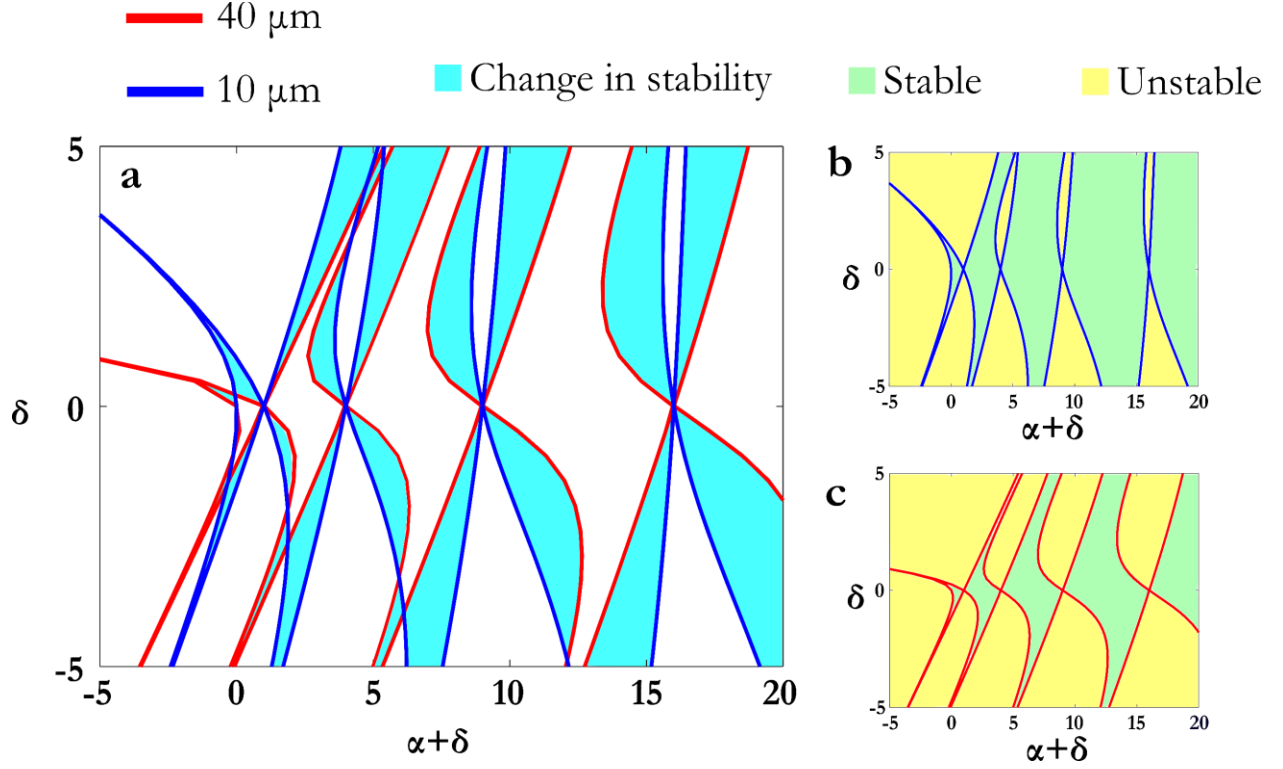
Figure 4-11 Theoretical stability diagram for a locally uniform MMF. (a) Change in the stability diagram when the fiber radius is reduced from 40 to 10 µm. A reduction in the radius of the MMF shifts the unstable gain regions, thus leading to new spectral lines. (b) and (c), Stability diagrams corresponding to parabolic MMFs with core radii of 40 and 10 µm, respectively. In all cases, the input spot-size was chosen to be 1.5 times that of the fundamental mode and the input peak power was assumed to be 180 kW. The parameters α and β are defined as $= \frac{a^2}{2\Delta}\beta_e^2$, $\delta = \frac{a^2}{2\Delta}\beta_e k_0 n_2 E_0^2 \omega_i^2$.

In order to unravel the origin of this flat supercontinuum generation, it is imperative to first understand how FWM processes or geometric parametric instabilities [29,43] unfold in a uniform graded-index nonlinear MMF. This analysis is pertinent to CW (or in our case broad pulses) excitations in the normal dispersive region. As is well-known, if the input beam is Gaussian, then the CW component undergoes periodic compressions/expansions – resulting from the self-imaging property of parabolic MMFs. This, in turn, has a profound effect on the spectral perturbations $A(z, \Omega)$, located at the sidebands $\omega_0 \pm \Omega$ around the carrier frequency ω_0. Under these conditions, these perturbations obey the following Hill's equation:

$$\frac{d^2 A}{d\xi^2} + \frac{a_0^2}{2\Delta} [\beta_e^2 + (\beta_e k_0 n_2 E_0^2 w_0^2) f(\xi)] A = 0 \qquad (67.)$$

where $\beta_e = (\beta(\omega_0 + \Omega) + \beta(\omega_0 - \Omega))/2 - \beta(\omega_0)$ involves all the even terms of the Taylor series expansion of the dispersion profile $\beta(\omega)$. In the above equation, $\xi = \sqrt{2\Delta} \, (z/a_0)$ represents a normalized propagation distance, n_2 accounts for the Kerr nonlinear index coefficient, and $k_0 = 2\pi/\lambda_0$, with λ_0 being the pump wavelength. The parameters E_0 and w_0 are fully determined from the initial conditions with the former denoting the initial electric field amplitude and the latter representing the input beam spot-size. The function $f(z) = 1/w^2 (z)$ corresponds to the beating behavior of light during propagation, where $w(z)$ denotes the local beam spot-size. The associated stability diagram (Figure 4-11 (a)) and the corresponding gain regions can then be obtained using Floquet theory.

Starting from noise, any frequency component lying in the unstable regions experiences an amplification, leading to a flow of energy from the pump to a particular set of spectral lines. Interestingly, this instability occurs even in the normal dispersion region. The gain experienced by the spectral lines depends on a number of factors including the depth of the nonlinear modulation. Figure 4-11 (b) and (c) depict the stability diagrams corresponding to the entrance and exit regions of a tapered MMF. The parameters used to obtain these diagrams are identical to those involved in our experiment at a peak power level of 180 kW. As it is evident from Figure 4-11, as the core radius decreases from 40 to 10 µm, the unstable (gain) frequency regions start to drift in a substantial way, thus sweeping the entire spectrum. This explains the flat supercontinuum generation observed in our experiment. In essence, this accelerated drift of the unstable regions allows the FWM to equally populate the SC.
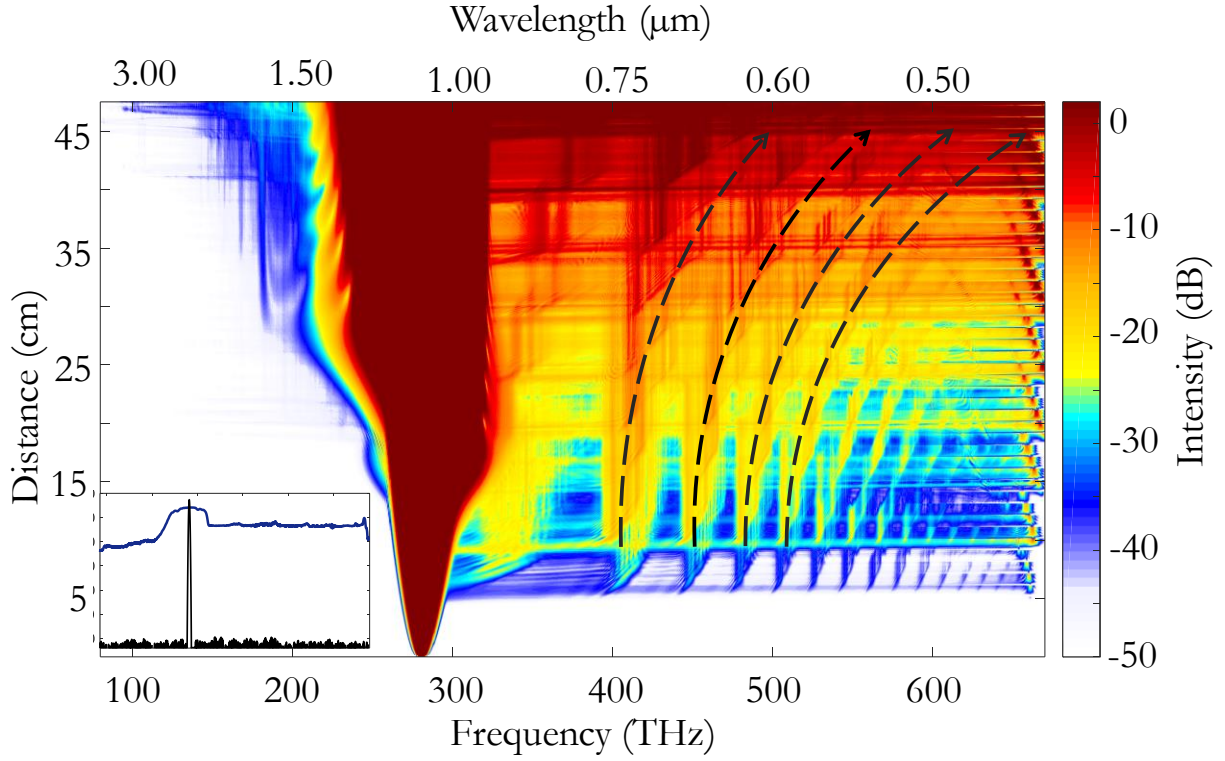
Figure 4-12 A gUPPE simulation of the spectral evolution in a tapered MMF when excited in the normal dispersion regime. A 0.5 m long MMF taper is excited with a 300 kW, 400 fs pulse, at 1064 nm. After only a few centimeters of propagation (~ 5 cm), a series of sidebands emerge. As the input pulse traverses the tapering section, an acceleration of intermodal collisions occurs. As a result, the newly generated sidebands drift away from the pump (dotted arrows), thus sweeping the entire spectrum. This leads to a flat and uniform SC. The inset compares the spectrum of the input pulse (black) with the output SC (blue).

To simulate these effects, we use gUPPE methods. The parameters employed in our simulations correspond to those in our experiment, only this time the length of the taper is assumed to be 0.5 m (to reduce computational complexity). The evolution of the spectrum during propagation is depicted in Figure 4-12. After a few centimeters of propagation, a series of sidebands emerge – as expected from geometric parametric instability. For longer propagation distances, where the beam oscillations speed up, all the generated sidebands start to drift away from the pump in an accelerated fashion (dotted arrows in Figure 4-12). These accelerated sidebands subsequently merge and form a uniform spectrum. The inset in Figure 4-12 shows the spectrum at the input and

the output of the fiber, as obtained from gUPPE. In addition, as the spectrum extends into the anomalous dispersion regime, formation of solitons is imminent. This process leads to a relatively uniform spectrum in the NIR – as it was previously shown in Figure 4-10. This can explain the extent of the spectrum in the NIR (Figure 4-10). Note, that this sideband generation occurs despite the fact that the modal oscillations are no longer periodic. Nevertheless, this instability can only be encouraged as long as the tapering takes place in an adiabatic manner – thus allowing the sidebands to efficiently grow. Adiabaticity of the tapered fiber has an impact on the spectral evolution.

As it was mentioned before, the periodic compression/expansion of a propagating beam in a parabolic-index multimode fiber leads to a sideband generation process. The efficiency of this process depends upon many factors including the perfect periodic oscillations. As the oscillation deviates from perfect periodicity, efficiency drops as a result. In tapered MMFs, the tapering rate determines the efficiency of the process. In Figure 4-13, a 1-m long tapered fiber with a core radius changing rapidly from 25 to 10 µm has been illuminated with different power levels of the input beam. In all cases, the sideband generation is suppressed due to a fast tapering rate. Figure 4-14 and Figure 4-15 show the output spectra of two fiber tapers of 3 and 5 m. These results show that as the tapering rate gets smaller and the taper length increases, the output spectrum becomes richer in spectral content and also more uniform. In addition, to push the short wavelength edge of the spectrum towards the blue and UV wavelengths, one needs to use a tapered fiber with smaller terminal radius.
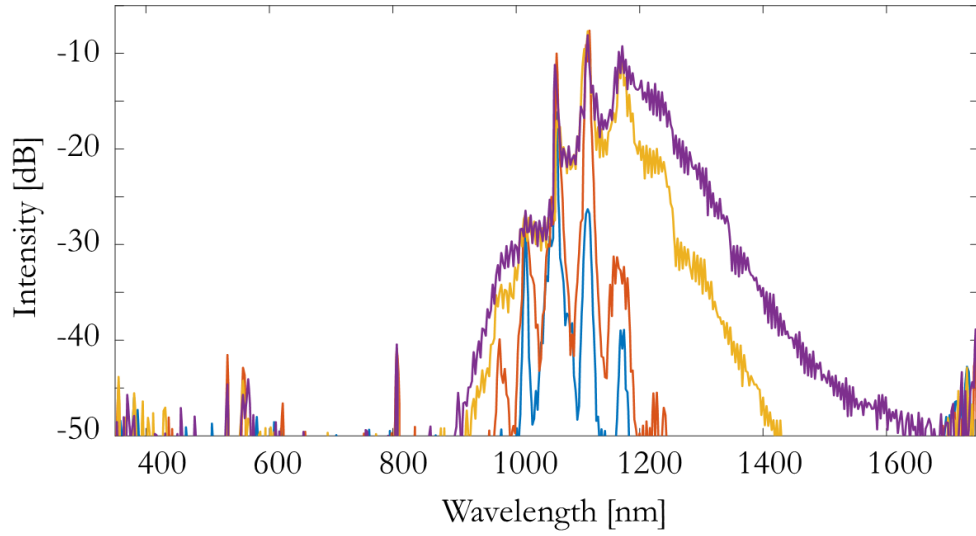
Figure 4-13 The output spectrum for a 1-m MMF taper. The spectra are measured at the end of a 1-m tapered MMF with the core radius changing from 25 to 10 µm. The power has raised from tens of kW to 180 kW, however, there is no sign of any sideband generation process.
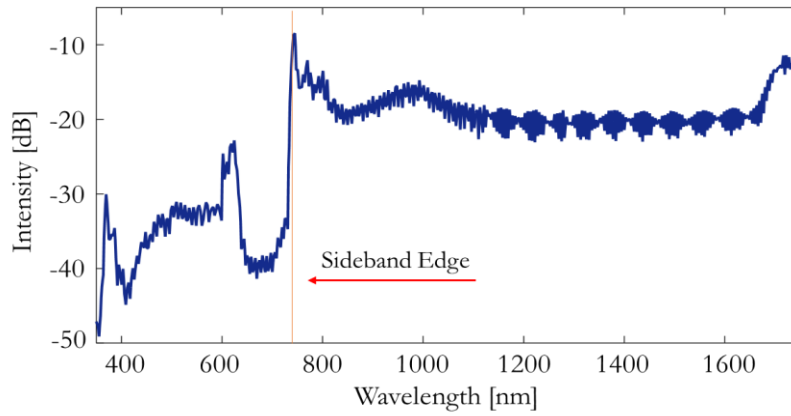
Figure 4-14 The output spectrum for a 3-m fiber taper. The spectrum is measured at the output of a 3-m long MMF taper with a core radius changing from 40 to 20 µm. The sideband generation process has pushed the spectrum edge down to 750 nm.
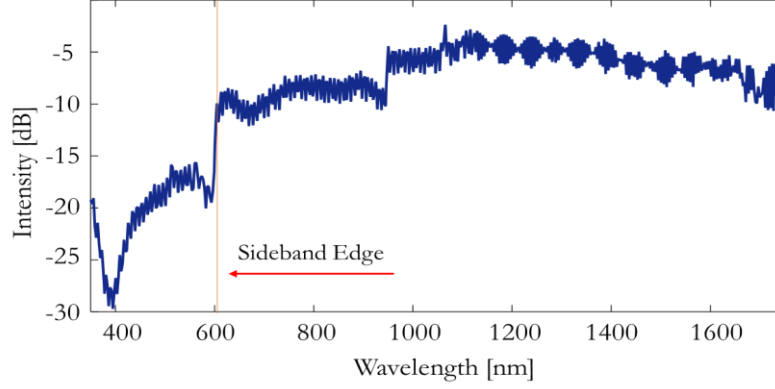
Figure 4-15 The output spectrum for a 5-m fiber taper. The spectrum is measured at the output of a 5-m long MMF taper with a core radius changing from 40 to 10 µm. The sideband generation has pushed the spectrum edge to 600 nm and has filled the gap between 600 and 750 nm (Figure 4-14)

In conclusion, we have investigated for the first time, accelerated nonlinear intermodal interactions in core decreasing multimode fibers. We have demonstrated that this spatiotemporal acceleration can have a significant effect on the temporal and spectral behavior in both dispersion regimes. In the anomalously dispersive region, this acceleration leads to blue-drifting dispersive wave combs while under normal dispersive conditions, we observe a generation of accelerating frequency bands that dynamically and uniformly sweep the entire spectrum. This, in turn, can be utilized to produce a notably flat and uniform supercontinuum, extending over 2.5 octaves. Our results could pave the way towards a new class of optical sources based on the aforementioned nonlinear acceleration dynamics.

4.5 Discussion

Historically, the field of nonlinear fiber optics has revolved mainly around single-mode optical fibers. Taking a fresh look at multimode fibers could provide new opportunities at both the scientific and technological levels. The additional spatial degrees of freedom offered by MMFs can indeed lead to a host of new phenomena. These include, for example, the emergence of

geometric parametric instabilities, MM-soliton formation, and beam self-cleaning. As indicated in our study, judiciously designed tapered multimode fibers can lead to accelerated nonlinear interactions, capable of generating new spectral lines, anywhere between the deep blue and IR wavelengths. In this respect, a gradual acceleration of these intermodal oscillations can be employed to induce an ultrabroad and uniform supercontinuum. In principle, because of larger core sizes, the SC produced in MMFs can have orders of magnitude higher spectral densities – as required in many applications. This same scheme can be used in fibers based on other material systems, such as chalcogenides that are considerably more transparent in IR. In the anomalous dispersive region, DW generation from accelerated soliton oscillations can lead to a significant blue-shift. This mechanism could be exploited in hollow-core photonic crystal fiber structures having minimal loss in the blue and near UV regions.

Another fundamental aspect considered in our study is associated with the complex dynamics of multimode spatiotemporal solitons in multimode fiber tapers. Interestingly, the nonlinear interaction between multimode solitons and slow propagating dispersive waves can mitigate or reverse the Raman-induced soliton self-frequency shift and the subsequent deceleration of solitons. In this same tapered environments, the spatially clean multimode solitons were found to destabilize, thus promoting energy transfer to higher-order modes. These observations indicate that multimode solitons are inherently complex entities requiring with potentially useful characteristics.

4.6 Methods

Simulations. The simulations were conducted using generalized unidirectional pulse propagation equations (gUPPE). The primary fiber parameters used in the simulations were the same (except for the length) as the tapered parabolic-index MMFs used in our experiments. In this respect, the

relative index change was assumed to be $\Delta \approx 1.6 \times 10^{-3}$ and the silica Kerr coefficient was taken to be $n_2 = 2.9 \times 10^{-20} \ m^2 W^{-1}$. In all cases, the core radius was reduced from 40 to 10 µm, as in the experiments. In addition, all nonlinear and linear processes such as modal walk-offs, self-focusing, self-phase modulation, cross-phase modulation, FWM, Raman and shock effects were accounted for in the simulations. The input pulse in the anomalous regime was centered around 1550 nm (0.193 PHz) and had a peak power of 500 kW. On the other hand, in the case of normal dispersion, the pulses were centered around 1064 nm (0.282 PHz), having a peak power of ~ 300 kW. In all our simulation, the pulse-widths (Figure 4-4, Figure 4-5 and Figure 4-12) were assumed to be 400 fs. The longitudinal step size was set at $\Delta z \approx 1 \ \mu m$. For undertaking such computationally demanding simulations, we used parallel computing, provided by the XSEDE supercomputer facility.

Experiments. The tapers used in both experiments utilized in-house fabricated germanium-doped graded-index silica multimode optical fibers having a range of fiber lengths and tapering ratios. The pulses were coupled to the fiber with up to 140 nJ (1.4 MW peak power) from a Ti:Sapphire laser source (1.55 µm) and with up to 72 µJ (180 kW peak power) form a microchip laser pump (1.064 µm). A three-axis translation stage and a 5 cm focal length lens were used to couple laser beams into the fibers. In all cases, the fibers had a NA=0.21. The ensued spectrum was measured with visible and IR spectrometers. Beam profiles at the output of the fibers were captured using visible and IR cameras. Several spectral filters were used to obtain the spatial distribution of the output beams at different wavelengths. For the cutback experiment, all measurements were recorded under the same initial conditions.

CHAPTER 5: GENERATION OF SELF-SIMILARITONS AND PARABOLIC PULSES IN PASSIVE GRADED-INDEX MULTIMODE FIBERS

Fiber lasers emerged as a rival to the well-established solid-state lasers. This platform offers some unique advantages that are very much desired in any practical laser systems. These include, for example, economic cost, high beam quality, compact design and good thermal management. However, utilizing small-core cross-section single-mode fibers for this purpose introduces new limitations. One such effect is accumulated nonlinear phase that reduces the pulse quality and compressibility [87–90]. Among the methods used to mitigate the nonlinear effects in fiber lasers, one popular approach is exploiting the unique properties of parabolic pulses. In the presence of a gain term, nonlinearity, and normal dispersion, there is an asymptotic solution with a temporal parabolic shape to the governing nonlinear Schrödinger equations. Such parabolic pulse solutions were first experimentally observed by Fermann et al [31,32,34]. Along these lines, the tolerances of these pulses to perturbations were also studied [91,92]. Due to their scalability and robustness to wave-breaking, these pulses were soon considered as candidates for making fiber amplifiers. The other unique feature of these attractor solutions that makes them ideal candidates for generating high energy short pulses is their linear chirp. The accumulated phase is turned into a linear chirp that can be easily compensated by a pair of gratings.

Performance of parabolic pulses is limited by gain bandwidth, higher-order dispersions, shock effect and stimulated Raman scattering. Among these factors, gain bandwidth sets the strictest limits. The bandwidth of a parabolic pulse cannot exceed the bandwidth of the gain medium and as the bandwidth of the parabolic pulse gets close to the gain bandwidth the linearity of the chirp is distorted and hence the pulse quality drops. The other major limitation comes from the fact that the amount of chirp a parabolic pulse can accumulate in a laser cavity is fully determined from the

74

cavity parameters and typically this value is not large enough. Accessing large chirp values significantly broadens the pulse and thus gives way to higher amplification levels.

One way to get around this problem is using tapered multimode optical fibers. The optical field inside a tapered MMF experiences an enhancement as a result of core-decreasing. Since, the energy confined to the spatiotemporal pulse is conserved, as the beam contracts in space the pulse intensity experiences an amplification. This artificial gain can lead to the formation of a parabolic pulse as it will be shown in the next section. The parabolic pulse generated through this process does not have any bandwidth limitation and the amount of chirp it accumulates is huge compared to that observed in single-mode fibers.

5.1 Parabolic Pulse Formation: Analysis

In the presence of a core-decreasing fiber, the nonlinearity monotonically increases – as a result of a reduction in the fiber core area. Assuming an exponential increase in the nonlinearity coefficient the governing nonlinear Schrödinger equation can be represented as below:

$$iU_z - \frac{\beta_2}{2} U_{TT} + \gamma |U|^2 e^{gz} U = 0 \tag{68}$$

By applying the change of variable $U = e^{-\frac{g}{2}z}\psi$ one reaches to the following equation:

$$i\psi_z - \frac{\beta_2}{2} \psi_{TT} + \gamma |\psi|^2 \psi - \frac{ig}{2}\psi = 0 \tag{69}$$

where z is the normalized propagation distance, T represents the normalized time scale and γ is the nonlinear factor. In this equation, ψ is the electric field amplitude and g represents the gain term. By applying the change of variables $\psi = Ae^{i\phi}$ one gets

$$iA_z e^{i\phi} - A\phi_z e^{i\phi} - \frac{\beta_2}{2}\left[A_T e^{i\phi} + i\phi_T Ae^{i\phi}\right]_T + \gamma A^3 e^{i\phi} - \frac{ig}{2} Ae^{i\phi} = 0 \tag{70}$$

$$iA_z - A\phi_z - \frac{\beta_2}{2}[A_{TT} + 2i\phi_T A_T + i\phi_{TT}A - A\phi_T^2] + \gamma A^3 - \frac{ig}{2}A = 0 \tag{71}$$

By separating the real and imaginary parts, we arrive at two equations as below:

$$A_z = \beta_2 \phi_T A_T + \frac{\beta_2}{2} A \phi_{TT} + \frac{g}{2} A \qquad (72)$$

$$A\left[-\phi_z + \frac{\beta_2}{2}\phi_T^2\right] = \frac{\beta_2}{2} A_{TT} - \gamma A^3 \qquad (73)$$

Since we are looking for a self-similar solution, we assume a solution of the form below:

$$A(z,T) = f(z)F[f^2(z)e^{-gz}T] = fF(\theta)$$

$$\phi(z,T) = \phi(z) + C(z)T^2$$

$$\theta = f^2 e^{-gz} T$$

$$(74)$$

Applying the above change of variables gives

$$\frac{df}{dz}F + fF'(\theta)\, T[2ff' - gf^2]e^{-gz} = \beta_2 f^3 e^{-gz} F'(\theta) 2CT + \frac{\beta_2}{2} fF2C + \frac{g}{2} fF \qquad (75)$$

Separating the terms with T^0 and T' yields two equations as below:

T^0:

$$\frac{df}{dz} = Cf\beta_2 + \frac{g}{2}f$$

$$2\frac{df}{dz} = (g + 2C\beta_2)f$$

$$(76)$$

T':

$$f^2 F'(\theta)[2f' - gf]e^{-gz} = 2C\beta_2 f^3 e^{-gz} F'(\theta)$$

$$2\frac{df}{dz} = (g + 2C\beta_2)f$$

$$(77)$$

Which is the same as the first equation (T^0) and shows the self-consistency. From the second equation we get:

$$fF\left[\frac{\beta_2}{2}4C^2T^2 - \frac{d\phi}{dz} - \frac{dC}{dz}T^2\right] = -\gamma f^3 F^3 + \frac{\beta_2}{2}f^3[F'(\theta)]_T\, e^{-gz}$$

$$fF\left[2\beta_2 C^2 T^2 - \frac{d\phi}{az} - \frac{dC}{dz}T^2\right] = -\gamma f^3 F^3 + \frac{\beta_2}{2}f^5 e^{-2gz}\frac{d^2 F}{d\theta^2} \qquad (78)$$

$$\left[2\beta_2 C^2 - \frac{dC}{dz}\right]f\frac{F\theta^2}{f^4}e^{2gz} - fF\frac{d\phi}{dz} = -\gamma f^3 F^3 + \frac{\beta_2}{2}f^5 e^{-2gz}\frac{d^2 F}{d\theta^2}$$

$$\left[2\beta_2 C^2 - \frac{dC}{dz}\right]\frac{\theta^2}{f^6}e^{2gz} - \frac{1}{f^2}\frac{d\phi}{dz} = -\gamma F^2 + \frac{\beta_2}{2}f^2 e^{-2gz}\frac{F''}{F} \qquad (79)$$

Let $f(0) = A_0$ and $F(0) = 1$. Assume $fe^{-gz} \to 0$ as $z \to \infty$. From this assumption, the term $\frac{F''}{F}$

can be neglected which yields

$$\left[2\beta_2 C^2 - \frac{dC}{dz}\right]\frac{\theta^2}{f^6}e^{2gz} - \frac{1}{f^2}\frac{d\phi}{dz} = -\gamma F^2 \qquad (80)$$

Let $\theta = 0$ where $F(0) = 1$

$$\frac{1}{f^2}\frac{d\phi}{dz} = \gamma \qquad (81)$$

By applying the above substitution one gets to the following equation

$$\left[2\beta_2 C^2 - \frac{dC}{dz}\right]\frac{\theta^2}{f^6}e^{2gz} - \gamma = -\gamma F^2$$

$$\left[2\beta_2 C^2 - \frac{dC}{dz}\right]\frac{\theta^2}{f^6}e^{2gz} = \gamma(1 - F^2) \qquad (82)$$

Let $f = A_0 e^{gz/3}$

$$2f' = (g + 2C\beta_2)f$$

$$\frac{2g}{3}e^{gz/3} = (g + 2C\beta_2)e^{gz/3}$$

$$C = -\frac{g}{6\beta_2} \qquad (83)$$

Replacing C in the above equation gives

$$\left(2\beta_2 \frac{g^2}{36\beta_2^2}\right)\frac{\theta^2}{A_0^6} = \gamma(1 - F^2) \qquad (84)$$

In the normal dispersion regime $\beta_2 > 0$

$$1 - F^2 = \frac{g^2\theta^2}{18\gamma A_0^6\beta_2}$$

$$F^2(\theta) = 1 - \frac{g^2\theta^2}{18\gamma A_0^6\beta_2} \qquad (85)$$

$$F(\theta) = \sqrt{1 - \frac{g^2e^{-2gz}}{18\gamma A_0^6\beta_2}A_0^4\, e^{\frac{4gz}{3}}T^2} \qquad (86)$$

$$A(z,T) = A_0 e^{\frac{gz}{3}}\sqrt{1 - \frac{T^2}{T_p^2(z)}} \qquad (87)$$

which is a parabolic pulse. With a pulse-width as below:

$$T_p = \frac{3\sqrt{2\gamma\beta_2}\, A_0}{g}\, e^{gz/3} \qquad (88)$$

The phase dependency of such a solution is computed from the relation below:

$$\frac{d\phi}{dz} = \gamma f^2 = \gamma A_0^2 e^{\frac{2}{3}gz} \qquad (89)$$

$$\phi(z) = \phi_0 + \frac{3\gamma A_0^2}{2g}\, e^{\frac{2}{3}gz}$$

$$\phi(z,T) = \phi(z) + C(z)T^2$$

$$\phi(z) = \phi_0 + \frac{3\gamma A_0^2}{2g}\, e^{\frac{2}{3}gz} - \frac{g}{6\beta_2}T^2 \qquad (90)$$

In multimode fibers, the gain term can be also a function of z. There are cases where the beam width and hence nonlinearity oscillates along propagation as a result of a presence of energy in the higher-order modes. In these cases, the equations are altered according to the following:

$$i\psi_z - \frac{\beta_2}{2}\psi_{TT} + \frac{\gamma}{q^2(z)}|\psi|^2\psi = 0 \qquad (91)$$

Here, the dispersion is considered to be normal ($\beta_2 > 0$). The following change of variables is applied:

$$\psi = q(z)u$$

$$iu_z q + iuq_z - \frac{\beta_2}{2}\psi_{TT}q + \gamma|u|^2 qu = 0 \qquad (92)$$

Let $g(z)/2 = -q_z/q$. Considering the gain to be of the following dependency

$$q = e^{-\frac{1}{2}G(z)} \qquad (93)$$

$$\frac{dq}{q} = -\frac{1}{2}g(z)dz$$

$$\ln(q) = -\frac{1}{2}G(z)$$

$$q = e^{-\frac{1}{2}G(z)}$$

$$G(z) = \int dz' g(z') \qquad (94)$$

The equation above can also be rewritten as below:

$$iu_z - i\frac{g(z)}{2}u - \frac{\beta_2}{2}u_{TT} + \gamma|u|^2 u = 0 \qquad (95)$$

By applying the change of variable $u = Ae^{i\phi}$

$$A_z = \beta_2\phi_T A_T + \frac{\beta_2}{2}A\phi_{TT} + \frac{g(z)}{2}A \qquad (96)$$

$$A\left[-\phi_z + \frac{\beta_2}{2}\phi_T^2\right] = \frac{\beta_2}{2}A_{TT} - \gamma A^3 \qquad (97)$$

Again, following the same formalism to find a self-similar solution, we assume:

$$A(z,T) = f(z)F[Q(z)T] = fF(\theta); \qquad \theta = Q(z)T \qquad (98)$$

$$\phi = \phi(z) + C(z)T^2 \qquad (99)$$

Assuming the above solutions, after the substitution, we get to the following equations:

$$\frac{df}{dz}F + fF'(\theta)TQ' = \beta_2 2CTfF'(\theta)Q + \frac{\beta_2}{2}fF2C + \frac{g(z)}{2}fF \qquad (100)$$

Separating the terms with dependency to T^0 and T' we one arrives as two equations as below:

T^0:

$$\frac{df}{dz} = \frac{\beta_2}{2}2Cf + \frac{g(z)}{2}f$$

$$2\frac{df}{dz} = [2\beta_2 C + g(z)]f$$

$$2\frac{df}{dz} = [2\beta_2 C(z) + g(z)]f$$

$$(101)$$

T':

$$fQ' = 2\beta_2 CfQ$$

$$Q' = 2\beta_2 CQ$$

$$C(z) = \frac{Q'}{2\beta_2 Q}$$

$$(102)$$

From T^0:

$$2\frac{df}{dz} = [2\beta_2 C(z) + g(z)]f$$

$$2\frac{df}{f} = [2\beta_2 C(z) + g(z)]dz$$

$$\ln(f^2) = \ln(Q) + \int^z g(z')dz'$$

$$f^2 = Qe^{\int^z g(z')dz'}$$

$$f^2 = Qe^{G(z)}$$

$$Q(z) = f^2(z)e^{-\int^z g(z')dz'}$$

$$Q(z) = f^2(z)e^{-G(z)} \qquad (103)$$

From the second equation

$$fF(\theta)\left[-\frac{d\phi}{dz} - \frac{dC}{dz}T^2 + \frac{\beta_2}{2}4C^2T^2\right] = -\gamma f^3 F^3 + \frac{\beta_2}{2}[fF'Q]_T$$

$$fF(\theta)\left[-\frac{d\phi}{dz} - \frac{dC}{dz}T^2 + 2\beta_2 C^2 T^2\right] = -\gamma f^3 F^3 + \frac{\beta_2}{2}fQ^2\frac{d^2F}{d\theta^2} = -\gamma f^3 F^3 + \frac{\beta_2}{2}f^5 e^{-2G(z)}\frac{d^2F}{d\theta^2}$$

$$(104)$$

Again we assume $fe^{-G(z)} \to 0$ as $z \to \infty$. From this assumption, the last term can be neglected

$(\frac{\beta_2}{2}f^5 e^{-2G(z)}\frac{d^2F}{d\theta^2} \approx 0)$ which yields

$$-f\frac{d\phi}{dz} - \frac{dC}{dz}T^2 f + 2\beta_2 C^2 T^2 f = -\gamma f^3 F^2$$

$$-f\frac{d\phi}{dz} + \left[2\beta_2 C^2 - \frac{dC}{dz}\right]T^2 f = -\gamma f^3 F^2$$

$$\left[2\beta_2 C^2 - \frac{dC}{dz}\right]\frac{1}{f^2}T^2 - \frac{1}{f^2}\frac{d\phi}{dz} = -\gamma F^2 \qquad (105)$$

By replacing $\theta = Q(z)T$

$$\left[2\beta_2 C^2 - \frac{dC}{dz}\right]\frac{1}{f^2}\frac{\theta^2}{Q^2(z)} - \frac{1}{f^2}\frac{d\phi}{dz} = -\gamma F^2 \qquad (106)$$

Again for $\theta = 0, F(0) = 1, f(0) = A_0, G(0) = 0$

$$\frac{d\phi}{dz}\frac{1}{f^2} = \gamma \qquad (107)$$

Let

$$\left(2\beta_2 C^2 - \frac{dC}{dz}\right)\frac{1}{Q^2 f^2} = \gamma a^2 \qquad (108)$$

where a is determined by the initial conditions

81

$$\gamma a^2 \theta^2 - \gamma = -\gamma F^2 \quad \rightarrow \quad \gamma(F^2 - 1) = -\gamma a^2 \theta^2$$

$$F^2 = 1 - a^2 \theta^2$$

$$F = \sqrt{1 - a^2 \theta^2}$$

$$F = \sqrt{1 - a^2 Q^2 T^2} = \sqrt{1 - \frac{T^2}{T_p^2(z)}} \tag{109}$$

Which is again a parabolic pulse with $T_p(z) = \frac{1}{aQ}$. To find $Q(z)$ one needs to solve the following

equation:

$$2\beta_2 - \frac{dC}{dz} = \gamma a^2 Q^2 f^2 = \gamma a^2 Q^2 Q e^{G(z)} \tag{110}$$

$$C = \frac{Q'}{2\beta_2 Q}$$

$$\frac{2\beta_2}{4\beta_2^2} \frac{Q'^2}{Q^2} - \frac{1}{2\beta_2} \frac{Q''Q - Q'^2}{Q^2} = \gamma a^2 Q^3 e^{G(z)}$$

$$\frac{Q'^2}{Q^2} - \frac{(Q''Q - Q'^2)}{Q^2} = 2\beta_2 \gamma a^2 Q^3 e^{G(z)}$$

$$2Q'^2 - QQ'' = 2\beta_2 \gamma a^2 Q^5 e^{G(z)}$$

$$QQ'' - 2Q'^2 + s(z)Q^5 = 0 \tag{111}$$

$$s(z) = 2\beta_2 \gamma a^2 e^{G(z)} \tag{112}$$

This equation can be solved analytically and also through a Runge-Kutta method.

5.2 gUPPE and BPM Numerical Simulation Results

In order to confirm the theoretical results, a number of numerical simulations have been conducted

using a gUPPE simulation scheme. Figure 5-1 shows the temporal evolution of a 500-fs pulse with

~63 nJ energy when it is launched in a tapered multimode fiber of 50 cm when its core radius is

linearly decreasing from 40 to 10 μm. The pump's central wavelength is considered to be at 1064

nm and hence experiences a normally dispersive condition. As it is clear in this figure as the input
beam goes through the tapered fiber, it experiences an amplification. Figure 5-2 shows the
temporal distribution of the output pulse and the chirp associated with this pulse.
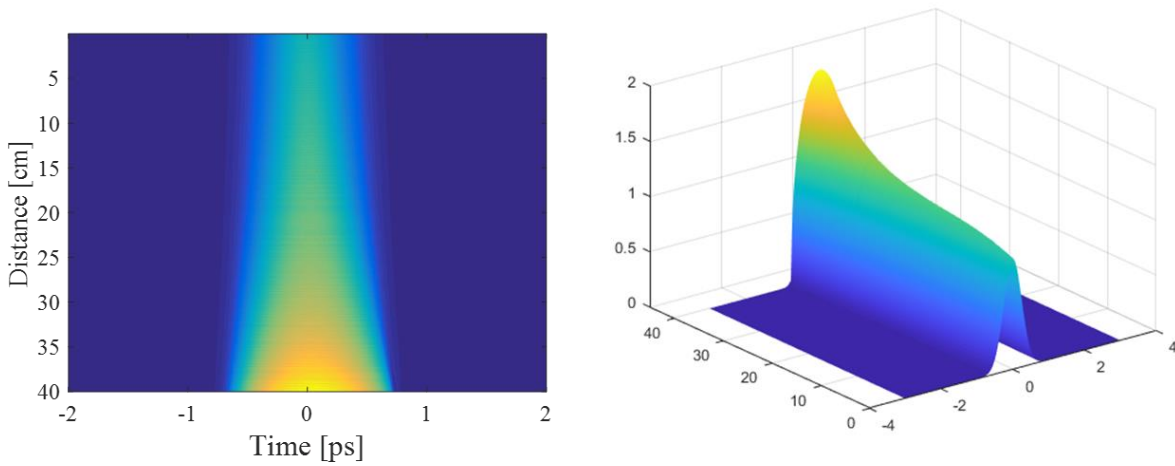
Figure 5-1 The temporal evolution of an input pulse of 500 ps pulse-width and ~63 nJ energy in
a tapered MM fiber of 50 cm when the core diameter decreases from 80 to 20 μm
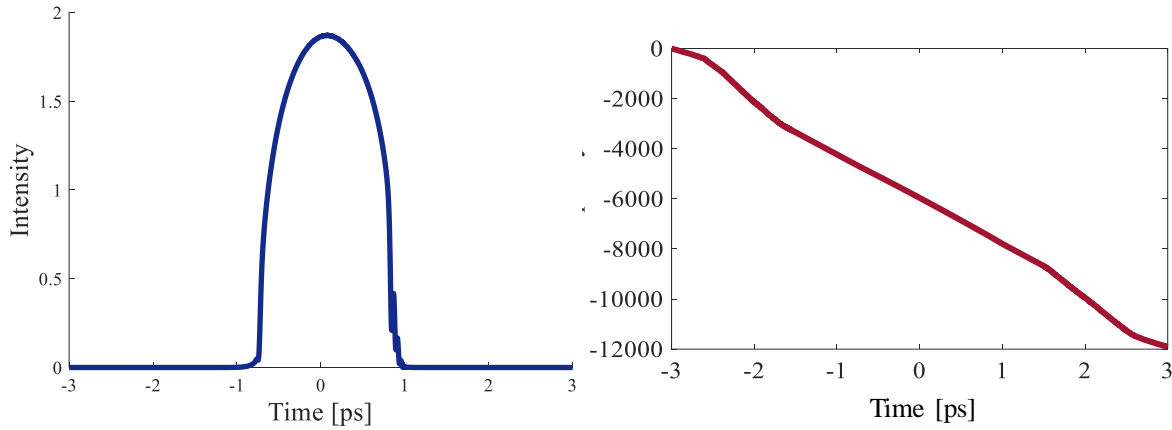
Figure 5-2 The temporal pulse shape of the beam (left) after going through the taper section
converges into a parabolic shape pulse. (right) The chirp associated with this pulse.

As it can be seen from this figure, the pulse has developed into a parabolic shape pulse with a large
linear chirp. The spectral evolution corresponding to the above-mentioned simulation is shown in

Figure 5-3. The pulse in the output of the fiber has a large bandwidth. In principle, by increasing the input power level and utilizing shorter fibers with higher core decreasing ratio, one can access bandwidths much greater than 100 nm and at the same time suppress the pesky spontaneous Raman effects.
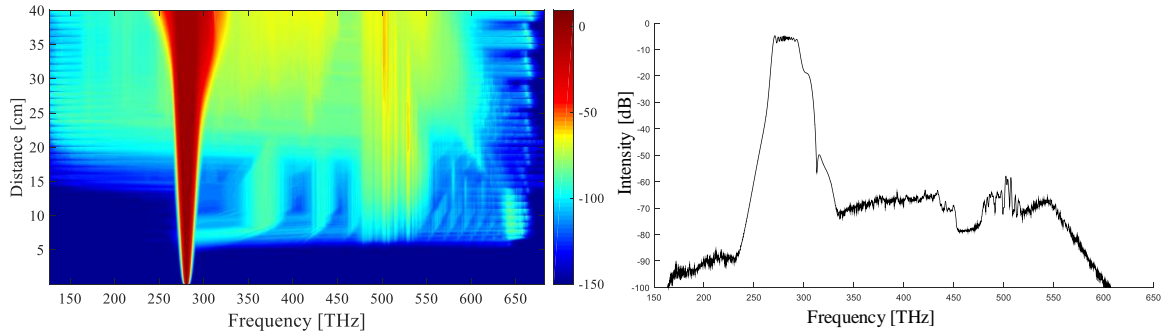
Figure 5-3 The spectral evolution (left) and the terminal spectrum (right) corresponding to the parabolic pulse in Figure 5-2.

The second simulation used the same parameters as the first experiment except for the fiber taper that was considered to be twice the length (1m). The temporal evolution associated with this case is demonstrated in Figure 5-4. In this case, the pulse initially experiences the spectral and temporal broadening. In the later stages when the broadening effect diminishes and gain effects become more significant, the pulse starts to develop into a parabola. The shallow pedestal around the strong signal belongs to the energy present in higher-order modes that has dispersed along propagation. Figure 5-5 shows the temporal pulse in the output of the tapered multimode fiber. The chirp associated with this pulse is shown in the same figure.
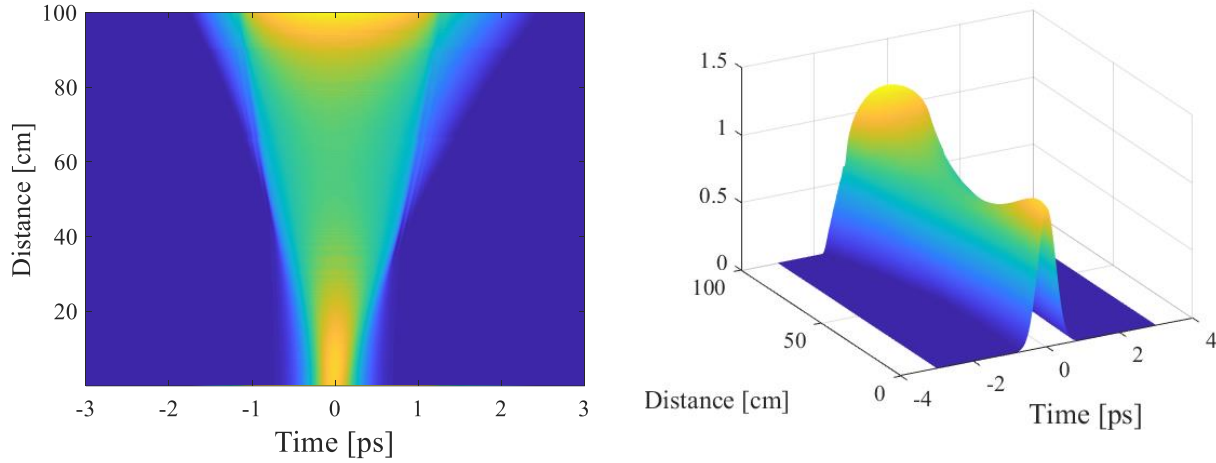
Figure 5-4 The temporal evolution of an input pulse of 500 ps pulse-width and ~63 nJ energy in a tapered fiber of 1 m when the core diameter decreases from 80 to 20 μm
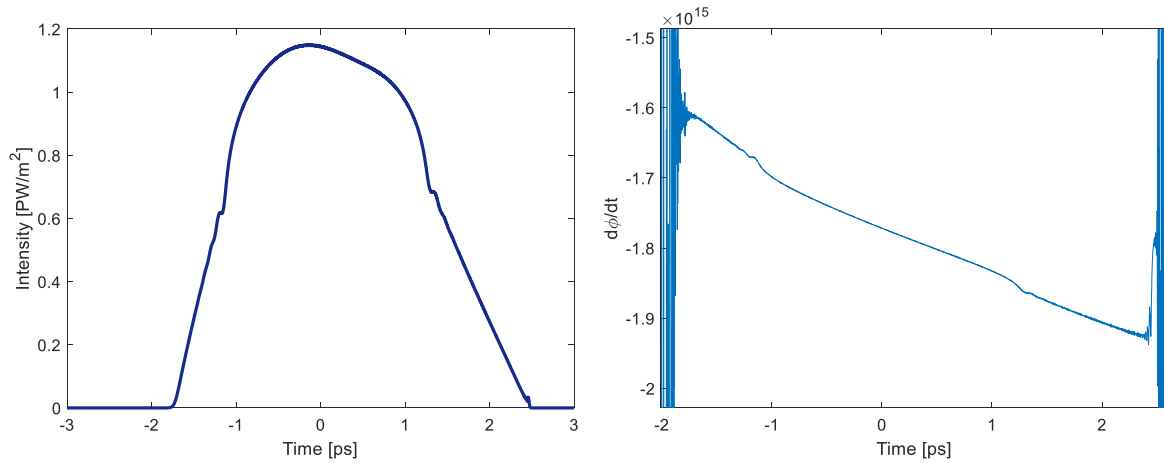
Figure 5-5 The temporal pulse shape of the beam (left) after going through the taper section converges into a parabolic shape pulse. (right) The chirp associated with this pulse.

As it can be seen in this figure, the residual energy from higher-order modes disperses and makes a pedestal around the main pulse. For longer propagations this effect becomes negligible. The main reason is that in the actual experiments much longer tapers of 10-30 m are exploited. In such cases, the energy very soon and under the action of beam self-cleaning effect couples to the fundamental mode. However, a small amount of energy stays in the higher-order modes which disperses and leaves minimal effects on the output pulse.

85
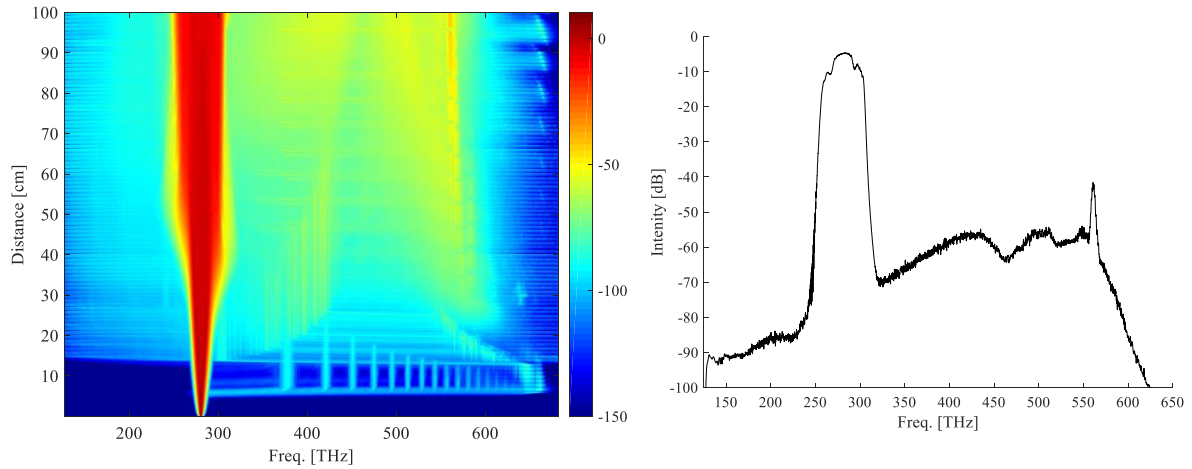
Figure 5-6 The spectral evolution (left) and the terminal spectrum (right) corresponding to the parabolic pulse in Figure 5-4

The spectral evolution corresponding to the second simulation (Figure 5-6), shows that for longer fiber case, the ultimate bandwidth of the output pulse is narrower. This is because of the fact that in this case, the pulse peak power in the output of the fiber is smaller than the first example. Our BPM simulations also show that this parabolic pulse formation is indeed an attractor solution. Figure 5-7 shows the pulse evolution when the input pulse has a parabolic chirp. The input chirp is compensated upon propagation in the fiber and becomes linear. The pulse shape evolves into a parabolic pulse shape in time. For this example, the input pulse was considered to be centered on 1030 nm with a peak power of 100 kW. The taper has a length of 30 m with the fiber core diameter reducing from 300 to 20 μm. In the next example, the same fiber and pulse parameters were used to excite the multimode fiber taper except for the pulse shape. The pulse shape was chosen to be arbitrary in this case (Figure 5-8). The pulse evolution, in this case, shows that the pulse evolves into the parabolic pulse shape independent of the input pulse properties. This shows that the parabolic pulse is indeed an attractor solution.
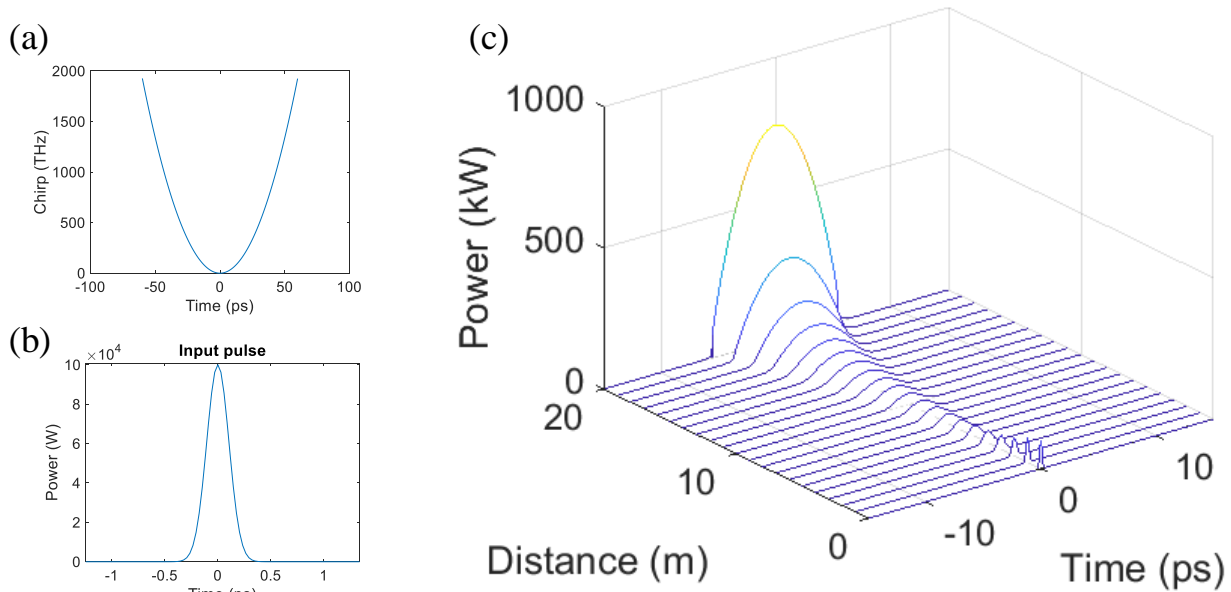
Figure 5-7 (a) The chirp of the input pulse. (b) The input pulse shape. (c) The evolution of the chirped input pulse in time and space shows that the pulse eventually evolves into a parabolic pulse.
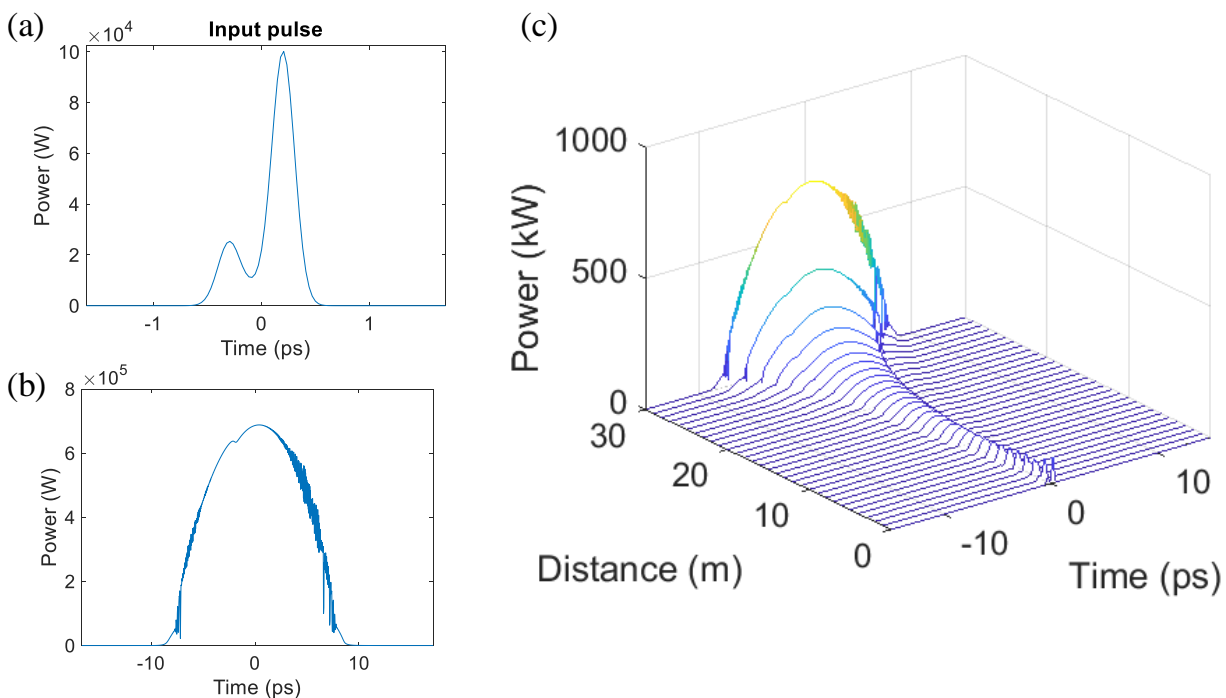
Figure 5-8 (a) The input pulse with an arbitrary pulse shape. (b) The output pulse with a parabolic pulse shape. (c) The evolution of the chirped input pulse in time and space shows that the pulse evolves into a parabolic pulse independent of the input pulse shape.

A series of experiments were conducted to verify the theoretical results. To this end, 300 fs pulses with peak powers ranging from 100s of kW to MW levels with a repetition rate of 1 MHz were launched into the fiber. The laser source used in this experiment was an Amplitude Satsuma fiber laser. To do this experiment, we used in-house multimode fiber tapers with a core radii decreasing from 300 to 20 μm over a course of 50 m. A custom-made FROG system was used to measure the output pulse. Figure 5-9 and Figure 5-10 show the spectrograph and the spectrum of the output pulse. The pulses used for this experiment had peak powers of 150 and 130 kW respectively. The output pulses have prohibitively large time-bandwidth product which makes it impossible to retrieve the pulse information from them. However, both spectrographs clearly have the diamond shape which is a signature of pulses with a linear chirp. In the next step in this project, we will employ compression gratings to compress these pulses before performing a FROG measurement.
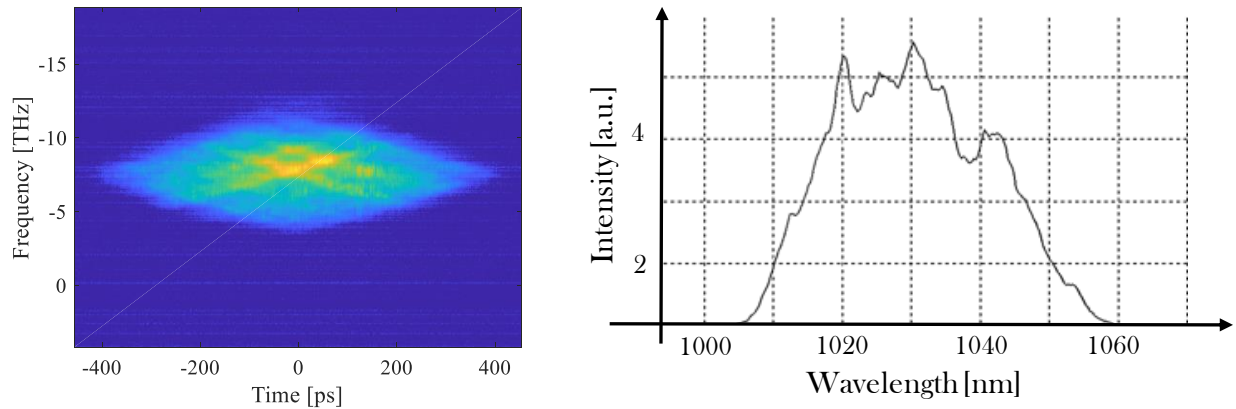
Figure 5-9 The spectrograph (left) and spectrum (right) measured at the end of a 50-m long fiber taper when its core diameter decrease from 300 to 20 μm. The input pulse has a pulse-width of 300 fs with a peak power of 150 kW. The diamond shape of the spectrogram is an indicator of the pulse linear chirp.
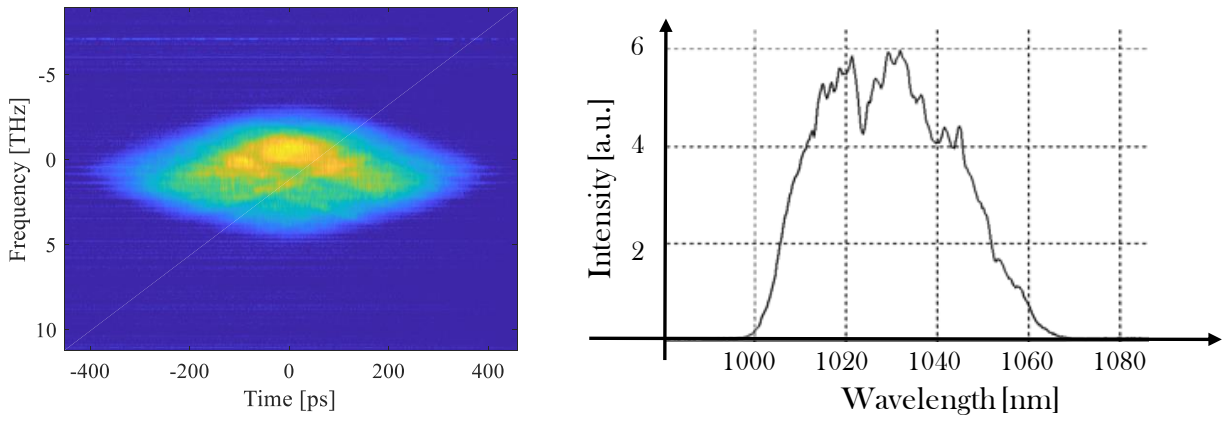
Figure 5-10 The spectrograph (left) and spectrum (right) measured at the end of a 50 m long fiber taper when its core diameter decrease from 300 to 20 μm. The input pulse has a pulse width of 300 fs with a peak power of 130 kW. The diamond shape of the spectrogram is an indicator of the pulse linear chirp.

CHAPTER 6: EFFICIENT SECOND-HARMONIC GENERATION IN PARABOLIC-INDEX MULTIMODE FIBERS

The results presented in this section have been published and can be found at : M. A. Eftekhar, Z. Sanjabi-Eznaveh, J. E. Antonio-Lopez, F. W. Wise, D. N. Christodoulides, and R. Amezcua-Correa, "Instant and efficient second-harmonic generation and downconversion in unprepared graded-index multimode fibers," Opt. Lett. **42**, 3478-3481 (2017) [70]

Second harmonic generation (SHG) in silica single-mode optical fibers was first reported by [93,94]. This was quite surprising given that amorphous systems like silica glass are not expected to exhibit a $\chi^{(2)}$ nonlinearity. This, in turn, incited considerable interest in the physics and applications of these effects, especially in single-mode fibers [95–100]. In early experiments, SHG was observed only after preparing the fiber by exposing it to the pump wavelength for several hours. While this process still remains poorly understood, a number of schemes have proved effective in increasing its conversion efficiency and reducing the required preparation time. Such techniques include for example, seeding a fiber with a second-harmonic (SH) signal along with the pump light [95], using polling techniques like thermal [101,102] and corona poling [103], and applying a transverse dc electric field in order to break the inversion symmetry of the material system [97]. Electron implantation was also utilized along similar lines [104]. It is important to note that, most of these experiments were conducted primarily in single-mode or few-mode fibers where only the fundamental mode was excited [105].

Second-harmonic generation was also recently observed along with their GPI sidebands in optically polled graded-index multimode fibers [106]. In this study, the fiber was first prepared

by exposing it for a few minutes, to a second-harmonic signal generated from a KTP crystal. Subsequently, SHG conversion up to 1% was reported, a few hours after the fiber was prepared.

Here, we experimentally demonstrate high SHG conversion efficiencies ~6.5% in heavily multimode parabolic-index germanium-doped optical fibers. Unlike previous studies, this conversion occurred without first preparing the fiber via any of the schemes outlined before. Even more importantly, the SHG was found to reach a maximum in an almost instantaneous manner. In our experiments, this frequency-doubling was also accompanied by an efficient down-conversion process in the near-IR regime (2128 nm). The effect of input pump power on the efficiency of these processes was also investigated. Cutback measurements performed on our fiber revealed that SHG effectively unfolded along the first 4-5 meters. In all cases, the recorded output beam profiles (pump and SH) were found to exhibit a Gaussian-like shape and a speckle-free pattern.
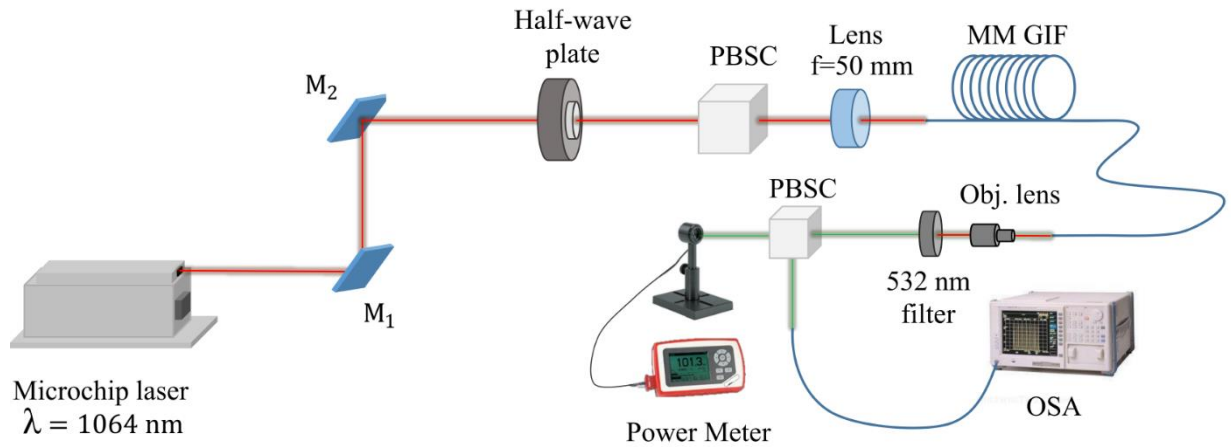
Figure 6-1 Schematic of the setup used for SHG and down-conversion in MMFs. Pulses from a Q-switched microchip laser at 1064 nm are coupled into a MMF. PBSC: polarizing beam splitter cube, M_1 and M_2: Mirrors, OSA: Optical spectrum analyzer.

A schematic representation of the experimental setup used is depicted in Figure 6-1. The optical source is an amplified Q-switched microchip laser, producing 400 ps pulses at a repetition rate of 500 Hz and with peak powers up to 200 kW. Each pulse carries ~ 95 µJ of energy at 1064 nm. The

laser beam is coupled to the multimode fiber samples using a 50 mm focal length lens with efficiencies exceeding 80%. To control the input power, a half-wave plate and a polarizing beam splitter cube (PBSC) were employed. The fiber was fixed on a three-axis translation stage. The visible and NIR portions of the output spectra were collected by a multimode patch cord and were analyzed using two different optical spectrum analyzers (OSA) covering the wavelength range from 350 to 1750 nm (ANDO AQ 6315E) and 1200 to 2400 nm (Yokogawa AQ6375). To record the beam profile of the second-harmonic signal, a CCD camera was used along with a 532-nm filter having 10 nm FWHM. In our experiments, two different MMFs were utilized. The first one was a low differential modal group delay multimode graded-index fiber with a core diameter of 50 µm and a refractive index contrast of 1.6×10^{-2}. The second MMF was of the step-index type having a numerical aperture of 0.22 and a core diameter of 105 µm. Both these fibers were germanium-doped and fabricated by Prysmian Group. At 1064 nm, the parabolic MMF used is expected to support ~250 modes while at 532 nm ~1000 modes.

The output spectra, collected at the end of a 5-m long parabolic-index MMF are depicted in Figure 6-2 for three different input power levels. Figure 6-2(a) shows the spectrum when the average input power is ~16 mW (P_{p-p}= 80 kW). In addition to pump and Raman sidebands, a distinct peak at 532 nm is clearly visible signifying the onset of SHG. This peak is accompanied by another rather strong line located at 560 nm, resulting from the frequency-doubling of the first Stokes Raman peak (R_1) at 1.118 µm. As it can be seen in Figure 6-2(b), by increasing the input power, a few other peaks start to appear in the vicinity of the pump's second-harmonic. In particular, the line at 587 nm corresponds to the frequency-doubling of the second Stokes Raman wave at 1.176 µm. In addition, two other peaks can be prominently seen at 546 nm and 577 nm. The first one can be attributed to a sum-frequency generation of the pump and the first Stokes peak while the second

one to a sum-frequency generation resulting from the first and second Stokes Raman peaks. This clearly indicates that the $\chi^{(2)}$ response of the fiber is indeed at play. Other significant frequency peaks appearing around 720 nm correspond to sidebands generated from GPI, that takes place in parabolic multimode fibers as also demonstrated in previous studies [29,42]. It should be noted that the distinct feature seen at 806 nm is the residual pump from our laser. By further raising the input power, a series of peaks starts to emerge between 420 and 490 nm, which can be ascribed to sum frequency generation between the pump or the Raman peaks and the first visible GPI sideband located at 720 nm (Figure 6-2 (c)).

Figure 6-3 shows the NIR portion of the spectrum which also displays a series of peaks. The strongest line in this region is located at 2.128 μm, corresponding to the down-converted wavelength of the pump, generated along with the second-harmonic because of the $\chi^{(2)}$ nonlinearity. Our experiments revealed that any change in the power level of the produced SH was always accompanied by a similar change in the down-converted signal. Another significant feature in this figure is the spectral band around 2 μm. This line corresponds to the first NIR-GPI sideband. Some of the spectral components between 2.13 μm and 2.35 μm also match the down-conversion of the first Stokes Raman waves. As a next step, we repeated these experiments in the previously mentioned step-index MMF. Even in this case, the presence of the second-harmonic was evident in the spectrum. However, our measurements showed that the generated green light (SH) was always very weak, by almost two orders of magnitude below that observed in the parabolic fiber. Further increasing the input pump power or prolonging the exposure time of this step-index MMF to the pump did very little in enhancing the generated SH signal. The same is also true for the down-converted wavelength. One possible explanation behind this difference in performance can be attributed to the GPI process that is only possible in parabolic fibers.
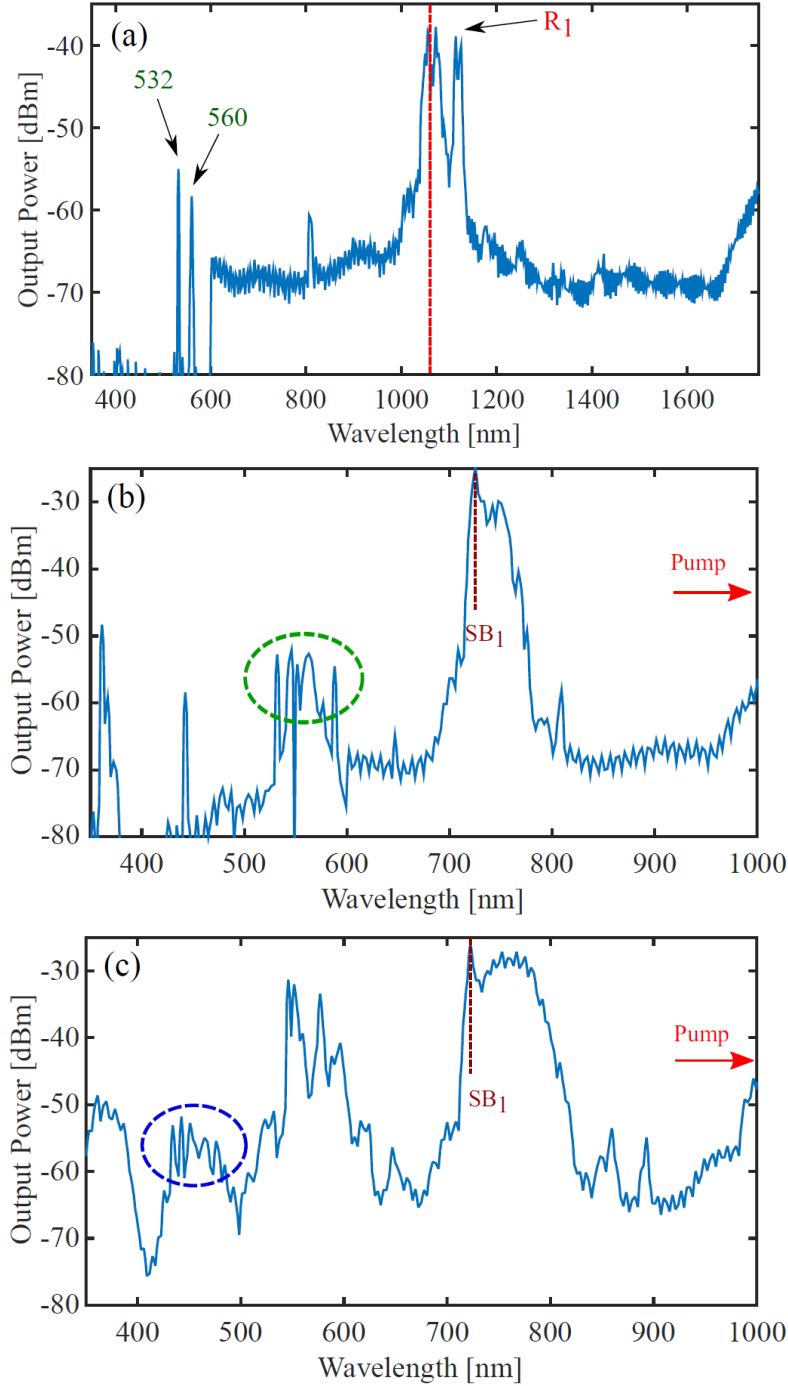
Figure 6-2 (a) Output spectrum measured at the end of a 5-m long parabolic MMF when excited with 400 ps 80 kW peak power pulses. SHG from the pump is evident at 532 nm. The line at 560 nm is due to the frequency-doubling of first Stokes Raman wave. (b) Increasing the input pump power to 110 kW results in the appearance of extra peaks in the vicinity of 532 nm (green cluster). (c) A further increase in the input pump power to 140 kW leads to other $\chi^{(2)}$ induced peaks in the 420-490 nm (blue cluster) wavelength range. SB_1 represents the first GPI sideband.

One of the direct byproducts of GPI is the generation of strong lines both in the visible as well as the UV part of the spectrum. As it has been shown before, exposing the fiber to green, blue or the UV wavelengths can enhance SHG up to 10 times [107]. As a result, in our experiments, the GPI-induced wavelengths in the red/blue, may act as enabling sources in "preparing" the fiber towards generating more efficiently the SH and down-converted signals.
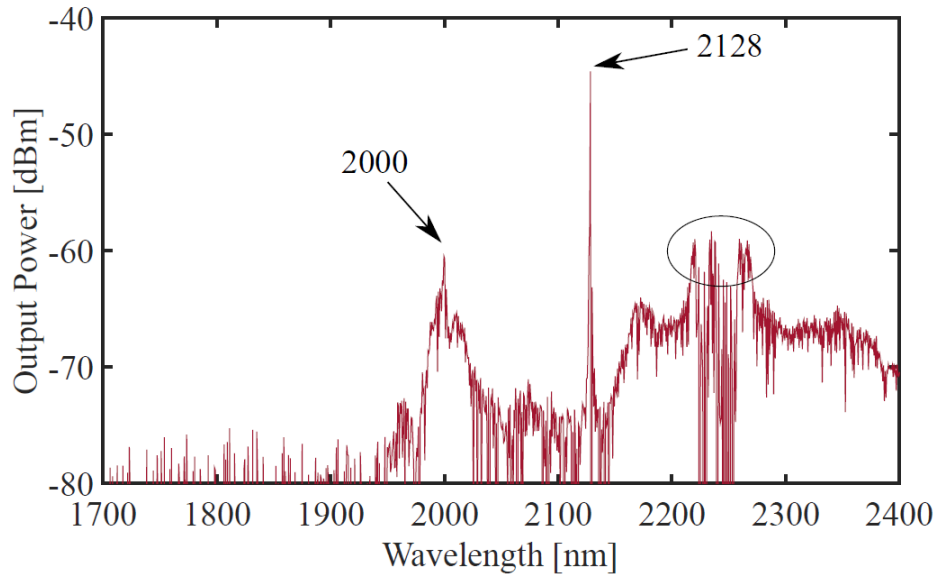
Figure 6-3 NIR portion of the spectrum collected at the end of a 5-m long parabolic MMF when pumped at 110 kW peak power. The prominent peak at 2128 nm corresponds to the pump down-conversion. The peak at 2 µm results from the first NIR GPI-sideband.
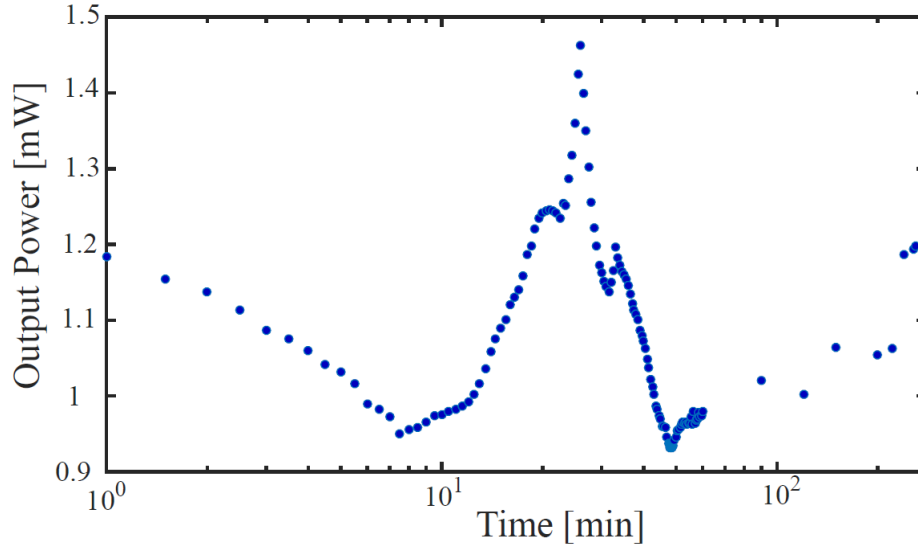
Figure 6-4 Temporal evolution of the generated second-harmonic, measured at the output of a 5-m long GI-MMF. The peak power used was 110 kW. The measurements were carried out for over 4 hours. Once the oscillations settle down, the SH power level is restored to its initial value.

A surprising result in our experiments was the fact that SHG occurred almost instantaneously in the parabolic MMF – even in the absence of any preparation. Figure 6-4 demonstrates the evolution of the generated SH in a 5 m long parabolic fiber as a function of time. A 532-nm bandpass filter was used to select the second-harmonic signal. The ensued SHG was monitored for 4 hours. The pump signal was initially blocked for a few minutes before initiating these measurements. As soon as the pump was unblocked, green light at 532 nm always emerged and was measured using a power meter. To make sure that this instant SHG does not result from any previous exposure of the fiber to the pump, we repeated this same experiment with totally unexposed fiber segments. In all cases, SHG took place almost immediately after the laser beam was coupled into the fiber. As it can be seen in Figure 6-4, the SH output power experiences fluctuations during the first few minutes. Our observations indicate that these oscillations become progressively less pronounced and as a result, the output SH slowly stabilizes around its initial value. It is worth mentioning that these fluctuations ($\pm$10%) are always present. This behavior can be explained by considering the

continuous formation and erasure of internal gratings induced by the co-propagating GPI-sideband colors. The reason behind this instant build-up of the $\chi^{(2)}$ process is still unclear to us.
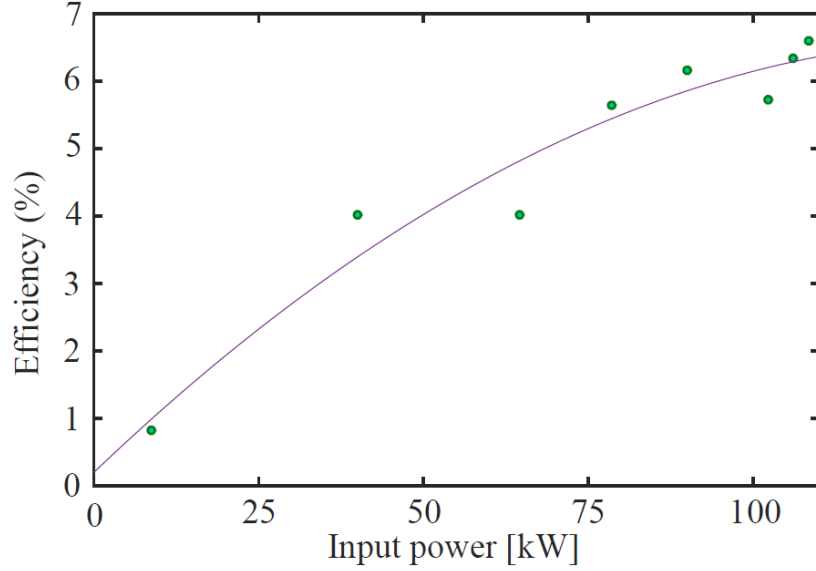
Figure 6-5 Output power conversion SH efficiency measured at the end of a 5-m long GI-MMF. The SHG monotonically increases with the pump power. The process saturates at 100 kW.

In another set of experiments, we investigated the dependence of the conversion efficiency on the input pump power. These studies were conducted again in a 5 m long parabolic MMF. These results are shown in Figure 6-5. For each power level, the initial conditions were tuned to yield the highest attainable SHG efficiency. As demonstrated in this figure, the efficiency of this process tends to monotonically increase with pump power. However, once the average input powers exceed 20 mW ($\sim P_{p-p}$=100 kW) the SHG saturates and the hence the efficiency no longer changes. In this regime, the maximum achievable peak power conversion was found to be ~6.5%, which to the best of our knowledge, is among the highest observed in unprepared fibers.
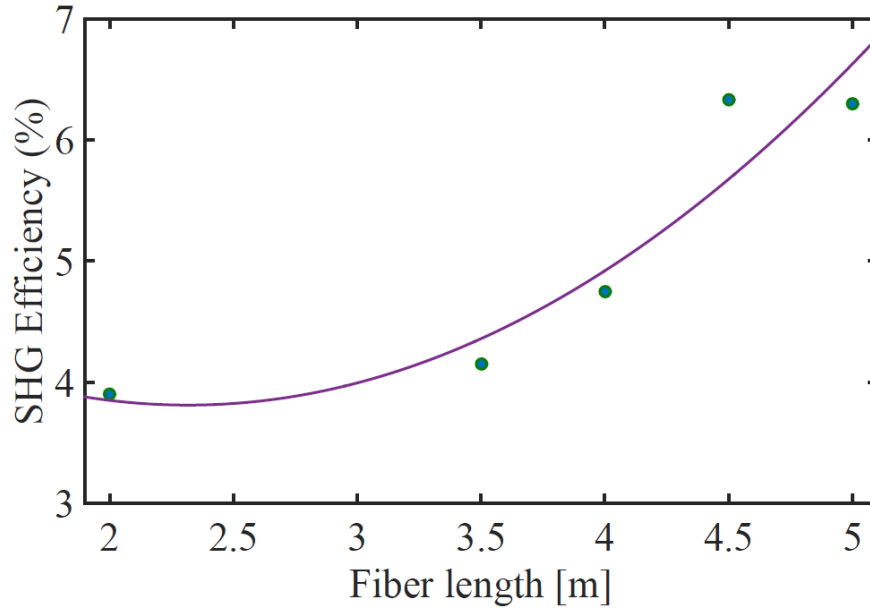
Figure 6-6 Power conversion efficiency for different fiber lengths. The efficiency tends to increase with distance in the parabolic MMF.

The effect of fiber length on the SHG process was previously investigated in single-mode fibers. In these studies, it was found that only the first few tens of centimeters are responsible for SHG []. Here, we probed the same behavior in parabolic MMFs having different lengths. These results are depicted in Figure 6-6. As opposed to single-mode fibers, in our case, we found that the SHG kept increasing with distance, way beyond the first 50 cm Figure 6-6 and it only seems to saturate after 4.5 meters.

The output beam profile distributions at the pump wavelength and SH (532 nm) are plotted in Figure 6-7 for different pump power levels. In accord with previous observations [42,44], the beam at the pump wavelength was found to be clean and speckle-free. Similarly, the beam profile for the SH 532 nm line had a Gaussian-like shape and was again speckle-free, a surprising result given the low power levels at SH (532 nm). This may be due to the fact the pump clean-up, in turn, induces a similar effect in the SH, i.e. by populating lower-order modes.
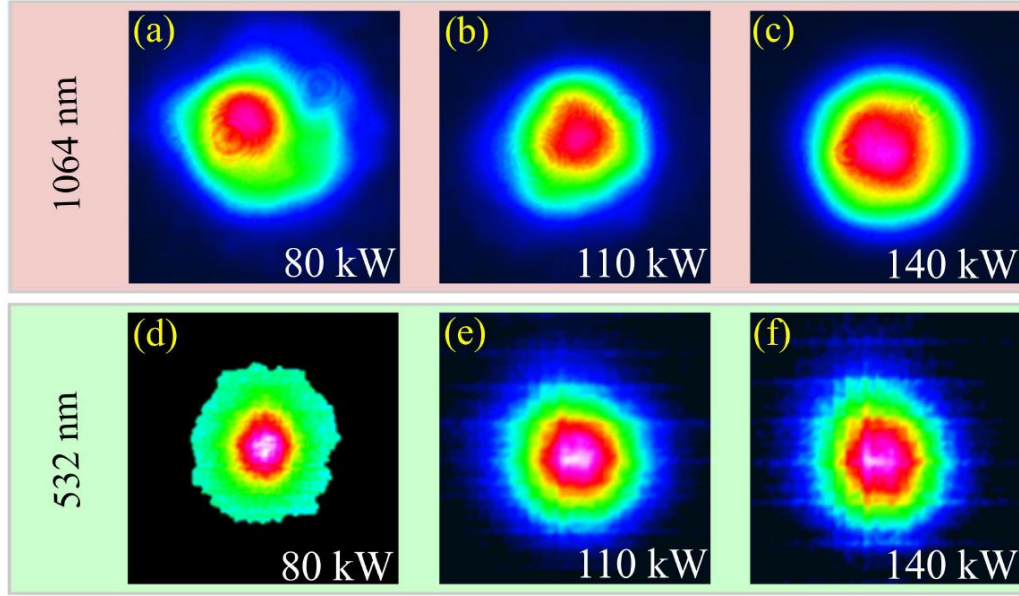
Figure 6-7 Output beam profile at 1064 nm (a-c) and 532 nm (d-f) after a 5 m long parabolic MMF, as a function of input power.

In conclusion, we have shown that germanium-doped parabolic multimode silica fibers can exhibit relatively high SHG conversion efficiencies and down-conversion. Unlike previous experiments, these $\chi^{(2)}$ related processes occurred immediately without any preparation. Of interest would be to consider the potential of the $\chi^{(2)}$ down-conversion process as a source for biphoton generation in quantum optics. Our results may pave the way towards alternative platforms for SHG and down-conversion.

CHAPTER 7: SUPERMODES IN MULTI-RING HONEYCOMB STRUCTURES

The results presented in this section have been published and can be found at: C. Xia, M. A. Eftekhar, R. Amezcua-Correa, J. E. Antonio-Lopez, A. Schülzgen, D. N. Christodoulides, G. Li, "Supermodes in Coupled Multi-Core Waveguide Structures," in *IEEE Journal of Selected Topics in Quantum Electronics*, vol. 22, no. 2, pp. 196-207, March-April 2016 [108]

7.1 Introduction

Supermodes are eigenmodes of composite structures involving coupled constituent elements, each of which also supporting guided modes in isolation [1, 2]. As indicated in a number of studies, such multi-core systems can be effectively analyzed using coupled-mode theory (CMT) - which is particularly effective when the coupling between neighboring elements is relatively weak. Over the years, the properties of supermodes in either linear [3] or ring arrays of coupled waveguides have been analyzed using CMT methods [4-6]. Even in the simplest possible configuration of two coupled channels, supermodes play an important role given that their interference is the one responsible for the energy exchange behavior in a directional coupler.

Quite recently, supermodes have received renewed interest within the context of mode-division multiplexing (MDM), a new transmission method aimed at overcoming the capacity limit of single-mode fiber communication systems. Since modes tend to couple during long-distance fiber transmission, unraveling mode crosstalk using multiple-input-multiple-output (MIMO) digital signal processing (DSP) is necessary for demultiplexing MDM channels [7]. In the presence of modal group dispersion, the computational load for MIMO DSP is proportional to the modal group delay [8]. Interestingly, coupled multi-core fibers can be designed to have reduced modal group

delays and/or larger effective areas in comparison with few-mode fibers (FMF) [9]. In a recent experiment, the modal delay was also found to depend sublinearly on transmission distance in the presence of strong supermode coupling [10]. It is thus imperative to study the properties of optical supermodes in a systematic manner.

7.2 Supermodes in Multi-ring Honeycomb Structures

Honeycomb waveguide arrangements have been intensely investigated over the years [12-19]. Their close-packed geometry makes them ideal for multi-core fiber application. In this section, we develop a general methodology capable of analyzing supermodes in multi-ring honeycomb waveguide lattices, consisting of any number of layers. In addition to hexagonal systems, this versatile technique can be used in other regular polygonal configurations. In brief, our approach is based on separately formulating an eigenvalue problem for in-phase supermodes and another for modes with orbital angular momentum. This can be achieved by appropriately grouping the constituent waveguide elements based on their topology. Here, this approach is explicitly demonstrated in honeycomb arrangements involving 7, 19, and 37 sites.

We begin our analysis by assuming that in all cases, each waveguide element is assumed to be cylindrical (of radius a) and single-moded, i.e. it only supports the LP_{01} mode, with a propagation constant β_0. The coupling coefficient κ between waveguide channels can then be obtained using coupled-mode theory. If the distance between core centers, i.e., the core pitch is D, this coupling strength is given by [20, 21]:
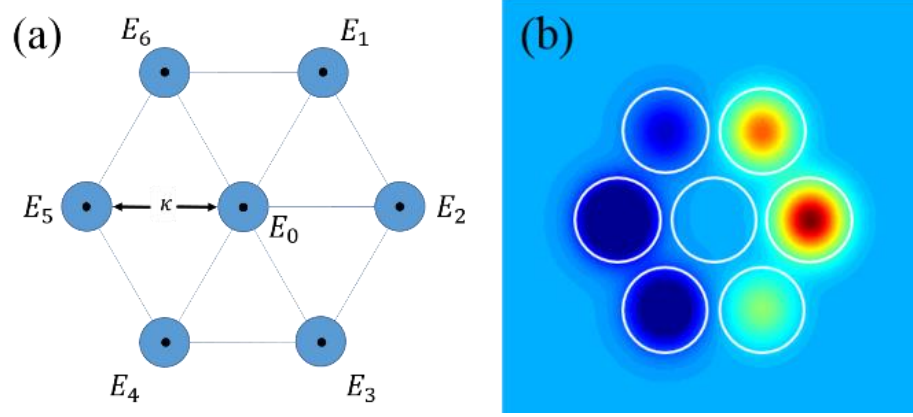
Figure 7-1 (a) A 7-core hexagonal lattice. All single mode waveguide elements interact with their nearest neighbors with a coupling strength κ. (b) Real part of the field distribution $(\sim \cos(Qn))$ associated with the DS_{11} supermode.

$$\kappa = \frac{\sqrt{2\Delta}}{a} \frac{U^2}{V^3} \frac{K_0(WD/a)}{K_1^2(W)} \qquad (113)$$

where $\Delta = (n_c - n_s)/n_c$ is the waveguide index difference and n_c, n_s are the core and cladding refractive indices, respectively. $V = k_0 a n_c \sqrt{2\Delta}$ is the dimensionless V-number involved in the eigenvalue problem describing the fundamental mode LP_{01} of the waveguide, e.g. $UJ_1(U)/J_0(U) = WK_1(W)/K_0(W)$ In the last equation, $U = a(k_0^2 n_c^2 - \beta^2)^{1/2}$, $W = a(\beta^2 - k_0^2 n_s^2)^{1/2}$, where $K_1(x)$ and $J_1(x)$ are Bessel functions of order l. The propagation constant β can be determined from the eigenvalue problem by keeping in mind that $V^2 = U^2 + W^2$.

In this section, we will exemplify our method in the case of a 7-, 19-, and 37-core hexagonal lattice. Even though both the 7- and 19-core systems have been previously analyzed using either direct schemes or linear algebraic methods [15, 18, 19], here we will still apply our methodology to these same geometries for demonstration purposes.

A 7-core arrangement is shown in Figure 7-1(a). In this multi-core system, the modal fields evolve according to:

$$i\frac{dU_0}{dz} + \beta_0 U_0 + \kappa \sum_{n=1}^{6} U_n = 0 \qquad (114)$$

$$i\frac{dU_n}{dz} + \beta_0 U_n + \kappa U_0 + \kappa(U_{n+1} + U_{n-1}) = 0 \qquad (115)$$

In Eq. (115), we only account for nearest neighbor interactions in this hexagonal system. By introducing a gauge transformation $U_n = u_n exp(i\beta_0 z)$ and by adopting a dimensionless coordinate $Z = \kappa z$ one arrives at

$$i\frac{du_0}{dZ} + \sum_{n=1}^{6} u_n = 0 \qquad (116)$$

$$i\frac{du_n}{dZ} + u_0 + (u_{n+1} + u_{n-1}) = 0 \qquad (117)$$

Figure 7-2 (a) A 19-core hexagonal lattice. The waveguide elements are grouped into 4 different families (a, b, c, d) indicated with different colors. (b) By excluding the central core, the remaining elements of these families are in addition grouped in each hexagonal sector in order to obtain supermodes having angular momenta.

In all cases, the modes can be re-expressed in terms of actual quantities and coordinates in a straightforward fashion. In solving this problem, we look for discrete supermodes, henceforth denoted as S_{lm} , where the discrete index l represents an orbital angular momentum and m is the root number of the corresponding eigenvalue equation. To obtain the seven supermodes of the

structure depicted in Figure 7-2(a), we first seek in-phase modes of the type DS_{0m} that represent to some extent discrete analogues to the continuous LP_{0m} modes in standard cylindrical waveguides [21, 22]. Under this assumption and by exploiting the symmetry of this problem, one can identify two species, u_a , u_b where $u_a = u_b$ and $u_b = u_1 = u_2 = \cdots = u_6$. From Eqs. (116) and (117), we find that $idu_a/dZ + 6u_b = 0$ and $idu_b/dZ + 2u_b + u_a = 0$. To obtain the dispersion relation of these in-phase modes we assume solutions of the type $u_a = u_a^0 e^{i\lambda z}$ and $u_b = u_b^0 e^{i\lambda z}$ that directly lead to an algebraic eigenvalue equation for the normalized propagation constant λ, $\lambda^2 - 2\lambda - 6 = 0$, with solutions $\lambda = 1 \pm \sqrt{7}$ As we will see these two eigenvalues correspond to the two in-phase supermodes DS_{01} and DS_{02}. From here, the eigenvectors $[u_a^0, u_b^0]$ can be readily deduced from the corresponding eigenvalue problem.
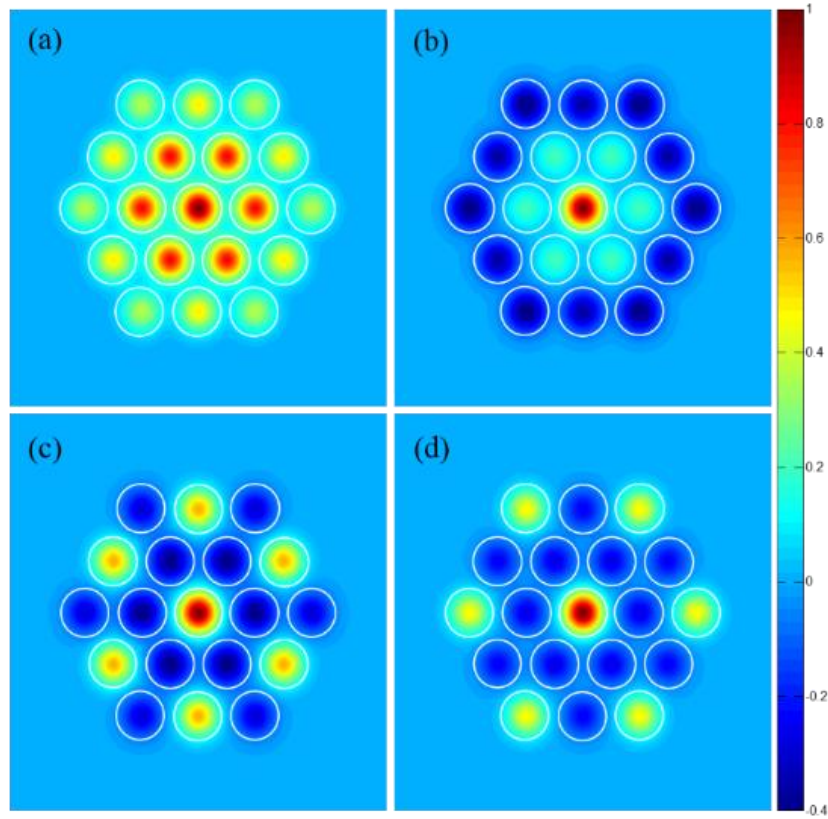
Figure 7-3 Real part of the modal field distributions in a 19-core lattice, associated with (a) the DS01 (b) DS02 (c) DS03 (d) DS04 supermodes.

We next consider supermodes involving angular momentum. In this respect, the modal fields in the outer ring vary according to $u_n = Be^{i\lambda Z}e^{iQn}$. In addition, we assume that the field in the central element is zero ($u_0 = 0$). In this case

$$i\frac{du_n}{dZ} + u_{n+1} + u_{n-1} = 0 \qquad (118)$$

Given that any solution of this latter equation must repeat itself after six elements, (e.g. $6Q = 2/\pi$), then upon substitution of u_n in Eq. (118) we deduce that

$$\lambda = 2\cos(Q) \qquad (119)$$

where $Q = l\pi/3$ and the angular momentum index takes values from the set $l = 1,2,\dots,5$. This eigenvalue relation (Eq. (119)) can now provide the remaining five supermodes DS_{l1}. Note that for the form assumed, $\sum_{n=1}^{6} u_n = 0$ which is consistent with the assumption that the DS_{lm} fields are zero at the center ($u_0 = 0$) when l is finite. Figure 7-3(b) illustrate the field profile of the DS_{11} supermode.

This same principle can now be applied to other honeycomb lattices having more rings. As a next example we consider a 19-element honeycomb double ring structure as shown in Figure 7-3(a). Given the topology of this configuration, the elements involved are now classified in four groups denoted as $a.b,c$, and $d-$ illustrated with different colors. As in the previous section, because of the hexagonal geometry, all waveguides interact only with their nearest neighbors with a coupling strength κ. Higher order interactions are here ignored since the coupling coefficient tends to exponentially decrease with distance. We now look for in-phase supermodes with $l = 0$. In this situation, the corresponding evolution equations for the modal fields, for these four groups, read as follows:

$$i\frac{d}{dZ}\begin{bmatrix} u_a \\ u_b \\ u_c \\ u_d \end{bmatrix} + \begin{bmatrix} 0 & 6 & 0 & 0 \\ 1 & 2 & 1 & 2 \\ 0 & 1 & 0 & 2 \\ 0 & 2 & 2 & 0 \end{bmatrix}\begin{bmatrix} u_a \\ u_b \\ u_c \\ u_d \end{bmatrix} = 0 \qquad (120)$$

Again, the in-phase eigenvalue problem can be obtained using the eigenvectors $u_{a,b,c,d} = u^0_{a,b,c,d}e^{i\lambda Z}$ from where we find that $\lambda^4 - 15\lambda^2 - 2\lambda^3 + 24 = 0$. The four roots of this algebraic equation are given by $[\lambda_1 = 4.8715, \ \lambda_2 = 1.2267, \ \lambda_3 = -1.6215, \ \lambda_4 = -2.4767]$ and correspond to the $DS_{01}, DS_{02}, DS_{03}$ and DS_{04} in-phase supermodes. Having found the eigenvalues, the corresponding eigenvectors $u^0_a, u^0_b, u^0_c, u^0_d$ can be evaluated from the matrix of Eq. (120). Figure 7-3 depicts the real part of modal field profile of the DS_{0m} supermodes. The remaining 15 modes are only possible if the angular momentum l is finite. In this case, again the field in the central element is zero ($u_a = 0$). In view of the b, c, and d groups assigned, Figure 7-2 (b) suggests that:

$$i\dot{u}_{b_n} + u_{b_{n+1}} + u_{b_{n-1}} + u_{c_n} + u_{d_n} + u_{d_{n-1}} = 0$$

$$i\dot{u}_{c_n} + u_{b_n} + u_{d_n} + u_{d_{n-1}} = 0$$

$$i\dot{u}_{d_n} + u_{b_n} + u_{b_{n+1}} + u_{c_n} + u_{c_{n+1}} = 0$$

$$(121)$$

where $\dot{u}_{b_n} = du_{bn}/dZ$, etc. By employing the ansatz $[u_{b_n}, u_{c_n}, u_{d_n}] = [u^0_{b_n}, u^0_{c_n}, u^0_{d_n}]e^{iQn}e^{i\lambda z}$ in equation (121), we arrive at $\lambda^3 - 2\lambda^2\cos(Q) - \lambda[4\cos(Q) + 5] - 4\sin^2(Q) = 0$. Again, periodicity demands that $Q = l\pi/3$ where l is $l = 1,2,...,5$. The three eigenvalues obtained from this cubic equation are tabulated in Table 7-1 for each angular momentum l. In this way the remaining 15 supermodes can be generated through the corresponding eigenvectors of the matrix of Eq.(121) . As an example, the real part of field profiles of modes DS_{11}, DS_{21}, and DS_{31} are shown in Figure 7-4 (a) (b) (c).

Table 7-1 The list of eigenvalues obtained from the cubic equation for the modes with angular momentum

Q	Eigenvalues
1	$\lambda = 3.354, -0.476, -1.877$
2	$\lambda = \sqrt{3}, 1, -\sqrt{3}$
3	$\lambda = -1 + \sqrt{2}, 0, -1 - \sqrt{2}$
4	$\lambda = \sqrt{3}, 1, -\sqrt{3}$
5	$\lambda = 3.354, -0.476, -1.877$

Other variations of these hexagonal lattices can also be investigated using this method. For example, let us consider again the 19-site configuration when this time the central waveguide is now completely removed. Using the same grouping outlined above, the in-phase modes satisfy

$$i \frac{d}{dz} \begin{bmatrix} u_b \\ u_c \\ u_d \end{bmatrix} + \begin{bmatrix} 2 & 1 & 2 \\ 1 & 0 & 2 \\ 2 & 2 & 0 \end{bmatrix} \begin{bmatrix} u_b \\ u_c \\ u_d \end{bmatrix} = 0 \quad (122)$$

and hence the eigenvalue equation is given by $\lambda^3 - 2\lambda^2 - 9\lambda = 0$, having three roots $\lambda = -2.1623, 0, 4.1623$.
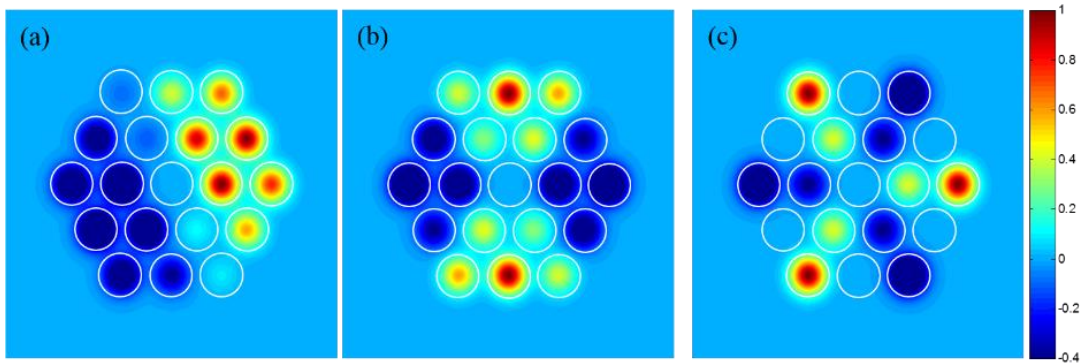
Figure 7-4 Real part of the modal field distributions in a 19-core lattice, associated with supermodes having angular momenta (a) DS$_{11}$ (b) DS$_{21}$ and (c) DS$_{31}$ mode.

One can show that the remaining 15 modes (DS_{lm}) of this 18-site arrangement are identical to those obtained for the 19-site lattice when $l = 1, 2, \dots, 5$.

As a final example, we investigate a 37 (three layer) hexagonal lattice consisting of single-mode waveguides as shown in Figure 7-5 (a). Because of their topology, the elements are now grouped in 7 families (a, b, c, d, e, f and g) as illustrated with different colors in Figure 7-5 (a). Assuming in-phase modes, we find

$$
i\frac{d}{dz}\begin{bmatrix} u_a \\ u_b \\ u_c \\ u_d \\ u_e \\ u_f \\ u_g \end{bmatrix} + \begin{bmatrix} 0 & 6 & 0 & 0 & 0 & 0 & 0 \\ 1 & 2 & 1 & 2 & 0 & 0 & 0 \\ 0 & 1 & 0 & 2 & 1 & 1 & 1 \\ 0 & 2 & 2 & 0 & 0 & 1 & 1 \\ 0 & 0 & 1 & 0 & 0 & 1 & 1 \\ 0 & 0 & 1 & 1 & 1 & 0 & 1 \\ 0 & 0 & 1 & 1 & 1 & 1 & 0 \end{bmatrix}\begin{bmatrix} u_a \\ u_b \\ u_c \\ u_d \\ u_e \\ u_f \\ u_g \end{bmatrix} = 0 \tag{123}
$$

Seven supermodes DS_{0m} can then be obtained from the resulting algebraic eigenvalue equation $\lambda^7 - 2\lambda^6 - 23\lambda^5 - 2\lambda^4 + 124\lambda^3 + 164\lambda^2 + 46\lambda - 12 = 0$. The seven roots of this latter equation are given by $\lambda = 5.3492, 2.9752, 0.1594, -0.9524, -1.0000, -1.8567, -2.6748$. As before, the remaining 30 supermodes exhibit angular momentum. These can be determined from the field evolution equations.

$$
i\dot{u}_{b_n} + u_{b_{n+1}} + u_{b_{n-1}} + u_{c_n} + u_{d_n} + u_{d_{n-1}} = 0
$$

$$
i\dot{u}_{c_n} + u_{b_n} + u_{d_n} + u_{d_{n-1}} + u_{e_n} + u_{f_n} + u_{g_{n-1}} = 0
$$

$$
i\dot{u}_{d_n} + u_{b_n} + u_{b_{n+1}} + u_{c_n} + u_{c_{n+1}} + u_{f_n} + u_{g_n} = 0
$$

$$
i\dot{u}_{e_n} + u_{c_n} + u_{f_n} + u_{g_{n-1}} = 0
$$

$$
i\dot{u}_{f_n} + u_{c_n} + u_{d_n} + u_{e_n} + u_{g_n} = 0
$$

$$
i\dot{u}_{g_n} + u_{c_{n+1}} + u_{d_n} + u_{f_n} + u_{e_{n+1}} = 0
$$

$$
\tag{124}
$$

By employing the ansatz $u_{x_n} = u_{x_n}^0 e^{i\lambda Z} e^{iQn}$ we find

$$\lambda^6 - 2\lambda^5 \cos(Q) - \lambda^4(4\cos(Q) + 13) + \lambda^3(4\cos^2(Q) + 8\cos(Q) - 14)$$

$$+ \lambda^2(16\cos^2(Q) + 18\cos(Q) + 18) + \lambda(6\cos(2Q)$$

$$+ 20\cos^2(Q) + 8\cos(Q) + 22)$$

$$+ (8\cos(2Q) + 8\cos^2(Q) + 4\cos(Q) - 4\cos(2Q)\cos(Q)) = 0$$
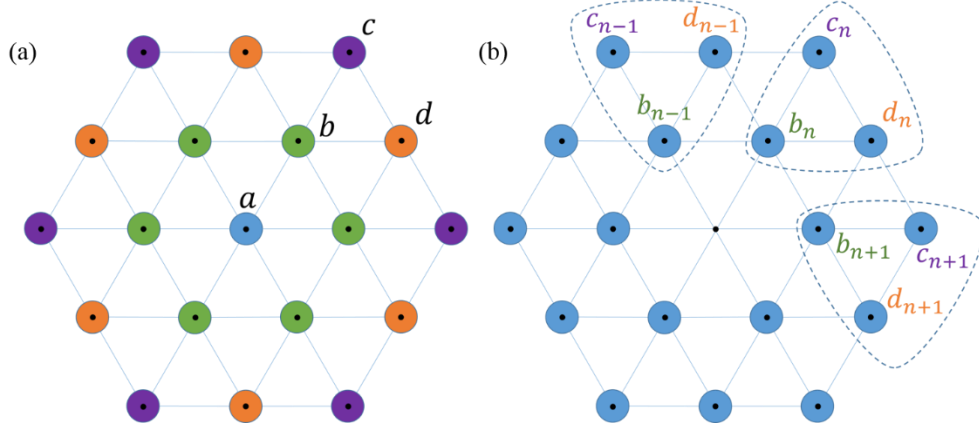
(125)
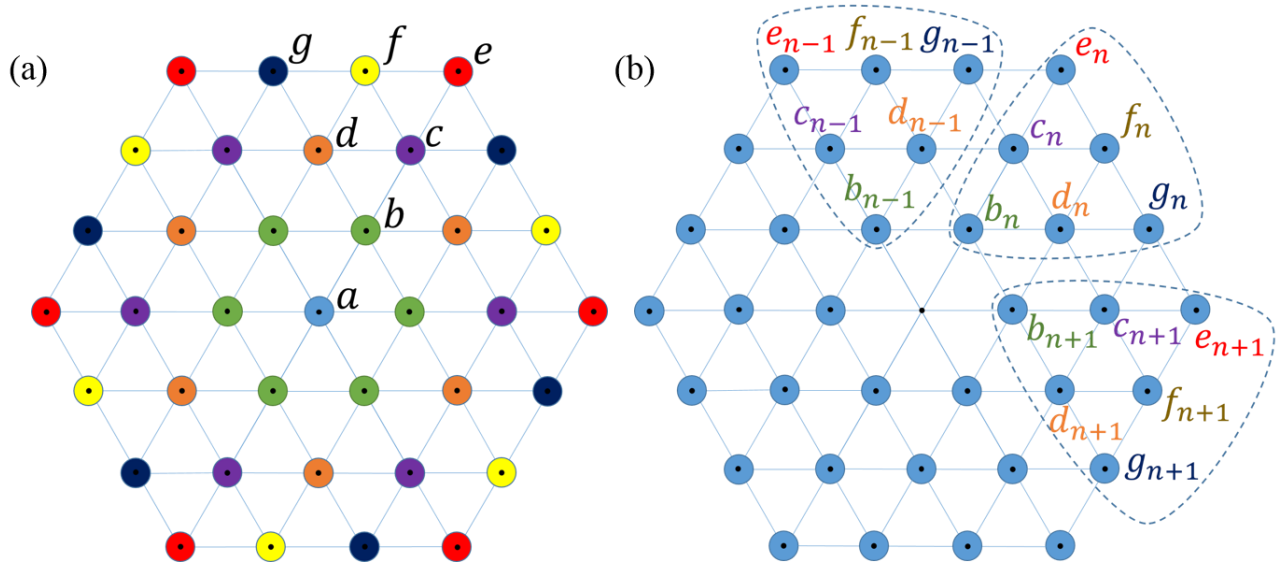
Figure 7-5 (a) 37-core hexagonal lattice. The waveguide elements are now grouped in 7 different families (a, b, c, d, e, f, g) indicated with different colors. (b) By excluding the central core, the remaining elements of these families are grouped in each hexagonal sector in order to obtain all the supermodes with angular momenta.

where $Q = l\pi/3$ with $l = 1,2, \dots ,5$. The 6×5 eigenvalues of these DS_{lm} supermodes (carrying angular momentum) can be directly obtained from Eq. (125) along with their eigenvectors. The real part of modal field profiles of the DS_{03}, DS_{04}, DS_{21}, DS_{23}, DS_{32} and DS_{35} is depicted in Figure 7-6 Real part of the modal field distributions in a 37-core lattice, associated with supermodes (a Finally the eigenvalue distributions and degeneracies of a 7-, 19-, 37-core lattice are provided for comparison in Figure 7-7 we would like to note that in all cases our results (based

on coupled-mode theory) are in excellent agreement with finite element simulations based on weakly guiding structures. The method described here can be used in a similar fashion to analyze any other multi-ring hexagonal lattice. For example, in the case of a 61-core hexagonal lattice (involving four layers), the grouping of the elements will lead to 11 in-phase DS_{0m} supermodes (whose eigenvalues are obtained from a 11th order polynomial) while 10×5 DS_{lm} supermodes with angular momentum can result from a 10th order polynomial involving $Q = l\pi/3$ where $l = 1, 2, \dots, 5$.
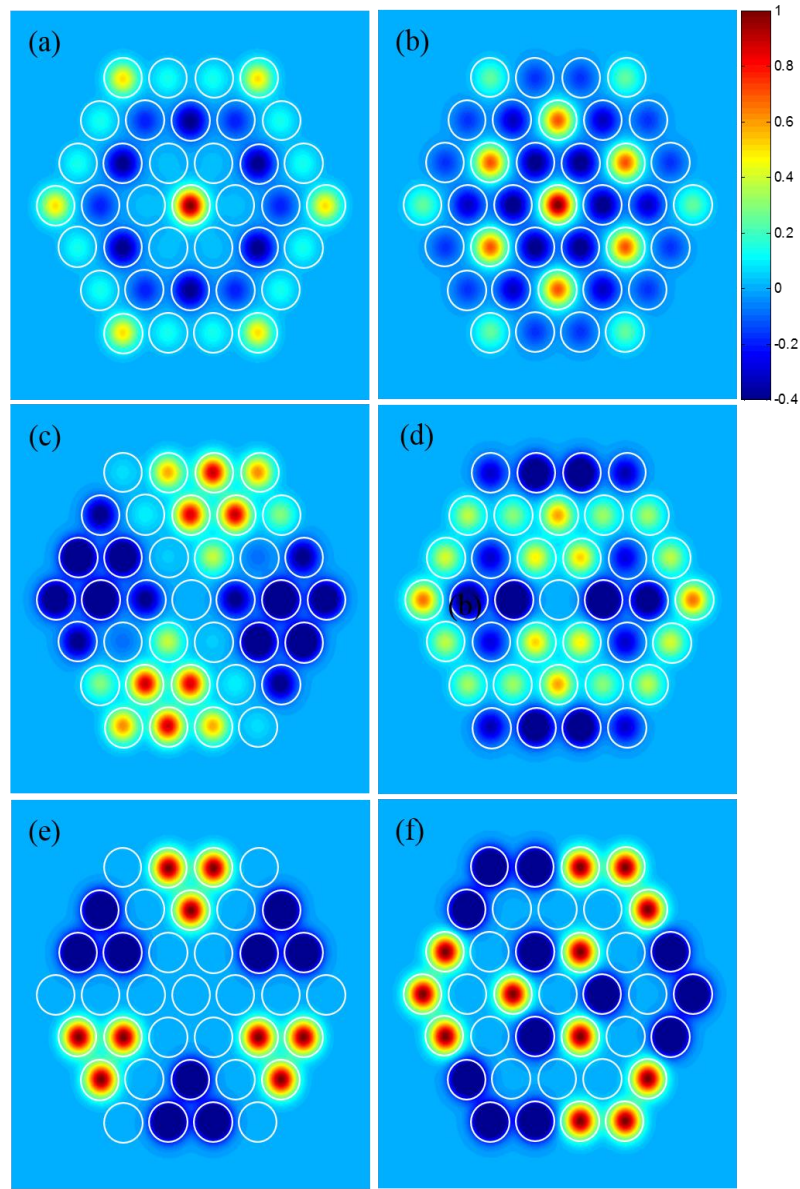
Figure 7-6 Real part of the modal field distributions in a 37-core lattice, associated with supermodes (a) DS_{03} (b) DS_{04} (c) DS_{21} (d) DS_{23} (e) DS_{32} (f) DS_{35}.
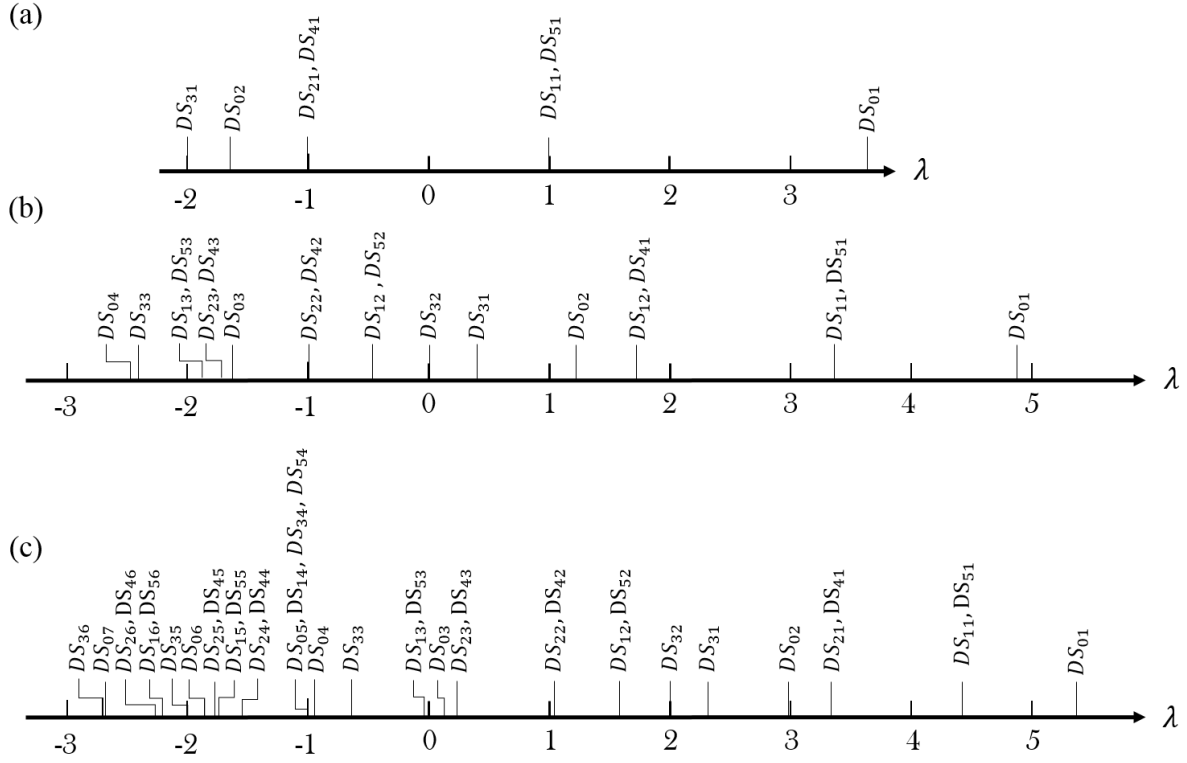
Figure 7-7 Eigenvalue distribution diagrams for (a) a 7-core (b) 19-core and (c) 37-core hexagonal lattice.

CHAPTER 8: MULTI-CORE STRUCTURES WITH EQUI-SPACED EIGENVALUES

8.1 Introduction

As it was discussed in the previous chapter, multi-core fiber structures are of great importance to us due to their potential to go beyond the data carrying capacity of single-mode fiber systems. In multi-core settings, the data carrying channels are the system supermodes rather than waveguide modes. Each supermode has a specific propagation constant and group velocity. A rather large modal dispersion is inherent to these structures due to the difference between the group velocities of supermodes. This intermodal group velocity dispersion is one of the limiting factors that compromises the data bandwidth. An ideal system will have zero differential group delay (DGD) and hence maximum data bandwidth. Here, we put forward a practical strategy to alleviate high DGD problem in the multi-core structures.
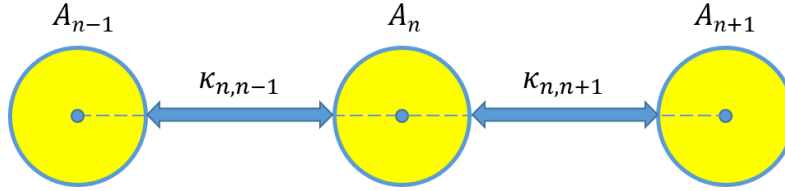
Figure 8-1 Three elements of a fiber array with their field amplitudes and inter-waveguide coupling coefficients.

Shemirani in [23] shows that in the presence of adequate coupling among the modes of a multimode structure, the system DGD scales proportional to $\sqrt{L}$ rather than L where L is the propagation distance. But in a multicore structure of arbitrary size, the eigenvalues are not distributed equidistantly from each other and therefore coupling all the modes to each other is not easily possible and by introducing a single perturbation one cannot couple all the modes to each other. Our aim here is to design a lattice of multi-core fibers similar with eigenvalues spaced

equally from each other. The advantage that this system offers is that through introducing a single coupling, all the modes can be coupled. Multimode fibers with a parabolic index offer such characteristics, however, since the highest-order mode lies near the continuum, a coupling term results in a large loss.

To design a one-dimensional linear multicore structure with equidistant eigenvalues, two strategies can be exploited. First considering the coupling or equivalently the spacing between elements as a variable. Second, considering the core to core spacings and coupling to be constant and consider the propagation constants (core radii) as the design variables.

First, we consider a 1D structure with identical waveguides and the spacing between elements can be altered. In this case, the system is described through a coupled-mode theory as below:

$$i\frac{dA_n}{dz} + \kappa_{n,n+1}A_{n+1} + \kappa_{n,n-1}A_{n-1} = 0 \qquad (126)$$

$$A_n = a_n e^{i\lambda z} \qquad (127)$$

where a_n is constant and accounts for the initial amplitude.

$$-\lambda a_n + \kappa_{n,n+1}a_{n+1} + \kappa_{n,n-1}a_{n-1} = 0 \qquad (128)$$

$$[a_n] = [a_0 \ a_1 \ a_2 \ a_3 \ a_4 \ ... \ a_N]$$

$$\begin{bmatrix} -\lambda & \kappa_{1,0} & 0 & 0 & 0 & \vdots & 0 \\ \kappa_{0,1} & -\lambda & \kappa_{2,1} & 0 & 0 & \vdots & 0 \\ 0 & \kappa_{1,2} & -\lambda & \kappa_{3,2} & 0 & \vdots & 0 \\ 0 & 0 & \kappa_{2,3} & -\lambda & \kappa_{4,3} & \vdots & 0 \\ 0 & 0 & 0 & \kappa_{3,4} & -\lambda & \vdots & 0 \\ 0 & 0 & 0 & 0 & \kappa_{4,5} & \vdots & \kappa_{N,N-1} \\ 0 & 0 & 0 & 0 & 0 & \vdots & -\lambda \end{bmatrix} \begin{bmatrix} a_0 \\ a_1 \\ a_2 \\ a_3 \\ a_4 \\ \vdots \\ a_N \end{bmatrix} = 0 \qquad (129)$$

From the physical symmetry $\kappa_{n,m} = \kappa_{m,n}$

$$
\begin{bmatrix}
-\lambda & \kappa_{1,0} & 0 & 0 & 0 & \vdots & 0 \\
\kappa_{1,0} & -\lambda & \kappa_{2,1} & 0 & 0 & \vdots & 0 \\
0 & \kappa_{2,1} & -\lambda & \kappa_{3,2} & 0 & \vdots & 0 \\
0 & 0 & \kappa_{3,2} & -\lambda & \kappa_{4,3} & \vdots & 0 \\
0 & 0 & 0 & \kappa_{4,3} & -\lambda & \vdots & 0 \\
0 & 0 & 0 & 0 & \kappa_{4,5} & \vdots & \kappa_{N,N-1} \\
0 & 0 & 0 & 0 & 0 & \vdots & -\lambda
\end{bmatrix}
\begin{bmatrix}
a_0 \\ a_1 \\ a_2 \\ a_3 \\ a_4 \\ \vdots \\ a_N
\end{bmatrix} = 0
\qquad (130)
$$

To have a non-trivial solution the determinant of the matrix above must be zero. This gives an equation of order N. Given the N desired eigenvalues, this equation needs to be solved to find the unknown coupling coefficients $\kappa_{m,n}$.

$$
\lambda^N + \sum_{n=0}^{N-1} \lambda^n f_n(\kappa_{1,0}, \kappa_{2,1}, \dots, \kappa_{N,N-1}) = 0
\qquad (131)
$$

To simplify the calculations, the equation can be normalized.

$$
i\frac{dA_n}{dz} + \kappa_{n,n+1} A_{n+1} + \kappa_{n,n-1} A_{n-1} = 0
\qquad (132)
$$

$z = \xi/Z$, where Z is the normalization factor

$$
i\frac{dA_n}{d\xi} + c_{n,n+1} A_{n+1} + c_{n,n-1} A_{n-1} = 0
\qquad (133)
$$

$$
c_{n,n+1} = \frac{\kappa_{n,n+1}}{Z}
\qquad (134)
$$

The second approach, as it was mentioned before is through using dissimilar waveguide elements. Again from the coupled-mode theory, one can represent the governing equations for such structure as below:

$$
i\frac{dA_n}{dz} + \kappa(A_{n+1} + A_{n-1}) + \delta_n A_n = 0
\qquad (135)
$$

Note that the coupling between waveguides is considered to be identical. Since the coupling is not critically dependent on the core radii of elements, this approximation is not expected to introduce significant error.

$$
A_n = a_n e^{i\lambda z}
\qquad (136)
$$

where a_n is constant and accounts for the initial amplitude

$$-\lambda a_n + \kappa(a_{n+1} + a_{n-1}) + \delta_n a_n = 0 \tag{137}$$

$$[a_n] = [a_1\ a_2\ a_3\ a_4\ \dots\ a_N]$$

$$\begin{bmatrix} -\lambda + \delta_1 & \kappa & 0 & 0 & 0 & \vdots & 0 \\ \kappa & -\lambda + \delta_2 & \kappa & 0 & 0 & \vdots & 0 \\ 0 & \kappa & -\lambda + \delta_3 & \kappa & 0 & \vdots & 0 \\ 0 & 0 & \kappa & -\lambda + \delta_4 & \kappa & \vdots & 0 \\ 0 & 0 & 0 & \kappa & -\lambda + \delta_5 & \vdots & 0 \\ 0 & 0 & 0 & 0 & \kappa & \vdots & \kappa \\ 0 & 0 & 0 & 0 & 0 & \vdots & -\lambda + \delta_N \end{bmatrix} \begin{bmatrix} a_1 \\ a_2 \\ a_3 \\ a_4 \\ \vdots \\ a_N \end{bmatrix} = 0 \tag{138}$$

To have a non-trivial solution the determinant of the matrix above must be zero. Again, this gives an equation of order N. Given the N desired eigenvalues, this equation is solved to find the unknown core detuning $\delta_{m,n}$.

$$\lambda^N + \sum_{n=0}^{N-1} \lambda^n f_n(k; \delta_1, \delta_2, \dots, \delta_N) = 0 \tag{139}$$

κ in the equation above is considered to be known. This equation can be normalized to simplify the computations.

$$i\frac{dA_n}{dz} + \kappa(A_{n+1} + A_{n-1}) + \delta_n A_n = 0 \tag{140}$$

$z = \xi/Z$, where Z is the normalization parameter

$$i\frac{dA_n}{d\xi} + c(A_{n+1} + A_{n-1}) + \Delta_n A_n = 0 \tag{141}$$

$$\Delta_n = \frac{\delta_n}{Z}, c = \frac{\kappa}{Z} \tag{142}$$

To inversely design a lattice from the desired eigenvalues Hochstadt theorem can be utilized.

8.2 Hochstadt Theorem:

This theorem is used to build a matrix from its eigenvalues. To make the matrix, first N desired eigenvalues are chosen (λ_n). Then N-1 arbitrary auxiliary values μ_n are chosen such that value of

each auxiliary value μ_n lies between two eigenvalues; i.e. $\lambda_1 < \mu_1 < \lambda_2$. Since these values are known, there will be two polynomials as below:

$$p_N(\lambda) = \prod_{n=1}^{N}(\lambda_n - \lambda), \tag{143}$$

$$p_{N-1}(\lambda) = \prod_{n=1}^{N-1}(\mu_n - \lambda), \tag{144}$$

By expanding the two above expressions, the following polynomials are obtained:

$$P_n = x^n + \alpha_{n-1}x^{n-1} + \cdots + \alpha_0 \tag{145}$$

$$P_{n-1} = x^{n-1} + \beta_{n-2}x^{n-2} + \cdots + \beta_0 \tag{146}$$

All the α and β coefficients are known and from these values, all the unknown coefficients of the next polynomial can be easily found

$$P_{n-2} = x^{n-2} + \gamma_{n-3}x^{n-3} + \cdots + \gamma_0 \tag{147}$$

$$a = \alpha_{n-1} - \beta_{n-2}$$

$$c = a\beta_{n-2} + \beta_{n-3} - \alpha_{n-2}$$

$$\gamma_i = \frac{a\beta_i + \beta_{i-1} - \alpha_i}{c}$$

$$i = n - 3, \dots, 1$$

$$\gamma_0 = \frac{a\beta_0 - \alpha_0}{c}$$

$$\tag{148}$$

In the above relations, a is directly related to δ, the required propagation constants of each individual element, and c is the inter-element coupling coefficient. By choosing μ to be at the midpoint of each interval, the detuning can be made zero and all the cores can be made to be the same size, i.e. $\delta_n = 0$. The lattice with desired eigenvalues is designed by adjusting the inter-element spacings.

As an example, this method above was exploited to design a linear structure containing five elements.

8.3 A Linear Array with Equidistant Eigenvalue Distribution

Here, the purpose is to design a lattice with a self-imaging characteristic. For such a system, eigenvalues must be equispaced. Based on the Hochstad theorem, if the second set of points which must interlace with the first set is chosen such that they lie exactly in the middle of the interval between two eigenvalues then all the detuning terms δs are going to be 0.

The following arbitrarily equispaced eigenvalues were chosen to design an example system with five elements.

$$\lambda = [-2.8 \quad -1.4 \quad 0 \quad 1.4 \quad 2.8]$$

$$\mu = [-2.1 \quad -0.7 \quad 0.7 \quad 2.1]$$

From Hochstadt theorem, the four coupling coefficients among 5 elements are calculated to be as below:

$$\kappa_1 = 0.98995, \quad \kappa_2 = 1.30958, \quad \kappa_3 = 1.48492, \quad \kappa_4 = 2.21359$$

Having the normalized coupling coefficients and given certain design specifications, one can find the actual inter-core coupling value.

$$-\Lambda a_n + c_{n,n+1} a_{n+1} + c_{n,n-1} a_{n-1} = 0 \tag{149}$$

Choosing the normalization factor to be $Z = 100$, the couplings will be as below:

$$c_1 = 98.9949, c_2 = 130.9580, c_3 = 148.4924, c_4 = 221.3594$$

The following parameters are considered for our considered design:

$$\Delta = 0.003$$

$$n_1 = 1.4489$$

$$\lambda = 1.5 \times 10^{-6}$$

$$a = 4.0 \; \mu m$$

Now, the spacing d_n between every two waveguides should be adjusted such that it gives the aforementioned denormalized coupling values.

Table 8-1 Four coupling terms between 5 elements of the 1-D linear lattice and the equivalent inter-waveguide spacings.

n	c_n	$d \; (\mu m)$	ERROR
1	98.995	17.63	0.1605
2	130.9375	16.75	0.02105
3	148.4925	16.35	0.14425
4	221.3595	15.10	0.05225

An array of five waveguides was constructed according to the values given in Table 8-1 and was numerically studied. To this end, we used COMSOL Multiphysics software. The eigenvalues associated with the supermodes are plotted in Figure 8-2. In this figure, the black line is a straight line given as a reference for comparison.
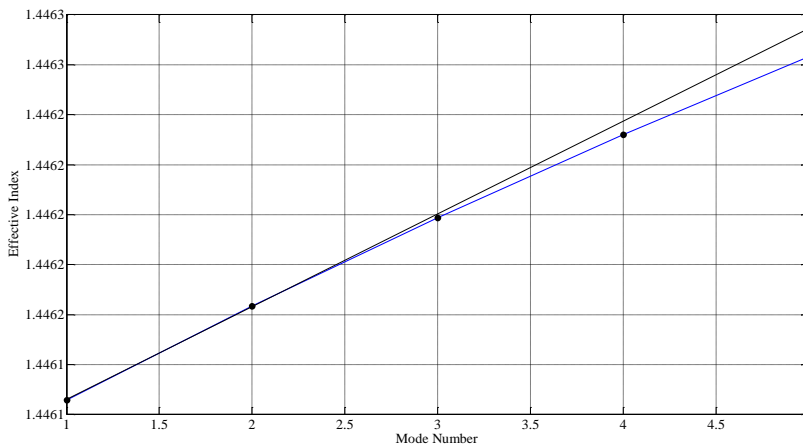
Figure 8-2 Distribution of eigenvalues corresponding to an array of identical waveguides and engineered inter-waveguide spacings (blue curve). The black line a straight line given as a reference.

Comparing this designed structure with a similar lattice but with uniform inter-component spacing (Figure 8-3) reveals a more linear distribution.
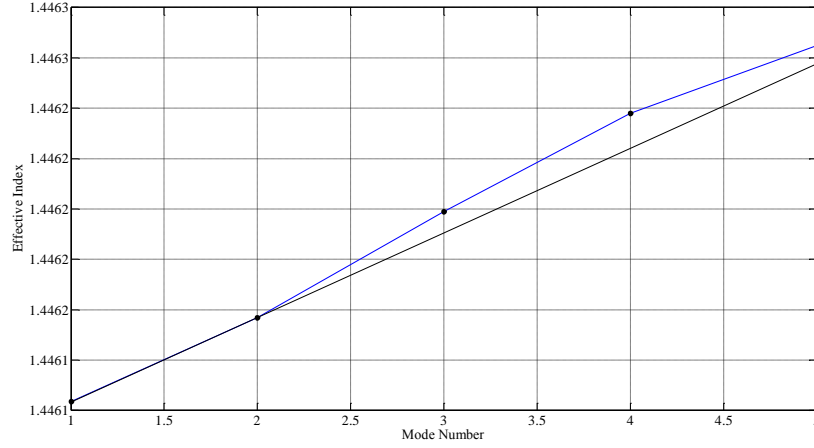
Figure 8-3 Distribution of eigenvalues corresponding to an array of identical waveguides distributed uniformly (spacing d = 16 µm).

In our designed structure, the difference in the propagation constants are computed as below

$$\Delta\beta_1 = 156.6607, \Delta\beta_2 = 148.5638, \Delta\beta_3 = 138.7872, \Delta\beta_4 = 131.3772$$

While for the equidistant case we had

$$\Delta\beta_1 = 139.4281, \Delta\beta_2 = 176.7711, \Delta\beta_3 = 163.3921, \Delta\beta_4 = 112.5193$$

The alternative to this design is a five-core lattice designed using the second scheme, having different core radii but with equal spacings. For this design, the characteristic polynomial of the matrix, calculated from Hochstadt theorem, was used to solve for the modifications required in the core radii. The following values were obtained after some mathematical manipulations.

$$\Delta_1 = 0, \quad \Delta_2 = 0.0972, \quad \Delta_3 = 0.4615, \quad \Delta_4 = 1.9861, \quad \Delta_5 = -2.545$$

$$\kappa = 1.05808848466682$$

To find the actual detuning values, given from our design specifications, we use a denormalization factor to scale the normalized coupling coefficients into physical values. The parameter Z (denormalization factor) is considered to be 156.9937 for a spacing of 16 μm.

$$Z = 156.993673333776$$

$$d = 16 \ \mu m$$

Considering this denormalization factor the detuning values will be as:

$$\delta_1 = 0, \delta_2 = 15.2679, \delta_3 = 72.4471, \delta_4 = 311.8137, \delta_5 = -399.5287,$$

$$\Delta n_{eff} = \frac{\lambda_0 \delta}{2\pi}$$

$$\Delta n_{eff_1} = 0, \Delta n_{eff_2} = 3.6449e - 6, \Delta n_{eff_3} = 1.7295e - 5, \Delta n_{eff_4} = 7.4440e - 5, \Delta n_{eff_5}$$

$$= -9.5380e - 05$$

Now, each detuning value is mapped into a change in the core diameters of individual elements.

Table 8-2 the offset values in the propagation constants, the equivalent core radii and the error introduced to a limited precision in determining the core radii values for our engineered design.

n	$\beta + \delta_n$	$r \ (\mu m)$	Error
1	1.4461984848	4	0
2	1.4462021297	4.005	$1.2878786993e - 07$
3	1.4462157803	4.024	$4.1792631000e - 07$
4	1.4462729248	4.107	$1.7560460996e - 07$
5	1.4461031043	3.868	$1.6276894987e - 07$
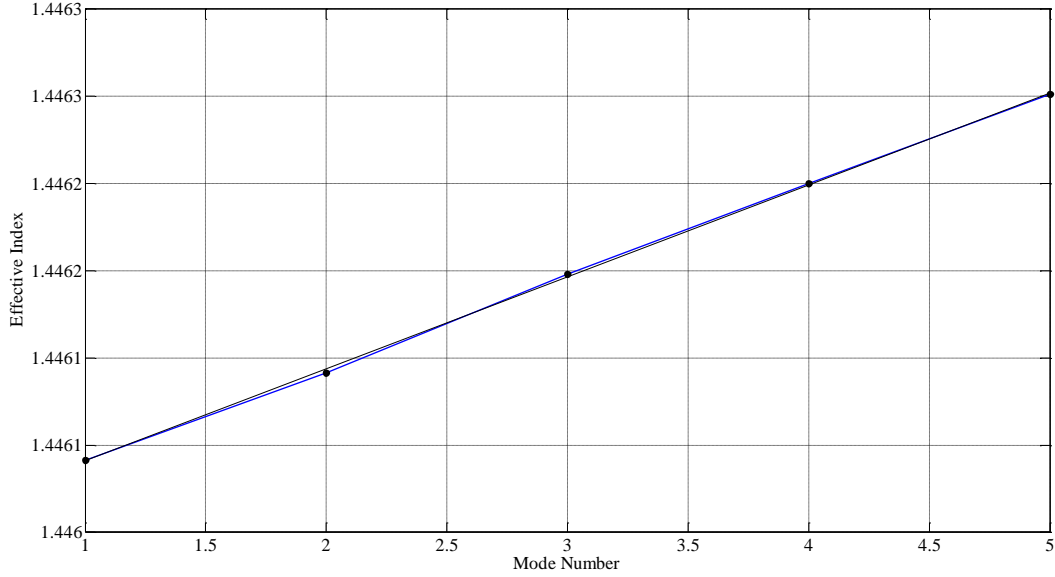
Figure 8-4 The linear distribution of eigenvalues for our designed 5-element linear array (blue curve). The black cure is a straight line given as a reference.

Comparing the two schemes reveals that the second scheme, which uses the detunings as the design parameters (instead of inter-core distance), is a much more robust method. The superiority of the second scheme comes from the fact that a multicore array structure has smaller sensitivities to changes in core radii in compare with the inter-waveguide element distance. A slight change in the spacing between the waveguide elements can significantly alter the coupling value. Therefore, due to this sensitivity, achieving the ideal design values and even fine tuning the distance between elements is very difficult. The difference among propagation eigenvalues obtained from the second scheme is given in the lines below:

$$\Delta\lambda_{12} = 5.006800e - 05, \Delta\lambda_{23} = 5.667000e - 05, \Delta\lambda_{34} = 5.213200e - 05, \Delta\lambda_{45} = 5.108700e - 05$$
$$\Delta\beta_{12} = 209.724348, \Delta\beta_{23} = 237.378741, \Delta\beta_{34} = 218.370011, \Delta\beta_{45} = 213.992725$$

8.4 2-D Multicore Structures with Equidistant Eigenvalue Distribution

Next, we intend to design a 2D rectangular lattice possessing a uniform distribution of eigenvalues. Designing a 2D lattice with arbitrary eigenvalues using the first scheme due to is impossible. The

reason is that, in 2-D structures, each element is surrounded by other elements and this limits the degree of freedom required to adjust the inter-element spacing. Therefore, the second scheme is exploited for our purpose. The governing equation for a 2-D multicore structure with common coupling coefficient but different core radii values is represented as below

$$i \frac{da_{m,n}}{dz} + \kappa \left(a_{m+1,n} + a_{m-1,n} + a_{m,n+1} + a_{m,n-1} \right) + \gamma_{n,m} a_{n,m} = 0 \qquad (150)$$

If the core radii considered to be the same the couplings to be different then:

$$i \frac{da_{m,n}}{dz} + \left(\kappa_{m+1,m;n} a_{m+1,n} + \kappa_{m-1,m;n} a_{m-1,n} + \kappa_{m;n,n+1} a_{m,n+1} + \kappa_{m;n,n-1} a_{m,n-1} \right) +$$

$$\gamma_{n,m} a_{n,m} = 0 \qquad (151)$$

Assuming a separable solution of the form below and its substitution in Eq. (151) greatly simplifies our analysis.

$$a_{m,n} = U_n V_m$$

$$i \frac{dU_n V_m}{dz} + \left(\kappa_{m+1,m;n} U_n V_{m+1} + \kappa_{m-1,m;n} U_n V_{m-1} + \kappa_{m;n,n+1} U_{n+1} V_m + \right.$$

$$\kappa_{m;n,n-1} U_{n-1} V_m) + \gamma_{n,m} U_n V_m = 0 \qquad (152)$$

$$iV_m \frac{dU_n}{dz} + iU_n \frac{dV_m}{dz} + \left(\kappa_{m+1,m;n} U_n V_{m+1} + \kappa_{m-1,m;n} U_n V_{m-1} + \kappa_{m;n,n+1} U_{n+1} V_m + \right.$$

$$\kappa_{m;n,n-1} U_{n-1} V_m) + \gamma_{n,m} U_n V_m = 0 \qquad (153)$$

By dividing both sides by $U_n V_m$ one gets:
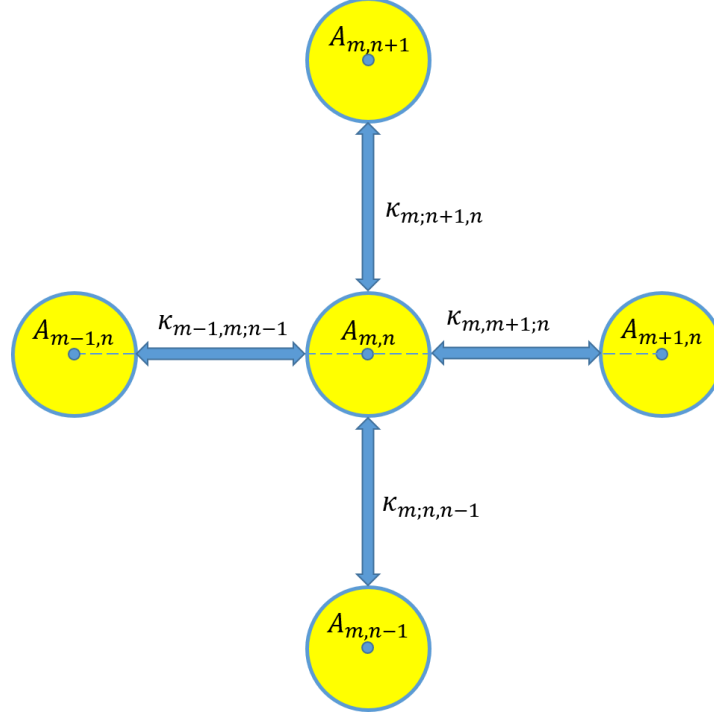
Figure 8-5 A two dimensional lattice of waveguides. The effect of cross-coupling terms is ignored here.

$$\frac{i}{U_n}\frac{dU_n}{dz} + \frac{i}{V_m}\frac{dV_m}{dz} + \left(\kappa_{m+1,m;n}\frac{V_{m+1}}{V_m} + \kappa_{m-1,m;n}\frac{V_{m-1}}{V_m} + \kappa_{m;n,n+1}\frac{U_{n+1}}{U_n} + \kappa_{m;n,n-1}\frac{U_{n-1}}{U_n}\right) + \gamma_{n,m} = 0$$

$$(154)$$

That can be decomposed in to two similar equations (155) and (156)

$$\frac{i}{U_n}\frac{dU_n}{dz} + \left(\kappa_{m;n,n+1}\frac{U_{n+1}}{U_n} + \kappa_{m;n,n-1}\frac{U_{n-1}}{U_n}\right) + \delta_{u;m,n} = 0 \qquad (155)$$

$$\frac{i}{V_m}\frac{dV_m}{dz} + \left(\kappa_{m+1,m;n}\frac{V_{m+1}}{V_m} + \kappa_{m-1,m;n}\frac{V_{m-1}}{V_m}\right) + \delta_{v;m,n} = 0 \qquad (156)$$

$$\delta_{u;m,n} + \delta_{v;m,n} = \gamma_{m,n} \qquad (157)$$

Equations (155) and (156) can be reformulated as below

$$i\frac{dU_n}{dz} + \left(\kappa_{m;n,n+1}U_{n+1} + \kappa_{m;n,n-1}U_{n-1}\right) + \delta_{u;m,n}U_n = 0 \qquad (158)$$

$$i\frac{dV_m}{dz} + \left(\kappa_{m+1,m;n}V_{m+1} + \kappa_{m-1,m;n}V_{m-1}\right) + \delta_{v;m,n}V_m = 0 \qquad (159)$$

$$\delta_{u;m,n} + \delta_{v;m,n} = \gamma_{m,n} \qquad (160)$$

$$U_n = u_n e^{i\lambda_u z} \tag{161}$$

$$V_m = v_m e^{i\lambda_v z} \tag{162}$$

where u_n and v_n are constant quantities.

$$-\lambda_u u_n + \left(\kappa_{m;n,n+1} u_{n+1} + \kappa_{m;n,n-1} u_{n-1}\right) + \delta_{u;m,n} u_n = 0 \tag{163}$$

$$-\lambda_v v_m + \left(\kappa_{m+1,m;n} v_{m+1} + \kappa_{m-1,m;n} v_{m-1}\right) + \delta_{v;m,n} v_m = 0 \tag{164}$$

$$\delta_{u;n,m} + \delta_{v;n,m} = \gamma_{m,n} \tag{165}$$

$$
\begin{bmatrix}
-\lambda_u + \delta_{u;m,1} & \kappa_{m;1,2} & 0 & 0 & 0 & \vdots & 0 \\
\kappa_{m;1,2} & -\lambda_u + \delta_{u;m,2} & \kappa_{m;2,3} & 0 & 0 & \vdots & 0 \\
0 & \kappa_{m;2,3} & -\lambda_u + \delta_{u;m,3} & \kappa_{m;3,4} & 0 & \vdots & 0 \\
0 & 0 & \kappa_{m;3,4} & -\lambda_u + \delta_{u;m,4} & \kappa_{m;4,5} & \vdots & 0 \\
0 & 0 & 0 & \kappa_{m;4,5} & -\lambda_u + \delta_{u;m,5} & \vdots & 0 \\
0 & 0 & 0 & 0 & \kappa_{m;5,6} & \vdots & \kappa_{m;N-1,N} \\
0 & 0 & 0 & 0 & 0 & \vdots & -\lambda_u + \delta_{u;m,N}
\end{bmatrix}
\begin{bmatrix}
u_1 \\ u_2 \\ u_3 \\ u_4 \\ \vdots \\ u_N
\end{bmatrix} =
$$

$$0 \tag{166}$$

$$
\begin{bmatrix}
-\lambda_v + \delta_{v;1,n} & \kappa_{1,2;n} & 0 & 0 & 0 & \vdots & 0 \\
\kappa_{1,2;n} & -\lambda_v + \delta_{v;2,n} & \kappa_{2,3;n} & 0 & 0 & \vdots & 0 \\
0 & \kappa_{2,3;n} & -\lambda_v + \delta_{v;3,n} & \kappa_{3,4;n} & 0 & \vdots & 0 \\
0 & 0 & \kappa_{3,4;n} & -\lambda_v + \delta_{v;4,n} & \kappa_{4,5;n} & \vdots & 0 \\
0 & 0 & 0 & \kappa_{4,5;n} & -\lambda_v + \delta_{v;5,n} & \vdots & 0 \\
0 & 0 & 0 & 0 & \kappa_{5,6;n} & \vdots & \kappa_{M-1,M;n} \\
0 & 0 & 0 & 0 & 0 & \vdots & -\lambda_v + \delta_{v;M,n}
\end{bmatrix}
\begin{bmatrix}
v_1 \\ v_2 \\ v_3 \\ v_4 \\ \vdots \\ v_M
\end{bmatrix} =
$$

$$0 \tag{167}$$

considering all the coupling terms to be equal one simply arrives at the following equations.

$$i\frac{da_{m,n}}{dz} + \kappa\left(a_{m+1,n} + a_{m-1,n} + a_{m,n+1} + a_{m,n-1}\right) + \gamma_{n,m} a_{n,m} = 0 \tag{168}$$

$$a_{m,n} = U_n V_m \tag{169}$$

$$U_n = u_n e^{i\lambda_u z} \tag{170}$$

$$V_m = v_m e^{i\lambda_v z} \tag{171}$$

$$-\lambda_u u_n + \kappa(u_{n+1} + u_{n-1}) + \delta_{u;m,n} u_n = 0 \tag{172}$$

$$-\lambda_v v_m + \kappa(v_{m+1} + v_{m-1}) + \delta_{v;m,n} v_m = 0 \tag{173}$$

$$\delta_{u;n,m} + \delta_{v;n,m} = \gamma_{m,n} \qquad\qquad (174)$$

8.4.1 Example Design: A Five by Five Rectangular Lattice

According to the design procedure described in the previous section, to design a two dimensional lattice of waveguides with uniformly distributed eigenvalues, the detuning terms should be appropriately chosen. For a sample design specification given before ($\Delta = 0.003$, $n_1 = 1.4489$, $\lambda = 1.5 \times 10^{-6}$, $a = 4.0\ \mu m$) the design parameters are found as given in Table 8-3.

Table 8-3 Each cell of this table shows propagation constant detuning from a reference value

	1	2	3	4	5
1	$\Delta_{1x} + \Delta_{1y}$	$\Delta_{1x} + \Delta_{2y}$	$\Delta_{1x} + \Delta_{3y}$	$\Delta_{1x} + \Delta_{4y}$	$\Delta_{1x} + \Delta_{5y}$
2	$\Delta_{2x} + \Delta_{1y}$	$\Delta_{2x} + \Delta_{2y}$	$\Delta_{2x} + \Delta_{3y}$	$\Delta_{2x} + \Delta_{4y}$	$\Delta_{2x} + \Delta_{5y}$
3	$\Delta_{3x} + \Delta_{1y}$	$\Delta_{3x} + \Delta_{2y}$	$\Delta_{3x} + \Delta_{3y}$	$\Delta_{3x} + \Delta_{4y}$	$\Delta_{3x} + \Delta_{5y}$
4	$\Delta_{4x} + \Delta_{1y}$	$\Delta_{4x} + \Delta_{2y}$	$\Delta_{4x} + \Delta_{3y}$	$\Delta_{4x} + \Delta_{4y}$	$\Delta_{4x} + \Delta_{5y}$
5	$\Delta_{5x} + \Delta_{1y}$	$\Delta_{5x} + \Delta_{2y}$	$\Delta_{5x} + \Delta_{3y}$	$\Delta_{5x} + \Delta_{4y}$	$\Delta_{5x} + \Delta_{5y}$

Table 8-4 Given our design specification, the core radii values are computed.

	1	2	3	4	5
1	4	4.005	4.024	4.107	3.868
2	4.005	4.010	4.030	4.112	3.872
3	4.024	4.030	4.049	4.132	3.891
4	4.107	4.112	4.132	4.217	3.971
5	3.868	3.872	3.891	3.971	3.740

Again, to corroborate our design, the system under consideration was simulated in COMSOL Multiphysics software and the associated propagation eigenvalues were found and plotted in Figure 8-6.
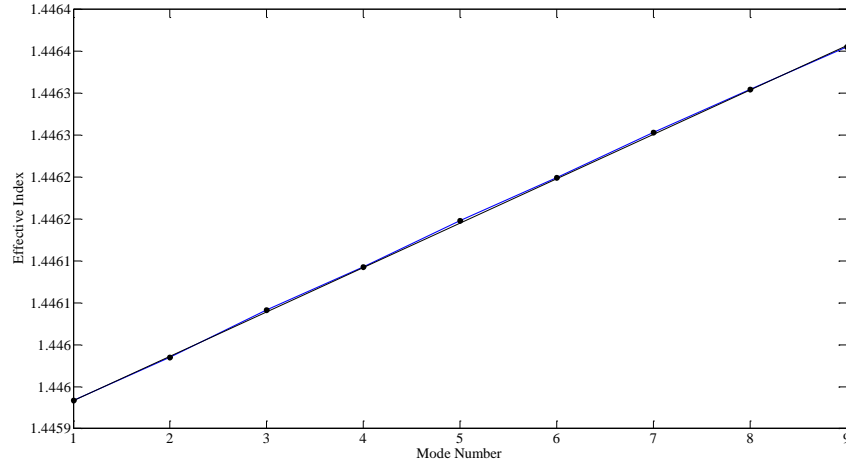
Figure 8-6 The linear distribution of eigenvalues for a designed two-dimensional system of 5 by 5 elements.

As it is clear from Figure 8-6, the eigenvalues are lying on a straight line and the intended linear behavior is achieved. The differences between eigenvalues corresponding to consecutive states are given below:

$$\Delta\beta_{12} = 215.953079007682$$
$$\Delta\beta_{23} = 237.889773309647$$
$$\Delta\beta_{34} = 215.358270798683$$
$$\Delta\beta_{45} = 230.622222304797$$
$$\Delta\beta_{56} = 215.320571687441$$
$$\Delta\beta_{67} = 224.933845206668$$
$$\Delta\beta_{78} = 216.221161580648$$
$$\Delta\beta_{89} = 212.413551284757$$

We expected to see 25 distinct supermodes, but as it is clear, the system is full of degeneracies and there exist only 9 distinct eigenvalues. The number of degenerate states for each eigenmode is shown in Figure 8-7.
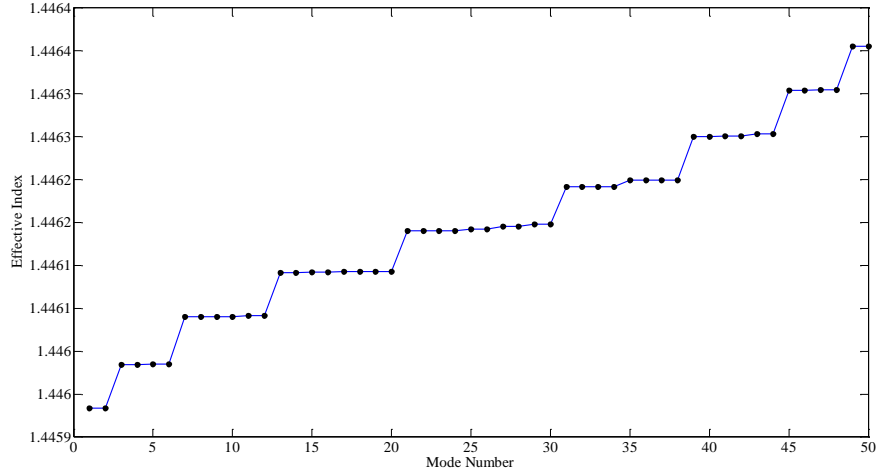
Figure 8-7 Distribution of 50 eigenvalues of an engineered 5 by 5 lattice. Evidently, there are many degeneracies in the system.

8.5 Seven-Element Hexagonal Lattice with Equi-spaced Eigenvalues

One of the most popular multicore structures is a 7-core hexagonal multicore setting. Its popularity mainly arises from the ease of fabrication this geometry offers. Here, we intend to design a 7-core hexagonal multicore structure with an equidistant distribution of eigenvalue. The coupling equations for such a lattice considering identical elements of the same core radius is given in Eq. (175):
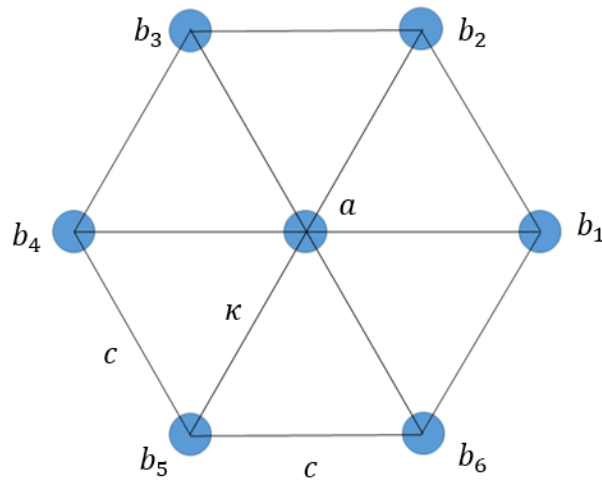
Figure 8-8 A 7-element hexagonal lattice. All seven elements are identical.

If all the elements are identical then $c = \kappa$. Then the normalized coupling equations are as blow:

$$i\frac{da}{dz} + b_1 + b_2 + b_3 + b_4 + b_5 + b_6 = 0$$

$$i\frac{db_1}{dz} + b_2 + b_6 + a = 0$$

$$i\frac{db_2}{dz} + b_1 + b_3 + a = 0$$

$$i\frac{db_3}{dz} + b_2 + b_4 + a = 0$$

$$i\frac{db_4}{dz} + b_3 + b_5 + a = 0$$

$$i\frac{db_5}{dz} + b_4 + b_6 + a = 0$$

$$(175)$$

The matrix representation of Eq. (175) is as below:

$$\begin{bmatrix} -\lambda & 1 & 1 & 1 & 1 & 1 & 1 \\ 1 & -\lambda & 1 & 0 & 0 & 0 & 1 \\ 1 & 1 & -\lambda & 1 & 0 & 0 & 0 \\ 1 & 0 & 1 & -\lambda & 1 & 0 & 0 \\ 1 & 0 & 0 & 1 & -\lambda & 1 & 0 \\ 1 & 0 & 0 & 0 & 1 & -\lambda & 1 \\ 1 & 1 & 0 & 0 & 0 & 1 & -\lambda \end{bmatrix} \begin{bmatrix} a \\ b_1 \\ b_2 \\ b_3 \\ b_4 \\ b_5 \\ b_6 \end{bmatrix} = 0 \qquad (176)$$

To find the eigenvalues, one needs to solve the following equation.

$$Av = \lambda v \qquad (177)$$

$$A = \begin{bmatrix} 0 & 1 & 1 & 1 & 1 & 1 & 1 \\ 1 & 0 & 1 & 0 & 0 & 0 & 1 \\ 1 & 1 & 0 & 1 & 0 & 0 & 0 \\ 1 & 0 & 1 & 0 & 1 & 0 & 0 \\ 1 & 0 & 0 & 1 & 0 & 1 & 0 \\ 1 & 0 & 0 & 0 & 1 & 0 & 1 \\ 1 & 1 & 0 & 0 & 0 & 1 & 0 \end{bmatrix} \qquad (178)$$

The eigenvalues of this configuration do not lie on a ladder. To achieve such a design, again we use the fiber core radii as the design variables. Considering detuning in the design, the coupling equations after normalization are as below:

$$i\frac{da}{d\xi} + b_1 + b_2 + b_3 + b_4 + b_5 + b_6 + \Delta_1 a = 0$$

$$i\frac{db_1}{d\xi} + b_2 + b_6 + a + \Delta_2 b_1 = 0$$

$$i\frac{db_2}{d\xi} + b_1 + b_3 + a + \Delta_3 b_2 = 0$$

$$i\frac{db_3}{d\xi} + b_2 + b_4 + a + \Delta_4 b_3 = 0$$

$$i\frac{db_4}{d\xi} + b_3 + b_5 + a + \Delta_5 b_4 = 0$$

$$i\frac{db_5}{d\xi} + b_4 + b_6 + a + \Delta_6 b_5 = 0$$

$$i\frac{db_6}{d\xi} + b_5 + b_1 + a + \Delta_7 b_6 = 0$$

(179)

Where the following normalization parameters were used:

$$\Delta_n = \frac{\delta_n}{\kappa}$$

(180)

$$\xi = \kappa z$$

(181)

$$A = \begin{bmatrix} \Delta_1 & 1 & 1 & 1 & 1 & 1 & 1 \\ 1 & \Delta_2 & 1 & 0 & 0 & 0 & 1 \\ 1 & 1 & \Delta_3 & 1 & 0 & 0 & 0 \\ 1 & 0 & 1 & \Delta_4 & 1 & 0 & 0 \\ 1 & 0 & 0 & 1 & \Delta_5 & 1 & 0 \\ 1 & 0 & 0 & 0 & 1 & \Delta_6 & 1 \\ 1 & 1 & 0 & 0 & 0 & 1 & \Delta_7 \end{bmatrix}$$

(182)

From Hochstadt theorem and performing some matrix conversion techniques, the proper Δs are calculated and represented as below:

$$\Delta_1 = -2.35811, \Delta_2 = 0.18432, \Delta_3 = -0.13201, \Delta_4 = 0.65139, \Delta_5 = 3.09043, \Delta_6 = -3.38838, \Delta_7 = 1.95237$$

To realize a design based on these parameters, we need to choose a design specification to scale all the values and make them physically meaningful. The design is done base on the following specifications:

$$\lambda = 1.5 \ \mu m$$

$$\Delta = 0.003$$

$$n_1 = 1.4489$$

$$n_2 = 1.4446$$

$$\rho = a = 4.0 \ \mu m$$

$$V = 1.88$$

Figure 8-9 The components of a 7-element hexagonal lattice and their assigned numbers.

For a spacing distance of $12\,\mu m$ between the waveguides, the coupling will be calculated theoretically as below:

$$d = 12\,\mu m \quad c_{theory} = 602.74739364553$$

A satisfactory coupling constant scales the detuning δs to values that fall within our fabrication precision.

$$\Delta_n = \frac{\delta_n}{\kappa}$$

$$\kappa = 602.74739364553$$

Table 8-5 The computed radius size for elements of a hexagonal multicore structure, having a linear eigenvalue distribution

n	r_n	Error
1	3.548	$4.77831e-08$
2	4.038	$1.97881e-07$
3	3.973	$2.53315e-07$
4	4.135	$2.04754e-08$
5	4.695	$1.81088e-07$
6	3.364	$3.90447e-07$
7	4.422	$3.03942e-07$
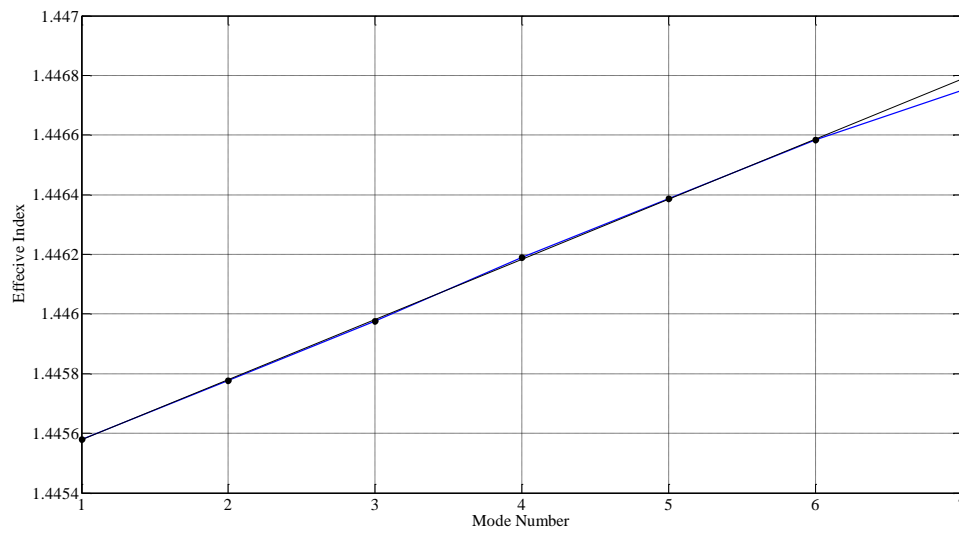
Figure 8-10 The eigenvalue distribution of the designed 7-element hexagonal structure

The field profile corresponding to the largest eigenvalue is shown in Figure 8-11. From this figure, one can see that by tweaking the fifth element (hosting most of the field energy in Figure 8-11) the eigenvalues distribution can be tuned to be more linear. A manual tuning reveals that by increasing the core radius of the fifth element to 4.8 μm the largest eigenvalue can be pushed up resulting to a very linear distribution of eigenvalues, as can be seen in Figure 8-12).
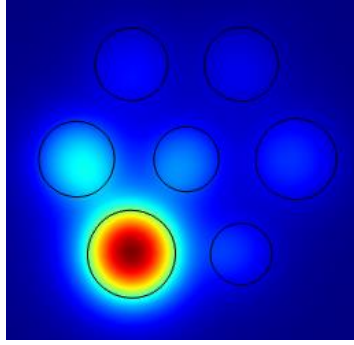
Figure 8-11 Field distribution of the mode with the largest eigenvalue.
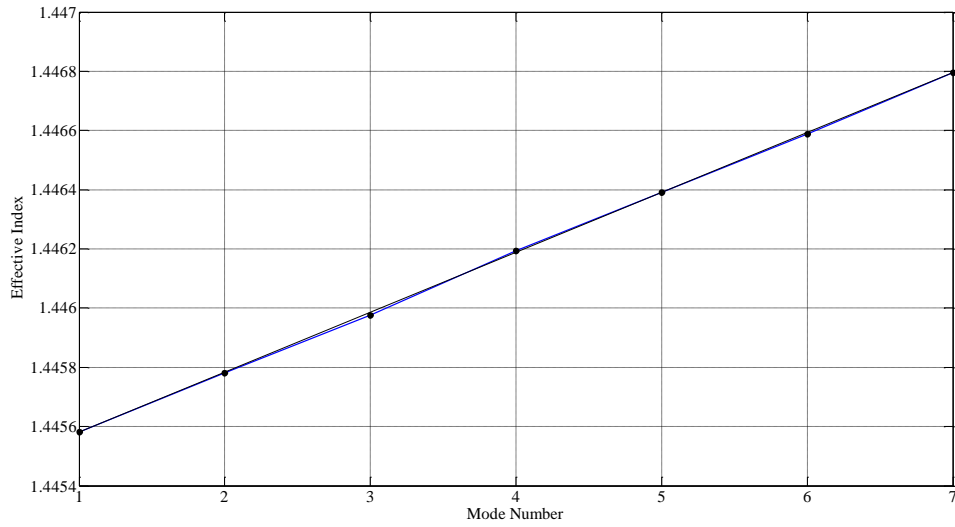
Figure 8-12 The linear eigenvalue distribution of the designed 7-element hexagonal structure after tweaking the fifth element

For this optimized design, the differences between consecutive eigenvalues are given as below:

$\Delta\beta_{12} = 837.94235$, $\Delta\beta_{23} = 818.81633$, $\Delta\beta_{34} = 906.05626$, $\Delta\beta_{45} = 832.08642$, $\Delta\beta_{56} = 827.55415$, $\Delta\beta_{67} = 867.10052$

8.6 Six-Element Pentagonal Lattice with Equi-spaced Eigenvalues

As it was mentioned before, by introducing an intermodal coupling, the intermodal group delay is greatly suppressed and the information bandwidth is enhanced. A grating coupler is usually used to couple modes to each other. Multicore fiber structures are usually contrasted with multimode fibers. Multimode fiber structures are economic options that can be used for information transmission. However, for all index distributions except parabolic-index profile, the eigenvalues do not lie uniformly away from each other. Using graded-index multimode fibers gives the advantage of having equidistant eigenvalues in addition to a minimal DGD. Thus the spatial modes of a graded-index MMF can be easily coupled by a single grating. However, due to the proximity of the higher-order modes to the cladding modes, a huge loss is introduced as a result of a flow of energy from bound modes to continuum. An alternative way is to do this DGD compensation process in certain periodically repeating stations outside an MMF where these problems are avoided. Photonic lanterns transform the modes of a multimode structure into supermodes of a multicore system and vice-versa. Here, we consider a multimode fiber with 6 modes (including degenerate modes and mode groups).

The multimode fiber that is the main medium to transfer information after a certain distance is gradually tapered into an equidistant multicore fiber. Through this process, every mode of the structure is coupled losslessly to a supermode of the MCF structure. Now, by introducing a simple grating, one can easily couple all the modes within the multicore section, hence, minimizing the walk-off effects. In the next stage, the modes are again coupled back into the multimode fiber. This process is repeated periodically and through this DGD is greatly mitigated.

However, to realize such a structure, the first step is designing a 6-core MCF. To simplify the fabrication process, a pentagonal geometry is considered. Figure 8-13 demonstrates a schematic of such a design.
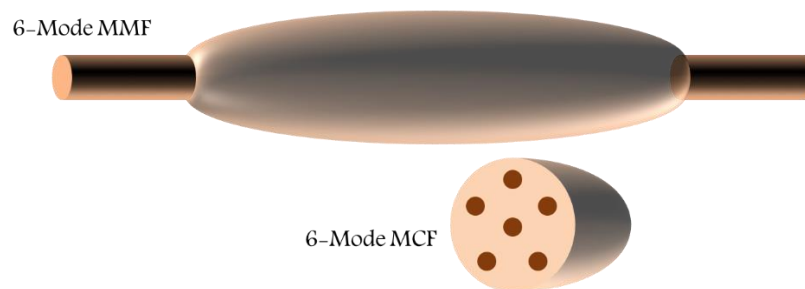
Figure 8-13 The 6-core multimode fiber is tapered into an equidistant multicore fiber structures, where all the modes are strongly coupled to each other and thus DGD is mitigated.

The first step is determining the design specifications including the core and cladding index, the starting point core-diameter, the spacing between cores that determines the coupling strength and also deviations from the starting core diameter design.

The considerations for a good design are

1- Variations of core diameters across the design should be as low as possible, to meet one of the fundamental assumptions: inter-core coupling is assumed to be independent of core-diameter variations.

2- The eigenvalues must be far from cladding to minimize any power leakage.

3- The cores should be as close as possible to allow for maximum coupling and supermodal overlaps.

4- While still meeting the conditions 1-3, the core-diameter variations should be large enough for an ease of fabrication.

It is clear from the above conditions that the design parameters should be carefully chosen to be practical.

Silica has a refractive index of $n_c = 1.444$ at telecom wavelength. We consider the core to have a refractive index $n_g < 1.46$ to stay single-mode for moderate core variations. The design is made around the central core radius of $4\ \mu m$. We do not expect the core radii size exceeded $4.5\ \mu m$ and we expect them to still stay single mode even for this core size.

- For single mode performance, the V-number should be below 2.405.

- We consider core to have a refractive index of 1.45 and the cladding to be 1.444 ($\Delta = 6 \times 10^{-3}$)

- The maximum radius size for single mode operation is $4.5\ \mu m$.

8.6.1 Calculation of Coupling Coefficients

In our design parameters, the fiber has a core radius of $4\ \mu m$, with a core index of 1.444 and the cladding index of 1.45. The structure as shown in Figure 8-14 is a pentagon.
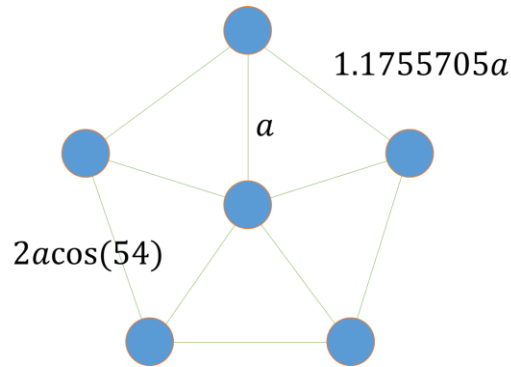
Figure 8-14 The 6-core pentagonal structure

It is very important to first determine the inter-core spacing first. Since for this specific geometry, the entire design is highly dependent on the spacing. The coupling factor is calculated from the relation below:

$$c = \sqrt{2\Delta} \frac{u^2 K_0\left(\frac{wD}{a}\right)}{K_1(w)^2 a \, V^3} \qquad (\,183\,)$$

D_1: Distance from central element to the circumferential cores

D_2: Distance between circumferential cores.

$$D_2 = 1.17557 \times D_1$$

The propagation constant (based on COMSOL simulations) is:

$$n_e = 1.44675066462022$$

$$\beta = k_0 n_e$$

8.6.2 Pentagonal Lattice: The First Design

We consider the spacing between the central core to the lateral elements to be $12\ \mu m$. And the fiber core radius to have a core radius of $a = 4\ \mu m$. We first calculate the coupling between the central element the peripheral ones.

$$n_{e1} = 1.44573898965622$$

$$n_{e2} = 1.44548981680895$$

$$\kappa = \frac{\beta_2 - \beta_1}{2} = \frac{k_0}{2}(n_{e1} - n_{e2})$$

$$\kappa = 505.0319912628847$$

The coupling between the central core and the peripheral ones is:

$$n_{e1} = 1.44568438808379$$

$$n_{e2} = 1.44555659355294$$

$$\kappa = \frac{\beta_2 - \beta_1}{2} = \frac{k_0}{2}(n_{e1} - n_{e2})$$

$$\kappa = 259.0183$$

The ratio between two coupling values is an important design parameter.

$$C = \frac{C_{l-l}}{C_{c-l}} = 0.512875027315939$$

The equations describing this structure are as below:

$$\frac{i\partial u_1}{\partial z} + c_1(u_2 + u_3 + u_4 + u_5 + u_6) + \delta_1 u_1 = 0$$

$$\frac{i\partial u_2}{\partial z} + c_1 u_1 + c_2(u_3 + u_6) + \delta_2 u_2 = 0$$

$$\frac{i\partial u_3}{\partial z} + c_1 u_1 + c_2(u_2 + u_4) + \delta_3 u_3 = 0$$

$$\frac{i\partial u_4}{\partial z} + c_1 u_1 + c_2(u_3 + u_5) + \delta_4 u_4 = 0$$

$$\frac{i\partial u_5}{\partial z} + c_1 u_1 + c_2(u_4 + u_6) + \delta_5 u_5 = 0$$

$$\frac{\partial u_6}{\partial z} + c_1 u_1 + c_2(u_2 + u_5) + \delta_6 u_6 = 0$$

(184)

The above equations are obtained after applying the gauge transform $U(z) = u(z)\, e^{-i\beta z}$.

$$\frac{i\partial u_1}{\partial Z} + (u_2 + u_3 + u_4 + u_5 + u_6) + \Delta_1 u_1 = 0$$

$$\frac{i\partial u_2}{\partial Z} + u_1 + C(u_3 + u_6) + \Delta_2 u_2 = 0$$

$$\frac{i\partial u_3}{\partial Z} + u_1 + C(u_2 + u_4) + \Delta_3 u_3 = 0$$

$$\frac{i\partial u_4}{\partial Z} + u_1 + C(u_3 + u_5) + \Delta_4 u_4 = 0$$

$$\frac{i\partial u_5}{\partial Z} + u_1 + C(u_4 + u_6) + \Delta_5 u_5 = 0$$

$$\frac{\partial u_6}{\partial Z} + u_1 + C(u_2 + u_5) + \Delta_6 u_6 = 0$$

$$Z = c_1 z, \; C = c_2/c_1 , \; \Delta_n = \delta_n/c_1$$

$$A = \begin{bmatrix} \Delta_1 & 1 & 1 & 1 & 1 & 1 \\ 1 & \Delta_2 & C & 0 & 0 & C \\ 1 & C & \Delta_3 & C & 0 & 0 \\ 1 & 0 & C & \Delta_4 & C & 0 \\ 1 & 0 & 0 & C & \Delta_5 & C \\ 1 & C & 0 & 0 & C & \Delta_6 \end{bmatrix} \tag{185}$$

As it was previously calculated $C = 0.563698041$. Now, we need to find Δs for an equidistance eigenvalue distribution. To do this we use the following a simple Python code that can be found in the Appendix I. Using the code given in Appendix I, we find the Δ vector to be as below:

$\Delta = [\, 9.19766331 \;\; 2.12727189 \; - 9.75904369 \; - 5.86620808 \; - 1.90776241 \;\; 6.2078824 \,]$

The eigenvalues of such a matrix are:

$Eig = [\, -9.88469887 \; - 5.93104506 \; - 1.97691166 \;\; 1.97699594 \;\; 5.9309001 \;\; 9.88456535 \,]$

Which are well equispaced. The difference between each two consecutive eigenvalues is as below:

$Diff(Eig)$

$= [3.953653810000000 \;\; 3.954133400000000 \;\; 3.953907600000000 \;\; 3.953904160000000$

$3.953665250000001]$

Where the difference is in the 4th precision digit. Based on the previously mentioned design specifications, the design values are denormalized. We recall that all the parameters were normalized with respect to the coupling factor ratio between the core fiber and the peripheral ones.

$$Z = c_1 z, \quad C = c_2/c_1, \quad \Delta_n = \delta_n/c_1$$

$$z = \frac{Z}{c_1}$$

$$c_2 = c_1 C$$

$$\delta_n = c_1 \Delta_n$$

And $c_1 = 505.0319912628847$. The actual detuning values are calculated as below:

$$\delta_n = 1000 * [4.645114216414875 \quad 1.074340358564260 \quad -4.928629267582189$$

$$-2.962622747804824 \quad -0.963481048778780 \quad 3.135179209997816]$$

Next, we find the core radius values, corresponding to these detuning values. The notation δ_n here is a difference of propagation constant from a reference value. In other words, $\beta_n - \beta_0 = \delta_n$, where β_ns are propagation constants of every isolated core. For a fiber with the following characteristics:

$$a = 3 \ \mu m$$

$$n_{core} = 1.45$$

$$n_{clad} = 1.444$$

The propagation constant (from COMSOL simulations) is:

$$n_e = 1.44562363576262$$

$$\beta_0 = k_0 n_e$$

Below, $\beta = \beta_0 + \delta_n$ values are calculated.

$$\beta = [\ 5.850517833699154 \quad 5.854342010110604 \quad 5.858166153590339 \quad 5.861990792363823$$

$$5.865814226483982 \quad 5.869638238372545\ ]$$

$$n_{eff} = [1.446769539740212 \quad 1.445888664959494 \quad 1.444407791411185 \quad 1.444892785877634$$

$$1.445385954466813 \quad 1.446397053629183]$$

The above n_{eff}s are proportional to core values given in the lines below:

$$r_1 = 4.02$$
$$r_2 = 3.21$$
$$r_3 = 2.046$$
$$r_4 = 2.448$$
$$r_5 = 2.818$$
$$r_6 = 3.652$$

The error values given below are calculated form the difference between ideal propagation constants and propagation constants proportional to the above mentioned design values (core radii)

$$Error_1 = -8.283090124905357e - 08$$
$$Error_2 = 4.210045174701804e - 07$$
$$Error_3 = -7.150309551118284e - 07$$
$$Error_4 = -8.319869093664778e - 07$$
$$Error_5 = 4.222431122524739e - 07$$
$$Error_6 = -1.043126112376669e - 06$$

To obtain a perfect design, the core radii are manually tuned. These values are given in Table 8-6

Table 8-6 The computed core radii of lattice elements for a pentagonal structure with an equidistant distribution of eigenvalue.

r_1	$\mathbf{4.08\ \mu m}$
r_2	$3.21\ \mu m$
r_3	$2.07\ \mu m$
r_4	$2.45\ \mu m$
r_5	$2.82\ \mu m$
r_6	$3.65\ \mu m$

Effective indices of six modes are also given in Table 8-7.

Table 8-7 The effective indices corresponding to the design values given in Table 8-6

1.444369816000000
1.444875056000000
1.445372428000000
1.445869554000000
1.446363699000000
1.446871981000000

The spacing between effective indices of consecutive modes is given below. The error is in the 4th decimal digit. The eigenvalues of our designed structure lie very well on a straight line (Figure 8-15).

1.0e-03 *

0.505240000000073

0.497371999999885

0.497125999999959

0.494145000000001

0.508281999999971
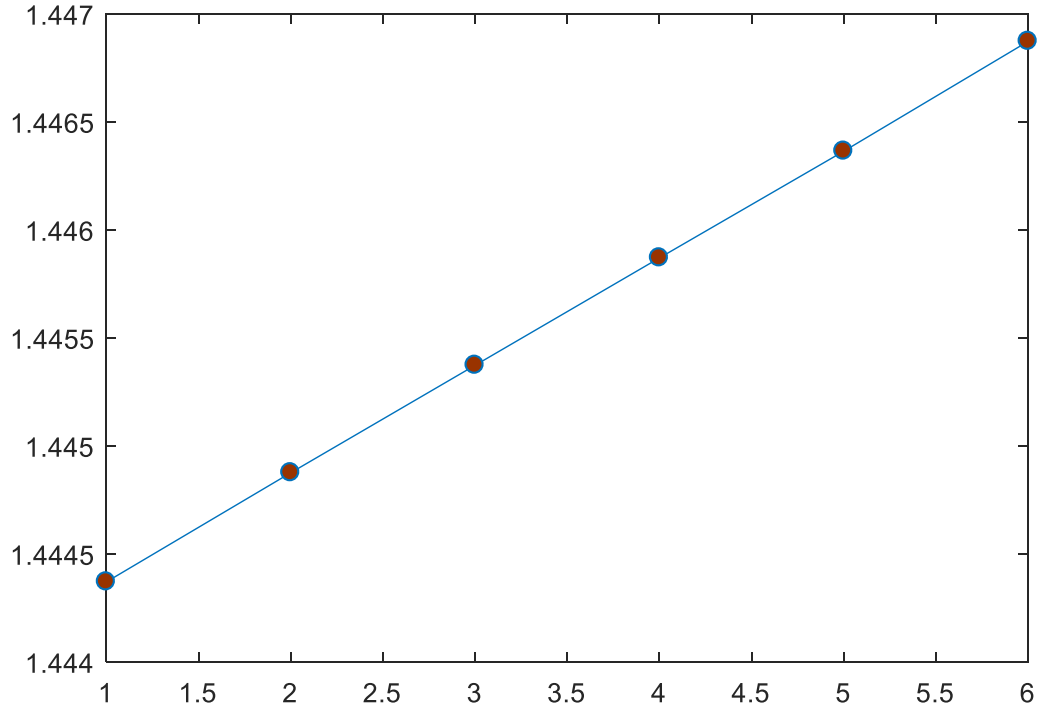
Figure 8-15 The linear distribution of eigenvalues for a pentagonal structure given in Table 8-6

8.6.3 Pentagonal Lattice: The Second Design

We consider the spacing to be $12\ \mu m$ from the central core to the lateral elements.

$$a = 12\ \mu m$$

The coupling between the central element and the peripheral ones is calculated as below:

$$n_{e1} = 1.44573898965622$$

$$n_{e2} = 1.44548981680895$$

$$\kappa = \frac{\beta_2 - \beta_1}{2} = \frac{k_0}{2}(n_{e1} - n_{e2})$$

$$\kappa = 505.0319912628847$$

The coupling between two peripheral elements is found from below:

$$n_{e1} = 1.44568438808379$$

$$n_{e2} = 1.44555659355294$$

$$\kappa = \frac{\beta_2 - \beta_1}{2} = \frac{k_0}{2}(n_{e1} - n_{e2})$$

$$\kappa = 259.0183$$

$$C = \frac{C_{l-l}}{C_{c-l}} = 0.512875027315939$$

Through the same procedure we find the Δ vector to be as below:

$$\Delta = [\, -5.80195284 \quad 1.19879854 \quad 6.38553905 \, - 1.37087941 \quad 3.73753476 \, - 4.1490221 \,]$$

The eigenvalues of such a matrix are:

$$Eig = [-6.58943748 \, - 3.95356274 \, - 1.31758142 \quad 1.31808138 \quad 3.95385456 \quad 6.58866692]$$

The differences between consecutive eigenvalues are as below:

$$\begin{aligned} Diff(Eig) \\ = \quad [2.635874740000 \quad 2.635981320000 \quad 2.635662800000 \quad 2.63577318000 \quad 2.634812360000] \end{aligned}$$

Where the difference is again in the 4th precision digit. Now, again denormalization is performed

to the actual design specifications.

$$Z = c_1 z, C = c_2/c_1 \,, \Delta_n = \delta_n/c_1$$

$$z = \frac{Z}{c_1}$$

$$c_2 = c_1 C$$

$$\delta_n = c_1 \Delta_n$$

For $c_1 = 505.0319912628847$, the physical detuning values are calculated as below:

$$\begin{aligned} \delta_n = \quad 1000 * [\, -2.930171795998549 \quad 0.605431613779239 \quad 3.224901501708409 \\ - 0.692337958213588 \quad 1.887574622257048 \, - 2.095388892956715] \end{aligned}$$

Now, we should find core radii proportional to these changes in the propagation constants. For a

fiber with the following characteristics:

$$a = 3 \, \mu m$$

$$n_{core} = 1.45$$

$$n_{clad} = 1.444$$

The propagation constant (from COMSOL simulations) is:

$$n_e = 1.44562363576262, \qquad \beta_0 = k_0 n_e$$

The vector below represents $\beta = \beta_0 + \delta_n$

$$\beta = [\, 5.850517833699154 \quad 5.854342010110604 \quad 5.858166153590339 \quad 5.861990792363823$$
$$5.865814226483982 \quad 5.869638238372545 \,]$$

And the effective indices proportional to these propagation constants are as below:

$$n_{eff} = [1.446769539740212 \quad 1.445888664959494 \quad 1.444407791411185 \quad 1.444892785877634$$
$$1.445385954466813 \quad 1.446397053629183]$$

These n_{eff}s are proportional to particular core radius values of fibers that are calculated and given

in the below:

$$r_1 = 2.454$$
$$r_2 = 3.118$$
$$r_3 = 3.672$$
$$r_4 = 2.87$$
$$r_5 = 3.378$$
$$r_6 = 2.608$$

$$Error_1 = -6.864806818551728e - 07$$
$$Error_2 = -8.968273186304998e - 07$$
$$Error_3 = -3.397280237127376e - 07$$
$$Error_4 = -1.363850628210983e - 06$$
$$Error_5 = -7.669702746238016e - 07$$
$$Error_6 = -1.540302957403483e - 06$$

In the section below, we perform the manual tuning to minimize the errors.

8.6.4 Pentagonal Lattice: Manual Tuning

After manually changing the core radii (with 10 nm precision) to reach the best performance at 1.55 μm we get the following values. For $d = 12\,\mu m$, where d is the distance from the central core to the peripheral ones.

Table 8-8 The optimized core radii values for an equidistant distribution of eigenvalues in a pentagonal multicore structure.

r_1	$2.50\,\mu m$
r_2	$3.12\,\mu m$
r_3	$3.69\,\mu m$
r_4	$2.87\,\mu m$
r_5	$3.39\,\mu m$
r_6	$2.61\,\mu m$

The location of each core is demonstrated in Figure 8-16.

$$s = 2d\cos(54°)$$
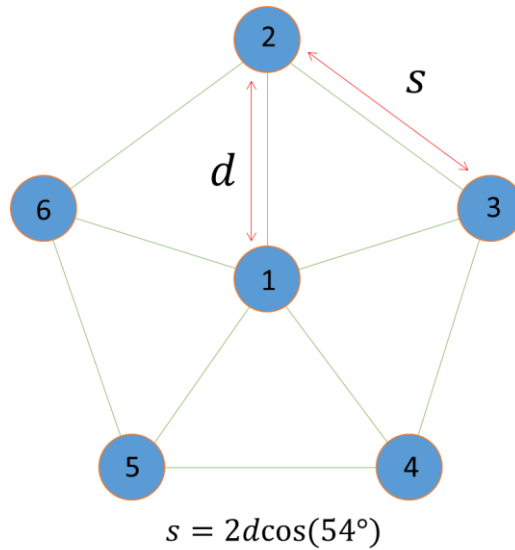
Figure 8-16 This figure shows the numbering convention that was used in the design procedure

The eigenvalues of such a structure are given in Table 8-9.

Table 8-9 The effective indices for the second design

1.444786257000000
1.445120029000000
1.445451588000000
1.445781903000000
1.446116304000000
1.446448379000000

The spacings between eigenvalues are given in Table 8-10

Table 8-10 The spacing between eigenvalues for the second design after manual tuning. Each value is normalized to 10^{-3} .

0.333771999999843
0.331559000000148
0.330315000000025
0.334400999999929
0.332074999999987

CONCLUSION AND REMARKS

Multimode fiber systems offer a promising avenue for overcoming some of the physical limitations associated with single mode structures. The added spatial degrees of freedom provide further opportunities at both the scientific and technological level that were previously overlooked and remained unattainable because of technological barriers. From a more fundamental perspective, such multidimensional multimode systems provide an ideal testbed for investigating complex linear and nonlinear modal interactions. Many aspects of such convoluted system are yet to be understood. An example of such complex processes is soliton fission and dispersive wave generation. While this process is very well understood in single-mode fibers, the efforts to obtain a general theory to accurately describe these effects in multimode systems have been so far unsuccessful. Here, we present the first general theory in this regard. Relying on our theory, we could exactly describe the spectral and temporal features correspond to the pulse propagation in an anomalously dispersive MMF. It also enabled us to not only predict the system output but also to engineer it. We also showed that parabolic multimode fibers can provide a versatile platform for tailoring supercontinuum generation. Experiments and simulations carried out in the anomalous dispersive region indicate that the modal composition (energy distribution and phase relationship among eigenmodes) of the input beam plays an important role in altering the output spectrum.

The propagating beam in a parabolic index multimode fiber experiences a self-imaging behavior. We investigated, for the first time, the effects of acceleration of nonlinear intermodal interactions

in multimode fibers. We demonstrated that this spatiotemporal acceleration can have a significant effect on the temporal and spectral behavior in both dispersion regimes. In the anomalously dispersive region, this acceleration leads to blue-drifting dispersive wave combs while under normal dispersive conditions, we observe a generation of accelerating frequency bands that dynamically and uniformly sweep the entire spectrum. This, in turn, can be utilized to produce a notably flat and uniform supercontinuum, extending over 2.5 octaves.

The same multimode fiber taper platform can be used to generate parabolic pulses. Using this platform, one can avoid any limitation on the bandwidth of these pulses. Also, due to the large core area, the pulse can carry orders of magnitude higher energy level. In addition, due to an input peak power dependent transmission, these fiber tapers can be used at the same time as saturable absorbs for spatiotemporal mode-locking in STML lasers.

An interesting observation that was made in multimode optical fibers was an efficient generation of a second-harmonic and down-converted signal. We showed that germanium-doped parabolic multimode silica fibers can exhibit relatively high SHG conversion efficiencies and down-conversion. Unlike previous experiments, these $\chi^{(2)}$ related processes occurred immediately without any preparation. Of interest would be to consider the potential of the $\chi^{(2)}$ down-conversion process as a source for biphoton generation in quantum optics.

In the last section, we analyzed multicore fiber systems, as another alternative platform for expanding communication bandwidths. We suggested a methodology to find the supermodes and their corresponding eigenvalues in a multicore optical system of any size and dimension. In the end, we suggested a novel scheme for designing multicore systems of equidistant eigenvalues. Such a system can be used to effectively compensate the intermodal group velocity dispersion present in any multimode systems. To do this, a single grating coupler can be utilized to couple all

the modes to each other and hence reduce DGD. It is worth mentioning that due to a large spacing

between the modal eigenvalues and core/cladding indices, there is no radiation loss.

APPENDIX A: THE PYTHON CODE FOR DESIGNING A SIX-ELEMENT PENTAGONAL STRUCTURE WITH EQUIDISTANT EIGENVALUE DISTRIBUTION

```python
import tensorflow as tf
import numpy as np

eig_val = tf.placeholder(dtype=tf.float32, shape=[1, 6])
initial_val = tf.placeholder(dtype=tf.float32, shape=[1, 6])

delta = tf.Variable(initial_value=[[.2, .3, -.1, -.6, .7, 1.]])

initalize_delta = delta.assign(initial_val)

c = 0.42

A = tf.constant([
    [0., 1., 1., 1., 1., 1.],
    [1., 0., c, 0., 0., c],
    [1., c, 0., c, 0., 0.],
    [1., 0., c, 0., c, 0.],
    [1., 0., 0., c, 0., c],
    [1., c, 0., 0., c, 0.]
], dtype=tf.float32)

matrix = A + tf.matmul(delta, tf.eye(6))
matrix = tf.reshape(matrix, shape=[1, 6, 6])
eig, _ = tf.self_adjoint_eig(matrix)

loss = tf.losses.mean_squared_error(labels=eig_val,
                                    predictions=tf.reshape(eig,
shape=[1, 6]))

optimizer =
tf.train.GradientDescentOptimizer(learning_rate=.1).minimize(los
s)

init = tf.global_variables_initializer()
sess = tf.Session()
sess.run(init)
loss_val = 1.
step = 0

min_loss = 1.


#eig_val_array = [[-1, 0, 0, 1, 1, 1]]
temp = np.random.uniform(-4., 4., 3)
eig_val_array =
np.matrix([temp.item(0),temp.item(1),temp.item(2),temp.item(1),t
emp.item(2),temp.item(2)])
```

```python
while loss_val > 0.00001:
    _, new_loss = sess.run([optimizer, loss],
feed_dict={eig_val: eig_val_array})
    if abs(new_loss-loss_val) < 0.00000001:
        if new_loss < min_loss:
            print(step, loss_val)
            print(eig_val_array)
            print(sess.run(eig))
            print(sess.run(delta))
            min_loss = new_loss
        step = 0
        sess.run(initalize_delta, feed_dict={initial_val:
[np.random.uniform(-4., 4., 6)]})
        #eig_val_array = eig_val_array
        temp = np.random.uniform(-4., 4., 5)
        eig_val_array = np.matrix([temp.item(0), temp.item(1),
temp.item(2), temp.item(3), temp.item(4), temp.item(4)])
        loss_val = 1.
    loss_val = new_loss
    step += 1

print(sess.run(delta))
print(sess.run(eig))
```

REFERENCES

1. P. S. J. Russell, "Photonic-Crystal Fibers," J. Light. Technol. **24**, 4729–4749 (2006).

2. J. C. Knight, "Photonic crystal fibres," Nature **424**, 847–851 (2003).

3. J. K. Ranka, R. S. Windeler, and A. J. Stentz, "Visible continuum generation in air–silica microstructure optical fibers with anomalous dispersion at 800 nm," Opt. Lett. **25**, 25 (2000).

4. W. Wadsworth, N. Joly, J. Knight, T. Birks, F. Biancalana, and P. Russell, "Supercontinuum and four-wave mixing with Q-switched pulses in endlessly single-mode photonic crystal fibres," Opt. Express **12**, 299–309 (2004).

5. J. M. Dudley, G. Genty, and S. Coen, "Supercontinuum generation in photonic crystal fiber," Rev. Mod. Phys. **78**, 1135 (2006).

6. J. M. Stone and J. C. Knight, "Visibly "white" light generation in uniform photonic crystal fiber using a microchip laser," Opt. Express **16**, 2670 (2008).

7. "Microstructured Fiber: Photonic crystal fibers advance supercontinuum generation," http://www.laserfocusworld.com/articles/print/volume-52/issue-06/features/microstructured-fiber-photonic-crystal-fibers-advance-supercontinuum-generation.html.

8. D. J. Richardson, J. Nilsson, and W. A. Clarkson, "High power fiber lasers: current status and future perspectives [Invited]," J. Opt. Soc. Am. B **27**, B63 (2010).

9. C. Jauregui, J. Limpert, and A. Tünnermann, "High-power fibre lasers," Nat. Photonics **7**, 861–867 (2013).

10. S. Hädrich, M. Kienel, M. Müller, A. Klenke, J. Rothhardt, R. Klas, T. Gottschall, T. Eidam, A. Drozdy, P. Jójárt, and others, "Energetic sub-2-cycle laser with 216 W average power," Opt. Lett. **41**, 4332–4335 (2016).

11. C. Gaida, M. Gebhardt, F. Stutzki, C. Jauregui, J. Limpert, and A. Tünnermann, "Thulium-doped fiber chirped-pulse amplification system with 2 GW of peak power," Opt. Lett. **41**, 4130–4133 (2016).

12. A. V. Smith, B. T. Do, G. R. Hadley, and R. L. Farrow, "Optical Damage Limits to Pulse Energy From Fibers," IEEE J. Sel. Top. Quantum Electron. **15**, 153–158 (2009).

13. J. M. Stone and J. C. Knight, "From zero dispersion to group index matching: How tapering fibers offers the best of both worlds for visible supercontinuum generation," Opt. Fiber Technol. **18**, 315–321 (2012).

14. T. A. Birks, W. J. Wadsworth, and P. S. J. Russell, "Supercontinuum generation in tapered fibers," Opt. Lett. **25**, 1415 (2000).

15. C. Lesvigne, V. Couderc, A. Tonello, P. Leproux, A. Barthélémy, S. Lacroix, F. Druon, P. Blandin, M. Hanna, and P. Georges, "Visible supercontinuum generation controlled by intermodal four-wave mixing in microstructured fiber," Opt. Lett. **32**, 2173–2175 (2007).

16. T. A. Birks, J. C. Knight, and P. S. J. Russell, "Endlessly single-mode photonic crystal fiber," Opt. Lett. **22**, 961–963 (1997).

17. D. J. Richardson, J. M. Fini, and L. E. Nelson, "Space-division multiplexing in optical fibres," Nat. Photonics **7**, 354–362 (2013).

18. P. Sillard, M. Bigot-Astruc, and D. Molin, "Few-Mode Fibers for Mode-Division-Multiplexed Systems," J. Light. Technol. **32**, 2824–2829 (2014).

19. G. Lopez-Galmiche, Z. S. Eznaveh, J. E. Antonio-Lopez, A. V. Benitez, J. R. Asomoza, J. S. Mondragon, C. Gonnet, P. Sillard, G. Li, A. Schülzgen, and others, "Few-mode erbium-doped fiber amplifier with photonic lantern for pump spatial mode control," Opt. Lett. **41**, 2588–2591 (2016).

20. S. G. Leon-Saval, N. K. Fontaine, J. R. Salazar-Gil, B. Ercan, R. Ryf, and J. Bland-Hawthorn, "Mode-selective photonic lanterns for space-division multiplexing," Opt. Express **22**, 1036 (2014).

21. N. K. Fontaine, R. Ryf, J. Bland-Hawthorn, and S. G. Leon-Saval, "Geometric requirements for photonic lanterns in space division multiplexing," Opt. Express **20**, 27123 (2012).

22. G. P. Agrawal, *Nonlinear Fiber Optics* (Academic press, 2007).

23. A. Picozzi, G. Millot, and S. Wabnitz, "Nonlinear optics: Nonlinear virtues of multimode fibre," Nat. Photonics **9**, 289–291 (2015).

24. W. H. Renninger and F. W. Wise, "Optical solitons in graded-index multimode fibres," Nat. Commun. **4**, 1719 (2013).

25. L. G. Wright, D. N. Christodoulides, and F. W. Wise, "Controllable spatiotemporal nonlinear effects in multimode fibres," Nat. Photonics **9**, 306–310 (2015).

26. L. G. Wright, W. H. Renninger, D. N. Christodoulides, and F. W. Wise, "Spatiotemporal dynamics of multimode optical solitons," Opt. Express **23**, 3492 (2015).

27. G. Lopez-Galmiche, Z. Sanjabi Eznaveh, M. A. Eftekhar, J. Antonio Lopez, L. G. Wright, F. Wise, D. Christodoulides, and R. Amezcua Correa, "Visible supercontinuum generation in a graded index multimode fiber pumped at 1064 nm," Opt. Lett. **41**, 2553 (2016).

28. L. G. Wright, S. Wabnitz, D. N. Christodoulides, and F. W. Wise, "Ultrabroadband Dispersive Radiation by Spatiotemporal Oscillation of Multimode Waves," Phys. Rev. Lett. **115**, 223902 (2015).

29. K. Krupa, A. Tonello, A. Barthélémy, V. Couderc, B. M. Shalaby, A. Bendahmane, G. Millot, and S. Wabnitz, "Observation of Geometric Parametric Instability Induced by the Periodic Spatial Self-Imaging of Multimode Waves," Phys. Rev. Lett. **116**, 183901 (2016).

30. K. Krupa, A. Tonello, B. M. Shalaby, M. Fabert, A. Barthélémy, G. Millot, S. Wabnitz, and V. Couderc, "Spatial beam self-cleaning in multimode fiber," ArXiv160302972 Phys. (2016).

31. V. I. Kruglov, A. C. Peacock, J. M. Dudley, and J. D. Harvey, "Self-similar propagation of high-power parabolic pulses in optical fiber amplifiers," Opt. Lett. **25**, 1753–1755 (2000).

32. V. I. Kruglov, A. C. Peacock, J. D. Harvey, and J. M. Dudley, "Self-similar propagation of parabolic pulses in normal-dispersion fiber amplifiers," JOSA B **19**, 461–469 (2002).

33. V. I. Kruglov, A. C. Peacock, and J. D. Harvey, "Exact Self-Similar Solutions of the Generalized Nonlinear Schr\"odinger Equation with Distributed Coefficients," Phys. Rev. Lett. **90**, 113902 (2003).

34. M. E. Fermann, V. I. Kruglov, B. C. Thomsen, J. M. Dudley, and J. D. Harvey, "Self-similar propagation and amplification of parabolic pulses in optical fibers," Phys. Rev. Lett. **84**, 6010 (2000).

35. B. Crosignani and P. Di Porto, "Soliton propagation in multimode optical fibers," Opt. Lett. **6**, 329–330 (1981).

36. L. G. Wright, S. Wabnitz, D. N. Christodoulides, and F. W. Wise, "Ultrabroadband Dispersive Radiation by Spatiotemporal Oscillation of Multimode Waves," Phys. Rev. Lett. **115**, 223902 (2015).

37. M. A. Eftekhar, L. G. Wright, M. S. Mills, M. Kolesik, R. A. Correa, F. W. Wise, and D. N. Christodoulides, "Versatile supercontinuum generation in parabolic multimode optical fibers," Opt. Express **25**, 9078–9087 (2017).

38. L. G. Wright, W. H. Renninger, D. N. Christodoulides, and F. W. Wise, "Spatiotemporal dynamics of multimode optical solitons," Opt. Express **23**, 3492–3506 (2015).

39.   A. Hasegawa, "Self-confinement of multimode optical pulse in a glass fiber," Opt. Lett. **5**, 416–417 (1980).

40.   B. Crosignani, A. Cutolo, and P. D. Porto, "Coupled-mode theory of nonlinear propagation in multimode and single-mode fibers: envelope solitons and self-confinement," JOSA **72**, 1136–1141 (1982).

41.   L. G. Wright, D. N. Christodoulides, and F. W. Wise, "Controllable spatiotemporal nonlinear effects in multimode fibres," Nat. Photonics **9**, 306–310 (2015).

42.   G. Lopez-Galmiche, Z. S. Eznaveh, M. A. Eftekhar, J. A. Lopez, L. G. Wright, F. Wise, D. Christodoulides, and R. A. Correa, "Visible supercontinuum generation in a graded index multimode fiber pumped at 1064 nm," Opt. Lett. **41**, 2553–2556 (2016).

43.   S. Longhi, "Modulational instability and space time dynamics in nonlinear parabolic-index optical fibers," Opt. Lett. **28**, 2363 (2003).

44.   K. Krupa, A. Tonello, B. M. Shalaby, M. Fabert, A. Barthélémy, G. Millot, S. Wabnitz, and V. Couderc, "Spatial beam self-cleaning in multimode fibres," Nat. Photonics **11**, 237–241 (2017).

45.   J. Andreasen and M. Kolesik, "Nonlinear propagation of light in structured media: Generalized unidirectional pulse propagation equations," Phys. Rev. E **86**, 036706 (2012).

46.   M. Kolesik and J. V. Moloney, "Nonlinear optical pulse propagation simulation: From Maxwell's to unidirectional equations," Phys. Rev. E **70**, 036604 (2004).

47.   D. Hollenbeck and C. D. Cantrell, "Multiple-vibrational-mode model for fiber-optic Raman gain spectrum and response function," JOSA B **19**, 2886–2892 (2002).

48.   A. W. Snyder and J. Love, *Optical Waveguide Theory* (Springer Science & Business Media, 2012).

49.   N. B. Terry, T. G. Alley, and T. H. Russell, "An explanation of SRS beam cleanup in graded-index fibers and the absence of SRS beam cleanup in step-index fibers," Opt. Express **15**, 17509–17519 (2007).

50.   D. J. Richardson, J. M. Fini, and L. E. Nelson, "Space-division multiplexing in optical fibres," Nat. Photonics **7**, 354–362 (2013).

51.   N. Bozinovic, Y. Yue, Y. Ren, M. Tur, P. Kristensen, H. Huang, A. E. Willner, and S. Ramachandran, "Terabit-Scale Orbital Angular Momentum Mode Division Multiplexing in Fibers," Science **340**, 1545–1548 (2013).

52.   R.-J. Essiambre, G. Kramer, P. J. Winzer, G. J. Foschini, and B. Goebel, "Capacity Limits of Optical Fiber Networks," J. Light. Technol. **28**, 662–701 (2010).

53.   A. M. Velazquez-Benitez, J. C. Alvarado, G. Lopez-Galmiche, J. E. Antonio-Lopez, J. Hernández-Cordero, J. Sanchez-Mondragon, P. Sillard, C. M. Okonkwo, and R. Amezcua-Correa, "Six mode selective fiber optic spatial multiplexer," Opt. Lett. **40**, 1663–1666 (2015).

54.   A. Picozzi, G. Millot, and S. Wabnitz, "Nonlinear optics: Nonlinear virtues of multimode fibre," Nat. Photonics **9**, 289–291 (2015).

55.   C. R. Petersen, U. Møller, I. Kubat, B. Zhou, S. Dupont, J. Ramsay, T. Benson, S. Sujecki, N. Abdel-Moneim, Z. Tang, and others, "Mid-infrared supercontinuum covering the 1.4–13.3 µm molecular fingerprint region using ultra-high NA chalcogenide step-index fibre," Nat. Photonics **8**, 830–834 (2014).

56.   J. Carpenter, B. J. Eggleton, and J. Schröder, "Observation of Eisenbud–Wigner–Smith states as principal modes in multimode fibre," Nat. Photonics **9**, 751–757 (2015).

57. W. Xiong, P. Ambichl, Y. Bromberg, B. Redding, S. Rotter, and H. Cao, "Spatiotemporal Control of Light Transmission through a Multimode Fiber with Strong Mode Coupling," Phys. Rev. Lett. **117**, 053901 (2016).

58. W. Xiong, P. Ambichl, Y. Bromberg, B. Redding, S. Rotter, and H. Cao, "Principal modes in multimode fibers: exploring the crossover from weak to strong mode coupling," Opt. Express **25**, 2709–2724 (2017).

59. F. Poletti and P. Horak, "Description of ultrashort pulse propagation in multimode optical fibers," JOSA B **25**, 1645–1654 (2008).

60. A. Mafi, "Pulse propagation in a short nonlinear graded-index multimode optical fiber," J. Light. Technol. **30**, 2803–2811 (2012).

61. P. Aschieri, J. Garnier, C. Michel, V. Doya, and A. Picozzi, "Condensation and thermalization of classsical optical waves in a waveguide," Phys. Rev. A **83**, 033838 (2011).

62. M. Guasoni, "Generalized modulational instability in multimode fibers: Wideband multimode parametric amplification," Phys. Rev. A **92**, 033849 (2015).

63. A. Mecozzi, C. Antonelli, and M. Shtaif, "Nonlinear propagation in multi-mode fibers in the strong coupling regime," Opt. Express **20**, 11673–11678 (2012).

64. H. Pourbeyram, G. P. Agrawal, and A. Mafi, "Stimulated Raman scattering cascade spanning the wavelength range of 523 to 1750 nm using a graded-index multimode optical fiber," Appl. Phys. Lett. **102**, 201107 (2013).

65. W. H. Renninger and F. W. Wise, "Optical solitons in graded-index multimode fibres," Nat. Commun. **4**, 1719 (2013).

66. L. G. Wright, W. H. Renninger, D. N. Christodoulides, and F. W. Wise, "Spatiotemporal dynamics of multimode optical solitons," Opt. Express **23**, 3492–3506 (2015).

67. A. R. Leach, *Molecular Modelling: Principles and Applications* (Pearson education, 2001).

68. K. Krupa, A. Tonello, B. M. Shalaby, M. Fabert, A. Barthélémy, G. Millot, S. Wabnitz, and V. Couderc, "Spatial beam self-cleaning in multimode fibres," Nat. Photonics **11**, 237–241 (2017).

69. Z. Liu, L. G. Wright, D. N. Christodoulides, and F. W. Wise, "Kerr self-cleaning of femtosecond-pulsed beams in graded-index multimode fiber," Opt. Lett. **41**, 3675–3678 (2016).

70. M. A. Eftekhar, Z. Sanjabi-Eznaveh, J. E. Antonio-Lopez, F. W. Wise, D. N. Christodoulides, and R. Amezcua-Correa, "Instant and efficient second-harmonic generation and downconversion in unprepared graded-index multimode fibers," Opt. Lett. **42**, 3478–3481 (2017).

71. K. Krupa, C. Louot, V. Couderc, M. Fabert, R. Guenard, B. M. Shalaby, A. Tonello, D. Pagnoux, P. Leproux, A. Bendahmane, R. Dupiol, G. Millot, and S. Wabnitz, "Spatiotemporal characterization of supercontinuum extending from the visible to the mid-infrared in a multimode graded-index optical fiber," Opt. Lett. **41**, 5785–5788 (2016).

72. W. J. Wadsworth, N. Joly, J. C. Knight, T. A. Birks, F. Biancalana, and P. S. J. Russell, "Supercontinuum and four-wave mixing with Q-switched pulses in endlessly single-mode photonic crystal fibres," Opt. Express **12**, 299–309 (2004).

73. A. Picozzi, "Towards a nonequilibrium thermodynamic description of incoherent nonlinear optics," Opt. Express **15**, 9063 (2007).

74. L. G. Wright, D. N. Christodoulides, and F. W. Wise, "Spatiotemporal mode-locking in multimode fiber lasers," Science **358**, 94–97 (2017).

75.   A. R. Osborne and T. L. Burch, "Internal Solitons in the Andaman Sea," Science **208**, 451–460 (1980).

76.   L. F. Mollenauer, R. H. Stolen, and J. P. Gordon, "Experimental Observation of Picosecond Pulse Narrowing and Solitons in Optical Fibers," Phys. Rev. Lett. **45**, 1095–1098 (1980).

77.   N. J. Zabusky and M. D. Kruskal, "Interaction of "Solitons" in a Collisionless Plasma and the Recurrence of Initial States," Phys. Rev. Lett. **15**, 240–243 (1965).

78.   L. Khaykovich, F. Schreck, G. Ferrari, T. Bourdel, J. Cubizolles, L. D. Carr, Y. Castin, and C. Salomon, "Formation of a Matter-Wave Bright Soliton," Science **296**, 1290–1293 (2002).

79.   A. Hasegawa and F. Tappert, "Transmission of stationary nonlinear optical pulses in dispersive dielectric fibers. I. Anomalous dispersion," Appl. Phys. Lett. **23**, 142–144 (1973).

80.   M. A. Eftekhar, L. G. Wright, M. S. Mills, M. Kolesik, R. A. Correa, F. W. Wise, and D. N. Christodoulides, "Versatile supercontinuum generation in parabolic multimode optical fibers," Opt. Express **25**, 9078–9087 (2017).

81.   J. M. Dudley, G. Genty, and S. Coen, "Supercontinuum generation in photonic crystal fiber," Rev. Mod. Phys. **78**, 1135–1184 (2006).

82.   M. Kolesik and J. V. Moloney, "Nonlinear optical pulse propagation simulation: From Maxwell's to unidirectional equations," Phys. Rev. E **70**, 036604 (2004).

83.   A. V. Gorbach and D. V. Skryabin, "Light trapping in gravity-like potentials and expansion of supercontinuum spectra in photonic-crystal fibres," Nat. Photonics **1**, 653–657 (2007).

84.   J. P. Gordon, "Theory of the soliton self-frequency shift," Opt. Lett. **11**, 662–664 (1986).

85.   S. Pickartz, U. Bandelow, and S. Amiranashvili, "Adiabatic theory of solitons fed by dispersive waves," Phys. Rev. A **94**, 033811 (2016).

86.   S. Pickartz, U. Bandelow, and S. Amiranashvili, "Asymptotically stable compensation of the soliton self-frequency shift," Opt. Lett. **42**, 1416–1419 (2017).

87.   K. Tamura, E. P. Ippen, H. A. Haus, and L. E. Nelson, "77-fs pulse generation from a stretched-pulse mode-locked all-fiber ring laser," Opt. Lett. **18**, 1080–1082 (1993).

88.   F. Ö. Ilday, J. R. Buckley, W. G. Clark, and F. W. Wise, "Self-Similar Evolution of Parabolic Pulses in a Laser," Phys. Rev. Lett. **92**, 213902 (2004).

89.   A. Chong, J. Buckley, W. Renninger, and F. Wise, "All-normal-dispersion femtosecond fiber laser," Opt. Express **14**, 10095–10100 (2006).

90.   W. H. Renninger, A. Chong, and F. W. Wise, "Dissipative solitons in normal-dispersion fiber lasers," Phys. Rev. A **77**, 023814 (2008).

91.   C. Finot, G. Millot, and J. M. Dudley, "Asymptotic characteristics of parabolic similariton pulses in optical fiber amplifiers," Opt. Lett. **29**, 2533–2535 (2004).

92.   C. Finot and G. Millot, "Synthesis of optical pulses by use of similaritons," Opt. Express **12**, 5104–5109 (2004).

93.   U. Österberg and W. Margulis, "Dye laser pumped by Nd: YAG laser pulses frequency doubled in a glass optical fiber," Opt. Lett. **11**, 516–518 (1986).

94.   W. Margulis and U. Österberg, "Second-harmonic generation in optical glass fibers," JOSA B **5**, 312–316 (1988).

95.   R. H. Stolen and H. W. K. Tom, "Self-organized phase-matched harmonic generation in optical fibers," Opt. Lett. **12**, 585–587 (1987).

96.   R. W. Terhune and D. A. Weinberger, "Second-harmonic generation in fibers," JOSA B **4**, 661–674 (1987).

97. M.-V. Bergot, M. C. Farries, M. E. Fermann, L. Li, L. J. Poyntz-Wright, P. S. J. Russell, and A. Smithson, "Generation of permanent optically induced second-order nonlinearities in optical fibers by poling," Opt. Lett. **13**, 592–594 (1988).

98. F. Ouellette, K. O. Hill, and D. C. Johnson, "Light-induced erasure of self-organized χ (2) gratings in optical fibers," Opt. Lett. **13**, 515–517 (1988).

99. V. Mizrahi, Y. Hibino, and G. Stegeman, "Polarization study of photoinduced second-harmonic generation in glass optical fibers," Opt. Commun. **78**, 283–288 (1990).

100. D. Z. Anderson, V. Mizrahi, and J. E. Sipe, "Model for second-harmonic generation in glass optical fibers based on asymmetric photoelectron emission from defect sites," Opt. Lett. **16**, 796–798 (1991).

101. P. G. Kazansky, L. Dong, and P. S. J. Russell, "High second-order nonlinearities in poled silicate fibers," Opt. Lett. **19**, 701–703 (1994).

102. V. Pruneri, G. Bonfrate, P. G. Kazansky, D. J. Richardson, N. G. Broderick, J. P. de Sandro, C. Simonneau, P. Vidakovic, and J. A. Levenson, "Greater than 20%-efficient frequency doubling of 1532-nm nanosecond pulses in quasi-phase-matched germanosilicate optical fibers," Opt. Lett. **24**, 208–210 (1999).

103. A. Okada, K. Ishii, K. Mito, and K. Sasaki, "Phase-matched second-harmonic generation in novel corona poled glass waveguides," Appl. Phys. Lett. **60**, 2853–2855 (1992).

104. P. G. Kazansky, A. Kamal, and P. S. J. Russell, "High second-order nonlinearities induced in lead silicate glass by electron-beam irradiation," Opt. Lett. **18**, 693–695 (1993).

105. M. A. Saifi and M. J. Andrejco, "Second-harmonic generation in single-mode and multimode fibers," Opt. Lett. **13**, 773–775 (1988).

106. D. Ceoldo, K. Krupa, A. Tonello, V. Couderc, D. Modotto, U. Minoni, G. Millot, and S. Wabnitz, "Second harmonic generation in multimode graded-index fibers: spatial beam cleaning and multiple harmonic sideband generation," Opt. Lett. **42**, 971–974 (2017).

107. T. J. Driscoll and N. M. Lawandy, "UV enhancement and erasure of second-harmonic generation in germanosilicate fibers," Opt. Lett. **17**, 571–573 (1992).

108. C. Xia, M. A. Eftekhar, R. A. Correa, J. E. Antonio-Lopez, A. Schülzgen, D. Christodoulides, and G. Li, "Supermodes in Coupled Multi-Core Waveguide Structures," IEEE J. Sel. Top. Quantum Electron. **22**, 196–207 (2016). © 2016 IEEE. Reprinted, with permission, from C. Xia, M. A. Eftekhar, R. A. Correa, J. E. Antonio-Lopez, A. Schülzgen, D. Christodoulides, and G. Li, "Supermodes in Coupled Multi-Core Waveguide Structures,", J. Sel. Top. Quantum Electron. **22**, 196–207 (2016).